

**Impacts of El Niño on the Spring and Summer Extreme
Precipitation over East Asia Based on Observational Data
and CMIP6 Models**

CAO, Dingrui

A Thesis Submitted in Partial Fulfillment
of the Requirements for the Degree of
Doctor of Philosophy
in
Earth and Atmospheric Sciences

The Chinese University of Hong Kong

August 2023

Thesis Assessment Committee

Professor LIU Lin (Chair)

Professor TAM Chi Yung Francis (Thesis Supervisor)

Professor TAI Pui Kuen Amos (Committee Member)

Professor XU Kang (External Examiner)

Abstract

of this entitled:

Impacts of El Niño on the Spring and Summer Extreme Precipitation over East Asia Based on Observational Data and CMIP6 Models

Submitted by CAO Dingrui

for the degree of Doctor of Philosophy

at The Chinese University of Hong Kong in August 2023

With over 22% of the world's population and abundant industrial districts, East Asia (EA) is susceptible to extreme precipitation. Extreme rainfall in EA is strongly affected by El Niño with distinct behaviors during different El Niño types. In this study, impacts of eastern Pacific (EP) and central Pacific (CP) El Niño on boreal spring and summer extreme rainfall over EA are investigated using observations and outputs from the Coupled Model Intercomparison Project phase 6 (CMIP6).

Based on observations, we focus on how EP and CP El Niño affect the following summer extremes over EA. During EP El Niño, more intense extreme precipitation is observed over the south of the Yangtze River (SYR). In contrast, suppressed extremes over the Mei-Yu rainband in China, the Baiu in Japan, and the Changma in South Korea (MBC) are observed. During CP El Niño, weaker (stronger) extreme precipitation is found over SYR (MBC). The extreme precipitation patterns corresponding to different El Niño types depend on the displacement of

the westerly jet (WJ) and the Western Pacific subtropical high that are forced by different sea surface temperature warming signals.

We then investigate the mechanisms resulting in synoptic-scale precipitation extremes over EA based on observations and compare them with the CMIP6 historical runs. On a day-to-day basis, intense daily precipitation is related to enhanced upper-level synoptic-scale waves. Here we use a temperature advection index (TAI) to characterize synoptic-scale activity. Both observed and simulated results show that 72% of Yangtze River Basin (YRB)–South Korea (SK)–south of Japan (SP) extreme events are accompanied by instances of positive TAI. Further study indicates that, in both observations and CMIP6, enhanced upper-level synoptic-scale waves lead to a stronger southward shift of the cold air linked to extreme precipitation over YRB as well as lower-troposphere southwest airflow associated with SK–SP precipitation extremes.

Observed and simulated influences of EP and CP El Niño on springtime extreme rainfall in EA are also studied. When EP El Niño occurs, in observations, 85% of YRB extreme rainfall events are accompanied by instances of positive TAI (as compared to 72% in the climatological sense). However, such a change of association with TAI is not found in CMIP6. Observations further show the intensified atmospheric baroclinicity along the EA WJ during EP El Niño, which favors the development of synoptic-scale activity. In contrast, the interannual-scale westerlies and atmospheric baroclinicity during EP El Niño are poorly simulated in CMIP6 models, resulting in the models' failure to capture the contemporaneous YRB-SK-SP extreme precipitation changes.

Finally, observations show less-than-normal total precipitation extremes in EA during CP El Niño, which is related to the anticyclonic anomaly over Northwestern Pacific extending westward to the East Bay of Bengal. However, the CMIP6 models inadequately represent the circulation characteristics during CP El Niño, leading to their failure in capturing CP El Niño-related rainfall features.

摘要

基於觀測資料和 CMIP6 模式厄爾尼諾對東亞春夏季極端降水的影響

曹丁睿

香港中文大學

東亞擁有全球 22% 的人口和豐富的工業區，易受到極端降水的影響。東亞極端降水深受厄爾尼諾影響，且在不同的厄爾尼諾類型中表現出不同的特徵。利用觀測資料和 CMIP6 模式資料，研究了東部型和中部型厄爾尼諾對東亞地區次年春季和夏季極端降水的影響。

基於觀測，研究了東部型和中部型厄爾尼諾如何影響東亞次年夏季極端降水。在東部型厄爾尼諾期間，長江南部（SYR）的極端降水增強，中國，日本以及韓國的梅雨帶地區（MBC）極端降水減弱。在中部型厄爾尼諾期間，SYR（MBC）的極端降水減弱（增強）。不同厄爾尼諾類型對應的極端降水分佈取決於西風急流和西太平洋副熱帶高壓的位置偏移，不同的海表面溫度增溫信號會強迫出不同的位置偏差。

接著，基於觀測資料研究了引起東亞天氣尺度春季極端降水的機制，並將其與 CMIP6 的歷史模擬資料作對比。結果表明較強的日降水與較強的高空天氣尺度波動有關。利用溫度平流指數（TAI）來表徵天氣尺度活動的強度。觀測和模式結果表明，72% 發生於長江流域（YRB）、韓國（SK）、日本南部（SP）的春季極端降水事件伴隨著正 TAI。進一步研究顯示在觀測和模式中，加強的高空天氣尺度波動有助於冷空氣南下，造成 YRB 的極端降水，也有助於與 SK - SP 極端降水有關的低空西南氣流的形成。

接著基於觀測資料和模式，研究了東部型和中部型厄爾尼諾對東亞次年春季極端降水的影響。在東部型厄爾尼諾年，觀測資料顯示 85% 發生在 YRB–SK–SP 的極端降水伴隨著正 TAI（氣候態下的比例為 72%）。然而，這種與 TAI 有關的極端降水變化無法在 CMIP6 中重現。觀測結果進一步表明，在東部型厄爾尼諾期間，沿著東亞西風急流一帶的大氣斜壓性增強，有利於天氣尺度活動的發展。相比之下，東部型厄爾尼諾期間，CMIP6 模式無法模擬出觀測中的年際尺度的西風急流異常，導致模式無法捕捉到天氣尺度的 YRB–SK–SP 極端降水異常。

最後，觀測結果表明中部型厄爾尼諾下東亞地區的極端降水偏少，這與從西北太平洋延伸到孟加拉灣以東的反氣旋異常有關。然而，由於 CMIP6 模型對中部型厄爾尼諾期間的環流特徵模擬能力不足，無法捕捉到與中部型厄爾尼諾有關的降雨特徵。

Acknowledgment

I would like to take this opportunity to express my heartfelt gratitude to all those who have supported me throughout my Ph.D. journey.

First and foremost, I am deeply grateful to my supervisor, Professor Tam Chi-Yung Francis, for his invaluable guidance and mentorship. Not only did he impart extensive knowledge in the field of atmospheric sciences, but he also nurtured my logical thinking skills. I am truly appreciative of his patience, encouragement, and unwavering support throughout my Ph.D. studies. Without his advice and guidance, I would not have been able to achieve what I have today.

I would also like to extend my gratitude to the members of our research group who provided me with valuable insights and made my academic life vibrant and enjoyable. I cherish the moments spent with all of you in Hong Kong.

I am indebted to Prof. Xu Kang for his careful review of this thesis, which has undoubtedly enhanced its quality. My sincere thanks also go to every staff member at the EASC who has assisted me during the past three years.

Finally, I am profoundly grateful to my parents, for their unwavering support and selfless dedication. Their encouragement and love have been my pillar of strength, enabling me to pursue my Ph.D. research without any burdens.

Table of Contents

Abstract	i
摘要.....	iv
Acknowledgment	vi
Table of Contents.....	vii
List of Figures	xi
List of Tables	xxii
1 Introduction.....	1
1.1 El Niño and its impacts in observations and models.....	1
1.1.1 El Niño diversity and its dynamics	2
1.1.2 Simulated El Niño diversity	5
1.2 The impacts of diverse El Niño on EA rainfall.....	6
1.2.1 El Niño-East Asian rainfall teleconnection.....	6
1.2.2 Impacts of El Niño diversity on EA rainfall	10
1.2.3 Simulated Impacts of El Niño diversity on EA rainfall	12
1.3 El Niño-East Asian extreme rainfall	13
1.3.1 EA extreme rainfall in observations	13
1.3.2 Simulated extreme rainfall in EA	16
1.3.3 Projected extreme rainfall in EA under global warming	17
1.4 Challenges in models' evaluation and prediction	19
1.4.1 Challenges in simulating El Niño diversity and its teleconnections.....	19
1.4.2 Uncertainty of future El Niño diversity and its teleconnections.....	21

1.5 Research questions and thesis outline.....	22
2 Data and Methodology.....	26
2.1 Observational and model datasets	26
2.2 Analysis methods	27
2.2.1 Selection of EP and CP El Niño events in observations.....	27
2.2.2 Selection of EP and CP El Niño events from CMIP6 data	28
2.2.3 The definition of EA extreme precipitation	31
2.2.4 TC extreme precipitation in summer	32
2.2.5 Probability of occurrence for extreme daily rainfall related to EP and CP El Niño.....	33
2.2.6 Moisture budge analysis	33
2.2.7 Temperature advection.....	34
2.2.8 Wave activity flux analysis for stationary Rossby waves.....	34
2.2.9 Eady growth rate	36
3 Impacts of El Niño and its diversity on East Asian summertime precipitation extremes....	41
3.1 Summertime EA precipitation extremes associated with EP and CP El Niño	41
3.2 TC and non-TC extreme precipitation in summer during EP and CP El Niño.....	46
3.2.1 TC precipitation during EP and CP El Niño	46
3.2.2 Non-TC precipitation during EP and CP El Niño.....	50
3.3 Mechanisms of non-TC extreme precipitation changes during EP and CP El Niño ..	52
3.3.1 Circulation associated with non-TC extreme precipitation	52
3.3.2 Circulation anomalies during EP and CP El Niño years.....	56

3.4 Summary	58
4 Evaluating CMIP6 in simulations of spring extreme precipitation over EA	65
4.1 Spring extreme precipitation over EA based on observations and CMIP6 models	65
4.2 The circulations related to extreme precipitation over SEA	67
4.3 Synoptic-scale circulation related to YRB-SK-SP extreme precipitation.....	75
4.4 Model bias for synoptic-scale precipitation over YRB-SK-SP	82
4.5 Summary	83
5 Evaluating the El Niño impacts on spring precipitation extremes over EA in CMIP6	89
5.1 Spring EA precipitation extremes associated with EP and CP El Niño	89
5.2 Large-scale circulation during EP El Niño	93
5.3 Relationship between circulations related to EA extreme precipitation events and EP El Niño	100
5.4 TAI-extreme precipitation over YRB-SK-SP during EP El Niño	104
5.5 TAI-all circulations modulated by EP El Niño.....	105
5.5 Mechanisms for springtime extreme precipitation during CP El Niño.....	114
5.6 Summary	117
6 Conclusion and Discussion	127
6.1 Summer extreme precipitation modulated by two types of El Niño.....	127
6.2 The modulation of EP El Niño on the relationship between spring extreme precipitation and synoptic-scale disturbances	128
6.3 Assessing CMIP6's capability to reproduce extreme spring precipitation over EA and the impacts of EP El Niño.....	130

6.4 Future work	132
Appendix.....	I
A1 Details for extreme rainfall indices	I
A2 Supplemental figures.....	IV
Bibliography	XVIII

List of Figures

Figure 1.1 Schematic diagram of (a) El Niño and (b) La Niña conditions in the Pacific Ocean

(See text in section 1.1.1 for more details). From:

<http://www.pmel.noaa.gov/tao/elnino/nino-home.html>4

Figure 2.1 (a) Spatial correlation coefficients between the observed EOF2 and modeled EOF2

SSTAs patterns (blue bars) and those between the observed EOF2 and the modeled EOF3

(orange bars) from historical simulations of 20 CMIP6 models. (b) Scatter diagram of

spatial correlations between the observed and simulated EP and CP El Niño SSTAs

patterns. The solid red line represents the spatial correlation coefficient threshold of 0.6

for CP El Niño.....30

Figure 3.1 Time-longitude cross-section displays the composite equatorial SSTA (shading;

units: °C), averaged from 5°S to 5°N. The composite encompasses two distinct El Niño

events: (a) EP El Niño and (b) CP El Niño. The label "(0)" signifies the El Niño developing

year, while "(1)" corresponds to the subsequent year. Statistically significant SSTA values

at the 90% confidence level are indicated by white crosses.42

Figure 3.2 Climatology of the 95th percentile of daily precipitation (shading; units: mm day⁻¹)

during the JJA season. Only grids with the precipitation PDF showing the goodness of fit

of gamma distribution for at least 80% of the JJA seasons (using K-S test at 90%

significance level) are shown. See text for details.43

Figure 3.3 Extreme precipitation anomalies during the following JJA season of the (a–e) EP

and (f–g) CP El Niño events. (a, f) total accumulated extreme precipitation (shading; units:

mm season⁻¹), (b, g) extreme precipitation frequency (shading; units: days season⁻¹), (c, h)

extreme precipitation intensity (shading; units: mm day⁻¹), (d, i) seasonal mean extreme precipitation (shading; units: mm season⁻¹), (e, j) scale parameter (β) of extreme precipitation (shading; units: mm day⁻¹). Black dots indicate the signals passing the 90% significance level.45

Figure 3.4 (a) Occurrence frequency of JJA mean TC (shading; units: per season). Composites of anomalous TC occurrence frequency during the JJA season associated with (b) EP and (c) CP El Niño events. TC occurrence frequency is interpolated onto the spatial grid of 5° × 5° horizontal resolution based on the 1951–2007 JTWC best track data. Open black circles indicate the signals passing the 90% significance level.47

Figure 3.5 TC precipitation in JJA. (a) total accumulated TC precipitation (shading; units: mm season⁻¹), (b) TC precipitation frequency (shading; units: days season⁻¹)48

Figure 3.6 Extreme precipitation anomalies associated with TCs during the following JJA of the (a–c) EP and (d–f) CP El Niño events. (a, d) TCs-induced total precipitation (shading; units: mm season⁻¹), (b, e) TCs-induced extreme precipitation frequency (shading; units: days season⁻¹), (c, f) TCs-induced total accumulated extreme precipitation (shading; units: mm season⁻¹). Black dots indicate the signals passing the 90% significance level.49

Figure 3.7 (a) Same as Figure 3.2 except for non-TC extreme precipitation. (b), (c) same as Figure 3.3(a), (b) except for non-TC related extreme precipitation during (b) EP, (c) CP El Niño in JJA(1).50

Figure 3.8 Daily precipitation probability density function (PDF) based on gamma distribution during EP (red curve) and CP El Niño (blue curve) events over (a) SYR and (b) MBC. The 95th percentile values of the daily precipitation associated with EP (CP) El Niño are

indicated by red (blue) vertical lines in (a) and (b), respectively.51

Figure 3.9 Anomalous lower- and upper-level atmospheric circulations associated with the extreme precipitation days in JJA over (a–c) SYR and (d–f) MBC. (a, d) Anomalous vertically integrated moisture flux (vectors; units: $\text{kg m}^{-1} \text{ s}^{-1}$) and its divergence (shading; units: mm day^{-1}); only moisture flux anomalies $> 20 \text{ kg m}^{-1} \text{ s}^{-1}$ are shown. (b, e) Anomalous 500 hPa wind (vectors; units: m s^{-1}) and pressure velocity (shading; units: $10^{-2} \text{ Pa s}^{-1}$); only vectors with magnitudes greater than 1 m s^{-1} are shown. (c, f) Anomalous 200 hPa wind (vectors; units: m s^{-1}) and its zonal component (shading; units: m s^{-1}); only vectors with magnitudes greater than 1 m s^{-1} are shown. The solid red line and red dashed line in (c, f) represent the contours of 25 m s^{-1} zonal wind at 200 hPa and the WJ axis for the extreme precipitation days over (c) SYR and (f) MBC in JJA, the blue lines represent the same for climatology.....54

Figure 3.10 Anomalous local Hadley circulation (vectors; meridional wind and vertical pressure velocity, see scale arrow at upper right) and pressure velocity composites (shading; units: $10^{-2} \text{ Pa s}^{-1}$) averaged over 105°E – 125°E for the extreme precipitation days in JJA over (a) SYR and (b) MBC.....55

Figure 3.11 Same as Figure 3.9, except for the composites during the following JJA season of the (a–c) EP and (d–f) CP El Niño events. Only vectors with magnitudes greater than (a, d) $20 \text{ kg m}^{-1} \text{ s}^{-1}$, (b, e) 0.2 m s^{-1} and (c, f) 0.5 m s^{-1} are shown. White crosses indicate that the signals of (a, d) moisture flux divergence, (b, e) pressure velocity and (c, f) zonal wind anomalies passing 90% significance level.....57

Figure 3.12 SSTA composite (shading; units: $^{\circ}\text{C}$) during the following JJA of the (a) EP and
xiii

(b) CP El Niño events. The red box in (a) and the blue box in (b) denote the tropical IO and MC, respectively. The white crosses indicate that signals pass the 90% significance level.....60

Figure 3.13 Anomalous downward short wave radiation flux (shading; units: W/m^2) and 850 hPa wind (vectors; units: m s^{-1}) during CP El Niño in subsequent spring and summer. Only vectors with magnitudes greater than 0.2 m s^{-1} are shown. The white crosses indicate that signals of downward short wave radiation flux pass the 90% significance level.....61

Figure 3.14 Schematic diagram illustrating the mechanism for causing extreme precipitation changes over SYR and MBC during the following JJA season of the (a) EP and (b) CP El Niño events.63

Figure 4.1 (a, b) Seasonal precipitation mean (shading; units: mm day^{-1}) and (c, d) climatology of the 95th percentile of daily precipitation (shading; units: mm day^{-1}) during the MAM season based on (a, c) APHRODITEv1101 and (b, d) MME mean of 20 models.....66

Figure 4.2 The anomalies of vertically integrated moisture flux (vectors; units: $\text{kg m}^{-1} \text{s}^{-1}$) and its divergence (shading; units: mm day^{-1}) associated with the extreme precipitation days in MAM over SEA based on (a) NCEP reanalysis data and (b) MME mean of 20 models; only moisture flux anomalies $> 20 \text{ kg m}^{-1} \text{s}^{-1}$ are shown.68

Figure 4.3 Same as Figure 4.2, but for 850 hPa meridional temperature gradient (shading; units: $^{\circ}\text{C m}^{-1} \times 10^{-5}$).69

Figure 4.4 Same as Figure 4.2, but for 850 hPa wind (vectors; units: m s^{-1}) and temperature advection (shading; units: $^{\circ}\text{C day}^{-1}$); only vectors with magnitudes greater than 0.5 m s^{-1} are shown.70

Figure 4.5 EOF2 mode of daily temperature advection (shading; units: $^{\circ}\text{C day}^{-1}$) at 850 hPa

based on (a) NCEP reanalysis data and (b) the MME mean of 20 models.....71

Figure 4.6 Regression map of March–May daily precipitation (shading; units: mm day^{-1}) on

TAI based on (a) APHRODITEv1101 and (b) MME mean of 20 models. Black dots in (a)

indicate the signals passing the 95% significance level. Black dots in (b) indicate locations

over which more than 70% of models agree on the sign of precipitation anomalies between

MME and each model.....72

Figure 4.7 The linkage between TAI (Y-axis) and YRB–SK–SP daily rainfall (X-axis) during

extreme precipitation days in observations and CMIP6 models. Red dots represent

extreme precipitation events with positive phase of TAI; Black dots denote extreme

precipitation events with negative phase of TAI.....74

Figure 4.8 Anomalies of March–May 850 hPa daily temperature (shading; units: $^{\circ}\text{C}$) and 850

hPa daily wind (vectors; units: m s^{-1}) obtained by regressing onto (a, d) all-day TAI in

MAM and (b, e) extreme-day TAI in MAM based on (a, b) NCEP data and (d, e) MME

mean of 20 models. Differences between the TAI-extreme and TAI-all temperature

(shading; units: $^{\circ}\text{C}$) and daily wind (vectors; units: m s^{-1}) based on NCEP data and MME

mean of 20 models are given in (c) and (f), respectively; only vectors with magnitudes

greater than 0.1 m s^{-1} are shown. The white crosses in (a, b) indicate that temperature

anomalies pass the 95% significance level, and white crosses in (d, e) indicate locations

over which more than 70% of models agree on the sign of temperature anomalies between

MME and each model.....78

Figure 4.9 Same as Figure 4.8, but for vertically integrated moisture flux (vectors; units: kg m^{-2}

m s^{-1}) and its divergence (shading; units: mm day^{-1}). Only moisture flux anomalies greater than (a, b, d, e) $10 \text{ kg m}^{-1} \text{s}^{-1}$ and (c, f) $5 \text{ kg m}^{-1} \text{s}^{-1}$ are shown. 79

Figure 4.10 Same as Figure 4.8, but for 250 hPa geopotential height anomalies (shading, units: m) 81

Figure 4.11 Biases of MME mean for TAI-all vertically integrated moisture flux (vectors; units: $\text{kg m}^{-1} \text{s}^{-1}$) and its divergence (shading; units: mm day^{-1}). Black dots in (a) indicate locations over which more than 80% of models agree on the sign of anomalies of daily precipitation biases between MME and each model. Only moisture flux anomalies greater than $5 \text{ kg m}^{-1} \text{s}^{-1}$ are shown. 82

Figure 4.12 Schematic diagram illustrating the mechanisms leading to TAI-all precipitation changes over YRB–SK–SP. See text for details. 85

Figure 5.1 Composite SSTA (shading; units: $^{\circ}\text{C}$) during the DJF(0) for (a, c) EP and (b, d) CP El Niño events based on (a–b) observations and (c–d) CMIP6 MME mean of 14 models. The white crosses for observations denote SSTA that are statistically significant at the 95% confidence level, and the white crosses for models indicate more than 70% of models agree on the sign of SSTA between MME and each model. 90

Figure 5.2 Precipitation anomalies during the following MAM season of the (a–d) EP and (e–h) CP El Niño events based on (a, b, e, f) APHRODITEv1101 and (c, d, g, h) MME mean of 14 selected models. (a, e, c, g) total accumulated seasonal precipitation (shading; units: mm season^{-1}), (b, f, d, h) total accumulated extreme precipitation (shading; units: mm season^{-1}). Black dots for (a–f) indicate the signals passing the 90% significance level. Black dots for (c–h) indicate locations over which more than 70% of models agree on the

sign of precipitation anomalies between MME and each model.92

Figure 5.3 Anomalous vertically integrated moisture flux (vectors; units: $\text{kg m}^{-1} \text{s}^{-1}$) and its divergence (shading; units: mm day^{-1}) during the following MAM season of the EP El Niño events based on (a) NCEP and (b) MME mean of 14 selected models. Only moisture flux anomalies $> 5 \text{ kg m}^{-1} \text{s}^{-1}$ are shown.93

Figure 5.4 Same as Figure 5.3 but for 250 hPa wave activity flux (vectors; units: $\text{m}^2 \text{s}^{-2}$) and 250 hPa geopotential height anomalies (shading; units: m). The vectors less than $0.2 \text{ m}^2 \text{s}^{-2}$ are omitted. The white crosses in (a) indicate that geopotential height anomalies passing the 95% significance level. The white crosses in (b) indicate locations over which more than 70% of models agree on the sign of geopotential height anomalies between MME and each model.95

Figure 5.5 Same as Figure 5.3, but for 250 hPa zonal wind (shading; units: m s^{-1}). The white crosses in (a) indicate zonal wind anomalies passing the 95% significance level. The white crosses in (b) indicate locations over which more than 70% of models agree on the sign of zonal wind anomalies between MME and each model.97

Figure 5.6 Climatology of 250 hPa zonal winds (shading; units: m s^{-1}) based on (a) NCEP reanalysis data and (b) MME mean of 14 models. (c) Climatological ensemble-mean 250 hPa zonal wind biases (shading; units: m s^{-1}) from the reanalysis climatology. White crosses in (b) indicate locations over which more than 70% of models agree on the sign of biases of zonal wind between MME and each model.98

Figure 5.7 Same as Figure 5.3, but for vertically integrated atmospheric apparent heat source (shading; units: $\text{K kg m}^{-2} \text{day}^{-1}$). The white crosses in (a) indicate heat source anomalies

passing the 90% significance level. The white crosses in (b) indicate locations over which more than 70% of models agree on the sign of heat source anomalies between MME and each model. 100

Figure 5.8 Daily precipitation probability density function (PDF) during EP El Niño (red curve) and all wet days (blue curve) events over (a) SC, (b) YRB and (c) SK-SP. The 95th percentile values of the daily precipitation associated with EP El Niño (climatology) are indicated by red (blue) vertical dashed (solid) lines in (a-c). 103

Figure 5.9 Anomalies of March–May daily precipitation (shading; units: mm day⁻¹) obtained by regressing onto (a, d) all-day TAI in MAM and (b, e) EP-all-day TAI, and (c, f) the difference between the latter and the former based on (a–c) NCEP data and (d–f) MME mean of 14 models. The black dots in (a–b) indicate precipitation anomalies passing the 95% significance level, and the black dots in (d–e) indicate locations over which more than 70% of models agree on the sign of anomalies of precipitation anomalies between MME and each of model..... 107

Figure 5.10 Same as Figure 5.9 but for 250 hPa geopotential height anomalies (shading; units: m). The white crosses in (a, b) indicate that geopotential height anomalies pass the 95% significance level. White crosses in (d–f) indicate locations over which more than 70% of models agree on the sign of geopotential height anomalies between the MME mean and each model. 109

Figure 5.11 Same as Figure 5.9, but for 850 hPa temperature (shading; units: °C) and 850 hPa wind (vectors; units: m s⁻¹). The white crosses in (a, b) indicate that 850 hPa temperature anomalies pass the 95% significance level, and white crosses in (d–f) indicate locations

over which more than 70% of models agree on the sign of anomalies of 850 hPa temperature anomalies between MME and each of model..... 111

Figure 5.12 Same as Figure 5.9, but for vertically integrated moisture flux (vectors; units: kg m⁻¹ s⁻¹) and its divergence (shading; units: mm day⁻¹). Only moisture flux anomalies greater than (a, b, d, e) 5 kg m⁻¹ s⁻¹ and (c, f) 1 kg m⁻¹ s⁻¹ are shown..... 113

Figure 5.13 Same as Figure 5.3 but for CP El Niño. Only moisture flux anomalies > 5 kg m⁻¹ s⁻¹ are shown. 116

Figure 5.14 SST mean-state bias (shading; units: °C) in the MME of 14 CMIP6 models. White crosses indicate locations over which more than 70% of models agree on the sign of SST bias between MME and each of model. The red box (170°E–80°W; 2°S–2°N) denotes the mean-state SST cold tongue bias. 117

Figure 5.15 Same as Figure 5.3, but for 500 hPa EGR (shading; units: day⁻¹)..... 123

Figure 5.16 Schematic diagram illustrating the mechanisms leading to EP-TAI-all precipitation changes over YRB–SK–SP. See text for details. 124

Figure 6.1 Flow chart illustrating the mechanisms underlying the occurrence of intense synoptic-scale-related precipitation extremes over YRB–SK–SP during EP El Niño... 130

Figure 6.2 Flow chart illustrating the reasons behind the inability of CMIP6 models to accurately reproduce extreme precipitation over YRB–SK–SP during EP El Niño, attributed to synoptic-scale activities..... 131

Figure A1 The first and second leading EOF modes of the tropical Pacific SST anomalies (shading; units: °C) corresponding to (a) EP and (b) CP El Niño in observations for the 1951–2007 period. Proportion of variance explained by each EOF mode is displayed in

brackets at the top of each panel.....	IV
Figure A2 Same as Figure A1, but for the first leading EOF mode of the tropical Pacific SST anomalies (shading; units: °C) for each of the 20 selected CMIP6 coupled models.....	V
Figure A3 Same as Figure A1, but for the second leading EOF mode of the tropical Pacific SST anomalies (shading; units: °C) for each of the 20 selected CMIP6 coupled models.	
.....	VI
Figure A4 Same as Figure A1, but for the third leading EOF mode of the tropical Pacific SST anomalies (shading; units: °C) for each of the 20 selected CMIP6 coupled models....	VII
Figure A5 The anomalies of 850 hPa meridional temperature gradient (shading; units: °C m ⁻¹ × 10 ⁻⁵) associated with the extreme precipitation days in MAM over SEA for each of the 20 selected CMIP6 coupled models.....	VIII
Figure A6 Same as Figure A5 but for 850 hPa wind (vectors; units: m s ⁻¹) and temperature advection (shading; units: °C day ⁻¹); only vectors with magnitudes greater than 0.5 m s ⁻¹ are shown.	IX
Figure A7 EOF2 mode of daily temperature advection (shading; units: °C day ⁻¹) at 850 hPa for each of the 20 selected CMIP6 coupled models.	X
Figure A8 Composite SSTA (shading; units: °C) during the DJF(0) for EP El Niño events based on observations and 14 selected CMIP6 coupled models. The white crosses denote SSTA that are statistically significant at the 95% confidence level.	XI
Figure A9 Same as Figure A8 but for CP El Niño.	XII
Figure A10 Composite SSTA (shading; units: °C) during the MAM(1) for (a, c) EP and (b, d) CP El Niño events based on (a–b) observations and (c–d) CMIP6 MME mean of 14	

models. The white crosses for observations denote SSTA that are statistically significant at the 95% confidence level, and the white crosses for models indicate more than 70% of models agree on the sign of SSTA between MME and each model. XIII

Figure A11 Anomalous vertically integrated moisture flux (vectors; units: $\text{kg m}^{-1} \text{ s}^{-1}$) and its divergence (shading; units: mm day^{-1}) during the following MAM season of the CP El Niño events based on observations and each of the 14 selected CMIP6 coupled models. Only moisture flux anomalies $> 5 \text{ kg m}^{-1} \text{ s}^{-1}$ are shown. XIV

Figure A12 Daily precipitation probability density function (PDF) during EP El Niño (red curve) and all wet days (blue curve) events over the SC region in APHRODITE and 14 CMIP6 models. The 95th percentile values of the daily precipitation associated with EP El Niño (climatology) are indicated by red (blue) vertical dashed (solid) lines. XV

Figure A13 Same as Figure A12 but for the YRB region. XVI

Figure A14 Same as Figure A12 but for the SK–SP region. XVII

List of Tables

Table 1.1 The four RCPs Moss et al. (2010)	25
Table 1.2 ScenarioMIP experiments design for Tier-1 experiment.....	25
Table 2.1 Description of the 20 CMIP6 coupled models analyzed in this study. The 14 models capable of simulating both EP and CP El Niño are marked in boldface font. See text for details.	38
Table 2.2 Selected EP and CP El Niño events.	39
Table 2.3 Description of extreme precipitation indices	40
Table 3.1 Risk Ratio (<i>RR</i>) of JJA extreme precipitation during EP versus CP El Niño over SYR and MBC.	64
Table 4.1 The correlation coefficient between TAI and YRB–SK–SP daily rainfall for climatological sense (TAI-daily rainfall) and for extreme precipitation days (TAI-extreme daily rainfall). The results of observations and models are presented below.	86
Table 4.2 Z test for the extreme-day TAI and all-day TAI in observations and each CMIP6 model.....	87
Table 4.3 The TAI-extreme ratio in observations and each CMIP6 model	88
Table 5.1 Z test for EP-all-day TAI and all-day TAI based on observations and 14 selected CMIP6 models. The models marked by red font indicate the corresponding P value less than 0.05.....	125
Table 5.2 The EP-TAI-extreme ratio and TAI-extreme ratio based on observations, two CMIP6 models with P value less than 0.05 obtained by Z test for TAI during the days of the EP El Niño and climatology, and MME mean of 14 selected models.	126

1 Introduction

1.1 El Niño and its impacts in observations and models

It is well known that the ocean possesses a longer "memory" than atmosphere, which can store the signals of atmospheric circulation anomalies through the sea-air interaction, thus enhancing the predictability of the climate system (Namias et al. 1988). El Niño–Southern Oscillation (ENSO), the most prominent interannual variability in the tropical air-sea coupling system, directly affects the atmospheric and oceanic circulations in the Pacific Ocean, exerting a significant influence on weather and climate systems in local and remote regions through teleconnections (Rasmusson and Arkin 1985; Lau 1997). ENSO is widely recognized as a crucial factor in predicting climate variability due to its close association with global climate. Recent research has focused on El Niño diversity, specifically eastern-Pacific (EP) and central-Pacific (CP) type events, which have demonstrated distinct climate anomalies associated with each type. Investigation of the extreme climate modulated by EP and CP El Niño has also been undertaken. Enhancing our understanding of the impact of El Niño on extreme rainfall anomalies over EA, which exhibits diverse behavior in EP and CP El Niño, is of paramount importance in improving the prediction of precipitation extremes. This will provide a robust theoretical foundation for flood control, disaster relief, and governmental policy formulation. In this study, we employ observational analysis to explore the impacts of both El Niño types on EA extreme precipitation. Furthermore, we examine the biases of CMIP6 models in simulating EA precipitation extremes during El Niño. By analyzing the outputs from the historical run, our goal is to identify the potential factors contributing to these biases and

establish a theoretical basis for enhancing the performance of the models.

1.1.1 El Niño diversity and its dynamics

ENSO dynamics is tied to that of thermocline changes. During natural years, Ekman transport induced by easterly winds causes cold water upwelling, inducing tilted thermocline along the west-east Pacific and lower-than-normal sea surface temperature (SST) in equatorial eastern Pacific (Al et al. 2002). In atmosphere, the Walker Circulation is formed due to the SST in equatorial western Pacific being higher than eastern Pacific, driven by the Bjerknes feedback. A similar mechanism also operates on the perturbed Walker Circulation, causing warm or cold phase of ENSO events (Neelin et al. 1998; Zheng et al. 2014). In warm ENSO phase (El Niño), the depth of thermocline becomes shallow caused by weak easterly winds, thereby inducing weaker upwelling and warm SST in equatorial eastern Pacific, then weakening the Walker Circulation (see **Figure 1.1a** for more details). The reverse situation can be found in cold ENSO phase (La Niña) (see **Figure 1.1b** for more details). Both El Niño and La Niña can affect global climate via modulating atmospheric circulations.

Previous studies suggested that there are two different types of El Niño events: canonical El Niño and El Niño Modoki (Trenberth and Stepaniak 2001; Larkin and Harrison 2005; Ashok et al. 2007; Yu and Kao 2007; Kao and Yu 2009; Kug et al. 2009; Yu and Giese 2013; Williams and Patricola 2018; Chen and Li 2021). During the mature period of conventional El Niño, the positive SST anomalies (SSTAs) are located in the equatorial eastern and central Pacific. Another type of El Niño frequently occurred in recent decades, different from conventional El Niño, positive SSTAs can be found in central Pacific (Kao and Yu 2009). To distinguish

between the two types of El Niño, the conventional El Niño is defined as Eastern-Pacific El Niño (EP El Niño), while another type of El Niño is called Central-Pacific El Niño (CP El Niño). The development of EP El Niño is driven by thermocline feedback through negative Ekman transport anomalies over the equatorial eastern Pacific (Kug et al. 2009). Substantial efforts have been paid to CP El Niño in recent decades due to more frequent related events. The studies in mechanisms related to CP El Niño experienced continuous improvement. Ashok et al. (2007) proposed that equatorial thermocline anomalies cause SSTAs related to CP El Niño due to wind stress changes. Unlike EP El Niño, the upward motion is relocated from the tropical eastern Pacific to the central Pacific. Kug et al. (2009) found that CP El Niño is not caused by the wind-driven thermocline anomalies due to the relatively deep mean thermocline in the central Pacific. They highlighted that zonal advection feedback is the primary reason causing CP El Niño. Yu et al. (2010) also supported that SST warming in the central Pacific during CP El Niño develops from oceanic advection. In general, current studies agreed that CP El Niño is induced by zonal advective feedback, with equatorward Ekman transport over the central pacific and significant convergence in this region (Wang et al. 2019b).

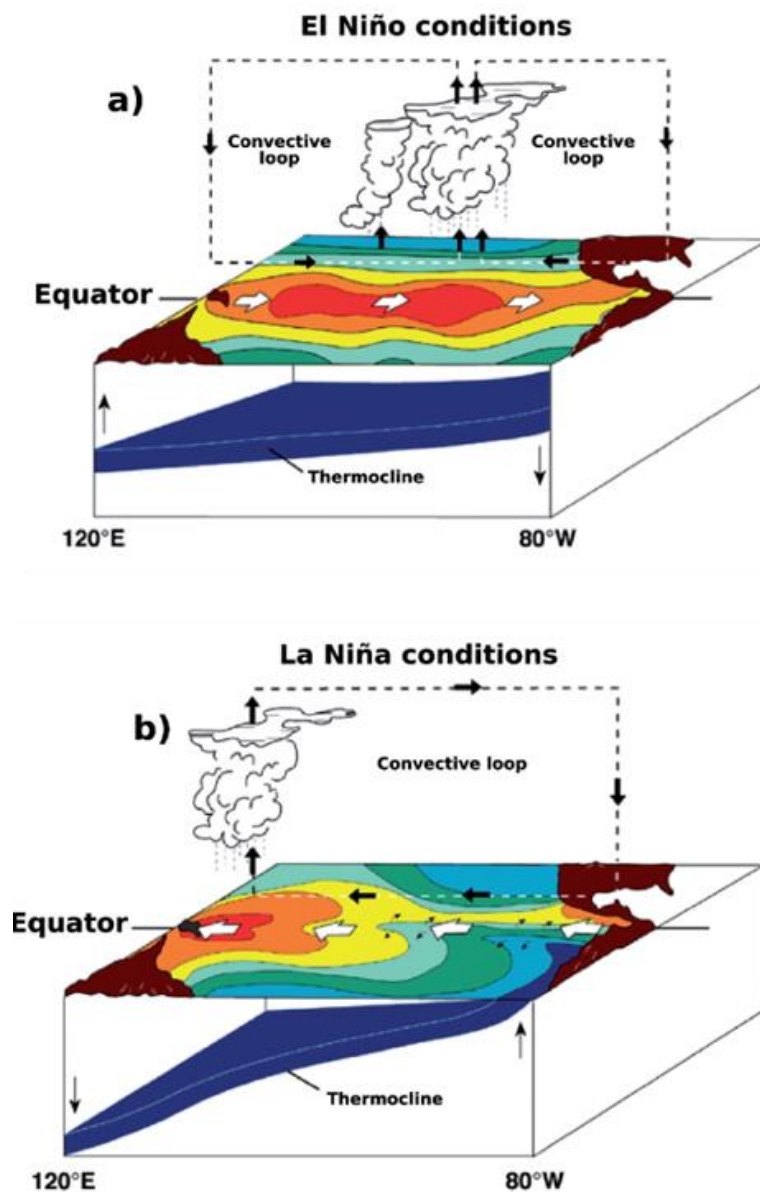


Figure 1.1 Schematic diagram of (a) El Niño and (b) La Niña conditions in the Pacific Ocean (See text in section 1.1.1 for more details). From: <http://www.pmel.noaa.gov/tao/elnino/nino-home.html>

1.1.2 Simulated El Niño diversity

The Coupled Model Intercomparison Project (CMIP) is an international effort to compare and evaluate the performance of global coupled climate models. CMIP5 and CMIP6 are two phases of this project, and both have been used extensively to evaluate present-day climate and also predict future climate changes (Meehl et al. 1997; Eyring et al. 2016). Numerous studies have been dedicated to assessing the performance of El Niño diversity in CMIP5/CMIP6 models (Xu et al. 2017b; Wang et al. 2019a; Feng et al. 2020; Freund et al. 2020; Hou and Tang 2022). In particular, both CMIP5 and CMIP6 models show good skill in simulating EP El Niño in terms of its lifecycle (Bellenger et al. 2014; Xu et al. 2017b; Wang et al. 2019a), temporal and spatial evolutions, but some models have difficulty simulating CP El Niño (Xu et al. 2017b; Wang et al. 2019a). Xu et al. (2017b) investigated how future climate change can modulate two types of El Niño based on 31 CMIP5 models. Compared with observations, all 31 models show good skill in obtaining EP El Niño via empirical orthogonal function (EOF) analysis on SST with interannual variability. Only 17 out of 31 models can reproduce CP El Niño well. Based on Xu et al. (2017b), those 17 state-of-the-art CMIP5 coupled global climate models with reasonable EP (CP) El Niño-related SSTAs are further utilized by Wang et al. (2019a) to investigate the performance of models in reproducing El Niño diversity. All selected models can capture the anomalous Walker Circulation during EP El Niño. In contrast, one-third of the models show the westward displaced anomalous Walker cells for CP El Niño. In other words, most CMIP5 models can well reproduce the EP El Niño related SSTAs and their corresponding circulation anomalies, while some models have large circulation biases during CP El Niño. In recent years, the El Niño-related climate changes extracted from CMIP6 model outputs were

widely discussed, and pointed out a better performance in CMIP6 compared with CMIP5 (Freund et al. 2020; Chen and Jin 2021; Jiang et al. 2021; Liu et al. 2021). Model's bias in simulating El Niño lies in the excessive westward extension of El Niño-related SSTA. Previous studies show that models with severe mean state SST cold tongue bias in tropical Pacific give more westward extension of El Niño SSTA (Li et al. 2019b; Wang et al. 2019a). Although it is improved in CMIP6, this problem still exists (Jiang et al. 2021). Hou and Tang (2022) compared the simulation ability of EP and CP El Niño in CMIP5/CMIP6 models. Both CMIP5 and CMIP6 underestimate the maximum SSTA compared with observations. CMIP6 models show a more realistic SSTA amplitude in both types than CMIP5. In addition, although the spatial structure of CP El Niño is better reflected in CMIP6, the excessive westward extension of CP El Niño variability is still discernible.

1.2 The impacts of diverse El Niño on EA rainfall

1.2.1 El Niño-East Asian rainfall teleconnection

El Niño can affect EA climate through atmospheric teleconnection, and the Western North Pacific anomalous anticyclone (WNPAC) is an essential teleconnection system between EA rainfall and SSTAs in Pacific during El Niño (Zhang et al. 1996, 1999; Zhang and Sumi 2002; Annamalai et al. 2005; Chen et al. 2013; Wu et al. 2017a, b; Yu et al. 2021). In boreal summer when El Niño develops, strong convection can be found in Northwestern Pacific (WNP), characterized by cyclonic wind anomalies in lower troposphere and enhanced precipitation. Then, the cyclonic anomaly over WNP is gradually replaced by anticyclonic anomaly accompanied by suppressed rainfall (Wang and Zhang 2002). This WNPAC typically forms in

boreal fall, and is still present in the mature winter and decaying spring, till the decaying summer when El Niño SSTAs disappear (Wang et al. 2003; Wu et al. 2003). Since the persistent low-level WNPAC is found almost throughout the entire El Niño cycle, it profoundly influences EA rainfall from the developing to the decaying phase of El Niño.

Mechanisms associated with the persistence of WNPAC from developing to decaying seasons during El Niño have been widely discussed by previous studies. Wang et al. (2000) proposed that this persistent WNPAC driven by wind-evaporation-SST (WES) feedback can affect EA climate in successive seasons. Specifically, along the WNPAC southeastern side, the anomalous northwest winds enhance evaporation by triggering the stronger-than-normal northeast trades, then inducing the negative SSTAs in WNP. In turn, the cooling SST in WNP inhibits local convection, which is the primary process to form the persistent WNPAC in situ. The theory of WES feedback is founded on air-sea coupling interaction. Stuecker et al. (2013) argued that the persistent WNPAC is not directly caused by the WES feedback. They conducted a numerical experiment using the atmospheric general circulation model, and their result showed that the given SST forcing in equatorial central-eastern Pacific could also cause the WNPAC. Their findings suggested that the WNPAC can be solely forced by atmospheric processes, while the oceanic feedback is not necessary. To reasonably reveal the mechanism resulting in persistent WNPAC, the wind-moist enthalpy advection-convection feedback is proposed by (Wu et al. 2017a, b) based on moist static energy budget analysis and numerical experiments. To be specific, the positive SSTAs in central-eastern Pacific during El Niño can enhance the local convection, then causing the equatorial-symmetrical two Rossby-wave cyclonic anomalies to the west (Gill 1980). The dry and low moist enthalpy air can be brought

to WNP through the cyclonic anomaly located north of the equator, which induces weaker local convection. The suppressed convection in WNP further sustains the WNPAC. The theory of wind-moist enthalpy advection-convection feedback highlights the internal-atmospheric dynamical and thermal processes rather than air-sea interaction. It is worth noting that although El Niño-related SSTAs cannot be seen during decaying summer, the WNPAC still exists, exerting a significant impact on EA climate (Wang et al. 2000; Xie et al. 2009, 2016; Jiang et al. 2019; Kim and An 2019). Two prevailing views have been proposed to explain how El Niño can continue to impact the WNPAC during the decaying summer: the above mentioned local coupling mechanism in the WNP (Wang et al. 2000) and the Indo-western Pacific Ocean capacitor (IPOC) effect (Xie et al. 2009). The former mechanism suggested that the SSTAs in WNP, caused by El Niño during its development phase, can persist through the subsequent seasons via local atmosphere-ocean coupling, and ultimately strengthen the WNPAC. Another mechanism, the IPOC effect, is considered as a key mechanism that sustains the WNPAC during the decaying summer of El Niño. Specifically, during the mature phase of El Niño, tropical Indian Ocean (IO) experiences warming SST which persists through local air-sea interaction until the following summer. This warming in tropical IO can then excite eastward Kelvin waves in the atmosphere, contributing to the maintenance of the WNPAC during the following summer.

Previous studies have devoted significant attention to the influence of the persistent WNPAC on EA rainfall throughout the El Niño cycle. During the developing autumn, a low-level anticyclonic anomaly over South China Sea (SCS) and an upper-level cyclonic circulation system over central China are found. On the northwestern side of the low-level WNPAC, the

southwest airflows could bring sufficient to the southeast coast of China, resulting in above-normal precipitation over central south China (Wu et al. 2003). This circulation configuration can persist to the mature winter. In the lower troposphere, the southeast airflows move eastward and expand northeastward, leading to intense precipitation throughout Southern China (Zhang et al. 1999; Wu et al. 2003). During the decaying spring, the intense precipitation pattern shifts northeastward and covers the region from the Yangtze River to south of Japan, which is caused by the northward movement of the WNPAC that pushes the southwest airflows northward (Wu et al. 2003). Despite the fact that SSTAs in the central-eastern Pacific disappear during the decaying summer, there is still a significant change in EA rainfall, commonly referred to as a "delayed response" (Yang et al. 2007; Xie et al. 2009; Wu et al. 2010; Zhou et al. 2019). Specifically, the intense precipitation over Yangtze River is attributed to the WNPAC maintained by local atmosphere-ocean coupling and IPOC effect (Wang et al. 2000; Xie et al. 2009, 2016a; Wu et al. 2010). The study conducted by (Zhou et al. 2019) proposed a categorization of the decaying summer of El Niño into two stages: early transition and later transition. The early transition phase is characterized by negative SSTAs in the central-eastern Pacific, while the later transition phase is characterized by neutral or slightly positive SSTAs in the same region. This study also demonstrated that the position of the WNPAC during the decaying summer varied between these two stages. During the later transition stage, the WNPAC is centered at 165°E, 25°N and is forced by both IO warming and anomalous anticyclone-SST feedback due to WNP cooling, resulting in a tripolar rainfall pattern with more intense rainfall over the Yangtze–Huaihe River valley and less intense rainfall over northern and southern China. By contrast, during the early transition stage, the WNPAC is more to the

southwest, mainly maintained by IO warming, leading to more precipitation over eastern China.

1.2.2 Impacts of El Niño diversity on EA rainfall

Previous studies have revealed that the persistence of WNPAC varies among EP and CP El Niño (Feng et al. 2011; Wang et al. 2021b; Yu et al. 2021). During EP El Niño, the WNPAC typically emerges in late autumn and can persist until the following summer due to the local coupling mechanism in the WNP and the IPOC effect. This leads to the persistence of the WNPAC during decaying summer. By contrast, for CP El Niño, the local air-sea interaction between WNP SST cooling and WNPAC is weaker compared to EP El Niño. Consequently, WNPAC decays rapidly and may even disappear by the following spring. However, the WNPAC appears again during CP El Niño in decaying summer. The work from Wang et al. (2021b) indicated that the reappeared WNPAC is related to the enhanced local perturbation circulation-convection feedback due to the strong mean precipitation over the tropical IO.

EP and CP El Niño have distinct effects on EA rainfall throughout their respective cycles. During the developing autumn, the opposite impacts of EP and CP El Niño on EA rainfall can be found (Zhang et al. 2011; Feng et al. 2016). Specifically, during EP El Niño, the EA autumn rainfall shows a dipole pattern, with intense precipitation in southern China and dry conditions in northern China, caused by a weak WNPAC. By contrast, a weak cyclonic anomaly over the WNP during CP El Niño results in less precipitation over the Yangtze River valley and southern China. Different precipitation patterns can also be observed during different types of El Niño in the mature winter. Xu et al. (2019) found that intense precipitation over southern China can

be found in EP-type events, while CP El Niño episodes result in less-than-normal precipitation over the same area. Using Atmospheric General Circulation Model (AGCM) experiments, Xu et al. (2019) suggested that a low-level WNPAC stimulated by SST warming/cooling in the central-to-eastern/western equatorial Pacific during EP El Niño in mature winter contributes to more-than-normal precipitation over southern China. However, the model experiments showed that during CP El Niño in mature winter, SST warming in WNP and SST cooling in SCS offset each other, resulting in a weak and broad-scale low-level anticyclone centered at SCS, which contributes to less winter rainfall over southern China. Although SSTAs for EP and CP El Niño decay during their decaying seasons, the precipitation over EA is also influenced by these two types of El Niño and exhibits diverse precipitation patterns. The works from Feng et al. (2011) and Li et al. (2021b) showed that, during the El Niño in decaying spring, precipitation over southern China during EP El Niño is intensified via southwesterly winds in the northwest flank of the coincidental WNPAC in the lower troposphere. By contrast, the WNPAC during CP El Niño in the following spring is much weaker than EP El Niño, which causes fewer precipitation changes over southern China. Despite EP El Niño-related SSTAs almost disappearing the following summer, the WNPAC also persists due to the IPOC effect (Xie et al. 2009, 2016b), which contributes to heavy rainfall along the Mei-Yu rainband (Xie et al. 2009; Feng et al. 2011; Yuan and Yang 2012). By contrast, during CP El Niño in the following summer, the WNPAC is a little more to the north, resulting in more (less)-than-normal Precipitation over Yellow–Huaihe River Valley (Yangtze River) (Feng et al. 2011; Li et al. 2019c).

1.2.3 Simulated Impacts of El Niño diversity on EA rainfall

The impact of El Niño on EA precipitation has been extensively studied, with several studies examining the ability of models to simulate these impacts (Guo et al. 2017b; Ng et al. 2019; Srinivas et al. 2019; Wang et al. 2019a, 2021a; Fu et al. 2021a). However, models' ability to simulate the impacts of EP and CP El Niño on EA precipitation can differ greatly (Wang et al. 2019a; Li et al. 2021b). Wang et al. (2019a) found that CMIP5 models better captured the EA rainfall anomalies induced by EP El Niño compared to those related to CP El Niño. Specifically, models can well capture the less (more)-than normal precipitation over WNP and SCS (eastern China) caused by WNPAC throughout the EP El Niño cycle. Furthermore, the models successfully replicate the enhancement of the East Asia summer monsoon (EASM) during the following summer of the EP El Niño. By contrast, simulations show a lack of consensus regarding the rainfall patterns over EA and corresponding circulations during CP El Niño. Two-thirds of the models show more realistic precipitation and low-level circulation anomalies, characterized by enhanced rainfall accompanying cyclonic anomaly near 150°E and decreased rainfall with northerly over SCS from early autumn to following spring. However, a large bias is found in the remaining one-third of the models, where overestimated rainfall accompanying cyclonic anomaly over SCS is caused by westward displacement of anomalous Walker cells. Another study by Li et al. (2021b) investigated spring precipitation over southern China during both types of El Niño using ERA5 and the European Centre for Medium-Range Weather Forecasts (ECMWF) operational model; they demonstrated that models in general can better simulate the precipitation pattern over EA during EP El Niño than CP El Niño. In particular, ERA5 shows WNPAC and intense rainfall over SC during EP El Niño, which is

accurately captured by ECMWF operational model. However, ERA5 shows slightly decreased rainfall over SC during CP El Niño, which is not replicated by ECMWF operational model due to overestimated southwesterly winds over WNP.

1.3 El Niño-East Asian extreme rainfall

1.3.1 EA extreme rainfall in observations

Previous studies have indicated that the largest proportion of annual rainfall in EA occurs during summer (Feng et al. 2011; Li and Wang 2018) and spring (Feng et al. 2011; Huang et al. 2015). Therefore, researchers have given considerable attention to EA extreme precipitation in those two seasons and explored their underlying physical mechanisms. The evolution of extreme precipitation during spring and summer in EA is characterized by a monthly shift (Li and Wang 2018; Cui et al. 2019). Specifically, during spring, there is a rainband in China that is concentrated in southern China, while during summer, with the onset of EASM, the rainband shifts northward and becomes centered in the Yangtze River Basin.

Some large-scale factors, such as lower-troposphere WNPAC, upper-level jet and EA trough, have been found to influence the occurrence of spring precipitation extremes in EA (Chen et al. 2003, 2019b; Wang and Zhou 2005; Huang et al. 2015; Shang et al. 2020; Nan et al. 2022; Zhong et al. 2023). For instance, Chen et al. (2019b) discovered a delayed effect of El Niño on spring extreme precipitation over southern China. Specifically, interannual-scale extreme precipitation in southeastern China during spring is attributed to the 850 hPa WNPAC associated with the warming SST in the tropical eastern-central Pacific in the preceding autumn-winter. In addition to the lower-level WNPAC, previous research has demonstrated that

the upper-level jet can also regulate spring extremes in EA (Huang et al. 2015). Specifically, a stronger East Asian subtropical jet (EASJ) plays a dominant role in promoting spring persistent precipitation over southern China, while a weaker East Asian polar front jet (EAPJ) has a modulation role in intensifying precipitation extremes over southern China. The configuration of a strong EASJ and weak EAPJ contributes to enhancing upward motion and increasing convergence of abundant water vapor over southern China. Spring extreme precipitation in southern China is not only modulated by large-scale factors but can also be influenced by synoptic-scale conditions (Chan et al. 2020; Xu et al. 2022b). Chan et al. (2020) examined the rainfall characteristics in southern China from April to June and its associated synoptic conditions. They pointed out that synoptic-scale conditions provided by pre- and post-SCS summer monsoon are quite different, manifested in the displacement of low-level vortices, shearlines, or fronts, and Western Pacific subtropical high (WPSH), inducing different rainfall behaviors. Furthermore, Wang et al (2021c) suggested that during spring, the intensification of daily warm temperature advection over southern China can lead to heavy precipitation in situ through positive diabatic feedback. In addition to warm temperature advection, the encounter of cold air and warm air also results in heavy precipitation through the formation of vigorous frontal systems. Xu et al (2022b) indicated that intensified springtime precipitation over Northern China has a strong correlation with frontal activities. The strong southerly wind not only provides abundant moisture and dynamic forcing for the formation of frontal precipitation but also encounters cold air along the Taihang Mountains and Yan Mountains. This strong frontal system contributes to persistent heavy precipitation in northern China.

The summer extreme precipitation over EA is distinguished by its northward shift to the Mei-14

Yu region, as opposed to spring. This phenomenon is primarily regulated by the EASM, WPSH, monsoon front, and upper-tropospheric westerly jet (WJ) (Zhang et al. 2017; Freychet et al. 2022; Tian et al. 2022). Previous studies demonstrated that the interannual-scale variation of WNPSH plays a crucial role in regulating the extreme rainfall over EA. The westward-displaced WPSH enhances the EASM and increases the moisture transport to EA, thereby contributing to more intense extreme precipitation over the Mei-Yu region (Zhang et al. 2017; Chen et al. 2019a). During the decaying summer of El Niño, the enhanced WPSH leads to more-than-normal seasonal precipitation over the Yangtze River Basin (Xie et al. 2009; Jiang et al. 2019; Chen et al. 2020b), thus more intense extreme precipitation can be found over the area due to these large-scale circulation backgrounds (Yuan et al. 2018; Wang et al. 2022). In addition to large-scale factors, synoptic-scale circulations also affect summertime extreme precipitation over EA (Luo et al. 2016; Tang et al. 2021c). Circulation clustering methods have demonstrated that synoptic-scale extreme precipitation in summer is primarily attributed to EASM-like circulations and cyclone-like circulations (Tang et al. 2021c). Extreme precipitation in the north land area of South China is primarily attributed to EASM-like circulations, while cyclone-like circulations, characterized by landfalling tropical cyclones (TCs) moving northward, induce extreme precipitation in the coastal areas of South China. Previous studies have also indicated that TCs play an important role in the southeastern coastal China rainfall (Chang et al. 2012; Zhang et al. 2018; Wang et al. 2020). Wang et al. (2020) demonstrated that the contribution of TC-induced extreme precipitation over southeastern coastal China is more than 50%, while inland China is less affected by TCs. Their further study showed that during El Niño, TC-induced precipitation over southern China is less intense due

to fewer TCs in suit and suppressed TC genesis in WNP, which is attributed to the prevalent westerly steering flow and abnormal integrated vapor transport from northern to southern China.

1.3.2 Simulated extreme rainfall in EA

Recent studies also attached attention to evaluating the performance of models in simulating EA extreme precipitation and making comparison in terms of those performance between CMIP5 and CMIP6, and results showed that there are improvements in every respect in CMIP6 (Xin et al. 2020; Zhu et al. 2020; Chen et al. 2021; Dong and Dong 2021; Jiang et al. 2021; Freychet et al. 2022). Specifically, Zhu et al. (2020) showed that extreme precipitation over southern China in CMIP6 is apparently improved compared to that in CMIP5. The more moisture transported to southern China in CMIP6 compared with CMIP5 could interpret the reduced dry bias in southern China. Compared with CMIP5, CMIP6 showed less bias of WPSH and EASM, contributing to improved performance in simulating summer precipitation over EA (Xin et al. 2020). Due to SST bias in WNP, weaker WPSH in CMIP5 is the prime reason for underestimating precipitation in Yangtze River; these features are also improved in CMIP6. Although CMIP6 is able to simulate more realistic summer precipitation in the Mei-Yu region compared to CMIP5, most CMIP6 models struggle to capture the spatial distribution and interannual variability of precipitation in the Mei-Yu region (Tong et al. 2022). The study found that models with better simulation of precipitation in the Mei-Yu region can more realistically reflect the relationship between the Mei-Yu rainfall and SST in the equatorial East Pacific and tropical IO (Tong et al. 2022).

1.3.3 Projected extreme rainfall in EA under global warming

Recently, CMIP5 and CMIP6 models have been widely used to investigate future climate changes (Chen et al. 2020a; Wainwright et al. 2021; McGregor et al. 2022; Xu et al. 2022a).

The climate response varies under different global warming scenarios, which are quantified using different emission scenarios (Arnell and Lloyd-Hughes 2014; Zhao et al. 2014; Chen et al. 2020a). For the CMIP5 models, four Representative Concentration Pathways (RCPs) were used to describe various greenhouse gas emission levels, policies, and economic and demographic factors (Moss et al. 2010). Among them, RCP2.6 represented the best-case scenario under emissions reduction, while RCP8.5 represented a high-emissions scenario (see **Table 1.1** for details). With the release of CMIP6, a new scenario framework called Shared Socioeconomic Pathways (SSPs) was introduced to replace RCPs. The SSPs consider not only greenhouse gas emissions, but also changes in energy and land use, and describe a range of socio-economic development pathways and policy measures (Eyring et al. 2016; O'Neill et al. 2017; Riahi et al. 2017). As for CMIP6, five SSPs were used, including SSP1-1.9, SSP1-2.6, SSP2-4.5, SSP3-7.0, and SSP5-8.5 (see **Table 1.2** for details). The changes in extreme precipitation in EA vary under different global warming emission scenarios (Ying et al. 2015; Veiga and Yuan 2021; Zhu et al. 2021). In the following sections, we will review the literature on changes in extreme precipitation under global warming in EA.

Global warming leads to an intensification of the global water cycle, with a greater amount of water vapor circulating in atmosphere and contributing to more extreme weather events such as floods (Monirul Qader Mirza 2002; Kerr 2007; Schiermeier 2011), droughts (Sheffield and

Wood 2008; Trenberth et al. 2014), and hurricanes (Haarsma et al. 2013). Global warming has led to an increase in water vapor supply in the East Asian monsoon region, resulting in more frequent and intense extreme precipitation events in this region (Sun and Ao 2013; Zhu et al. 2021; Chen et al. 2022). The extreme precipitation significantly increased under global warming poses significant challenges to water resource management (Fu et al. 2021b; Tang et al. 2021a; Chen et al. 2022; You et al. 2022). Previous studies have shown that extreme rainfall in the present-day mainly occurs in southern China during spring. Under the RCP8.5 scenario of global warming, the projection indicates a dramatic increase in springtime extreme precipitation in the north part of southern China, suggesting a northward shift of the extreme precipitation pattern (Chen et al. 2022). The Mei-Yu region is the major contributor to extreme summer precipitation in EA (Zhang et al. 2017; Chen et al. 2019a). With the global warming background, extreme precipitation in the Mei-Yu region has significantly increased (Chen et al. 2018, 2021, 2022). In a future warmer climate, the heightened frequency of extreme precipitation in East Asian monsoon region can primarily be attributed to thermodynamic processes, while dynamic processes play a relatively minor role in the changes observed in extreme precipitation (Wang et al. 2012; Endo and Kitoh 2014; Li et al. 2019a; Fu et al. 2021b). With the release of the CMIP6 models, an increasing number of studies were dedicated to comparing the similarities and differences of future climate change projections between CMIP5 and CMIP6 (Chen et al. 2020a; Li et al. 2021a; Zhu et al. 2021). The simulations from both CMIP5 and CMIP6 indicate that higher forcing scenarios are associated with more intense extreme rainfall in EA (Tang et al. 2021b; Zhu et al. 2021). However, compared to CMIP5, CMIP6 simulations show that extreme precipitation in China is more sensitive to global

warming, with more extreme rainfall occurring in most regions south of the Yangtze River and around 40°N latitude (Zhu et al. 2021).

1.4 Challenges in models' evaluation and prediction

1.4.1 Challenges in simulating El Niño diversity and its teleconnections

There still exist systematic biases in simulating the spatiotemporal evolution characteristics of SSTA patterns during El Niño in CMIP5/CMIP6 models, which are closely related to biases in the tropical atmosphere/ocean mean state and biases in the ocean-atmosphere feedback processes (Timmermann et al. 2018; Ferrett and Collins 2019; Jiang et al. 2021). Meanwhile, the simulated bias in mean-state SST has an impact on the teleconnections between El Niño and EA rainfall (Feng et al. 2019; Wang et al. 2019a). State-of-the-art climate models have been found to exhibit a mean-state SST bias, which is characterized by underestimated SST in the equatorial western-central Pacific (EWP), according to previous studies (Dai 2006; Li et al. 2014; Wang et al. 2019a). This westward-extended cold tongue bias significantly affects the models' performance of SST patterns during El Niño (Jiang et al. 2021, 2022). Specifically, the simulated mean-state cold SST bias can enhance the zonal advection feedback due to the enlarged mean zonal SST gradient in EWP, favoring a more westward extension of the El Niño-related SST pattern with a warm SST bias in EWP. Moreover, the underestimation of the El Niño-East Asian winter monsoon (EAWM) teleconnection is indicated by the anomalous cyclonic circulation over WNP caused by the westward extension of El Niño SST pattern due to the severe mean-state cold bias in EWP. Furthermore, the mean-state cold tongue bias in models has a persistent influence on El Niño-related SST and teleconnections from mature

winter to decaying summer (Jiang et al. 2017). During the decaying summer of El Niño, SST warming in EWP dissipates in observations. However, models with mean-state cold tongue bias still exhibit positive SSTAs in EWP during decaying summer, inducing a weaker WNPAC. In contrast, CMIP6 models exhibit a significantly reduced mean-state cold tongue bias in Pacific compared to CMIP5 models. As a result, CMIP6 models can capture a more realistic El Niño-related SST bias as well as the El Niño-monsoon teleconnection (Jiang et al. 2021, 2022). Although the simulating skills of CMIP6 have improved a lot compared with CMIP5, there still exists biases in CMIP6 (Jiang et al. 2021).

Compared to EP El Niño, CP El Niño is more sensitive to the basic state, as indicated by the simulations (McPhaden et al. 2011; Wang et al. 2019a; Jiang et al. 2020). Specifically, CMIP5 models can accurately capture SSTAs and circulation patterns during EP El Niño, regardless of the mean-state cold tongue bias (Bellenger et al. 2014). During CP El Niño, observations reveal a significant upward motion in the central Pacific. However, the severe mean-state cold tongue bias in models enhances the Walker Circulation and Bjerknes feedback, leading to SST cooling and stronger downward motion in the central Pacific during CP El Niño, and causing opposite climate impacts over EA (Wang et al. 2019a). In a recent study by Li et al. (2021), it was found that the incorrect rainfall pattern over EA during CP El Niño in the model is due to a mean-state cold tongue bias in tropical Pacific. However, the EA rainfall pattern during EP El Niño is less affected by this bias. During EP El Niño in simulations, the warmer-than observed SST in the tropical eastern Pacific is caused by a stronger thermocline positive feedback due to the cold tongue bias. This increased convection in the tropical eastern Pacific contributes to a cyclonic anomaly in situ but is too far east to affect EA rainfall, hence the

model is skillful to predict rainfall over EA. On the other hand, during CP El Niño, the observations show slightly decreased rainfall over southern China. However, the cyclonic anomaly cannot be captured by the model due to the weaker anomalous convection caused by mean-state cold tongue bias. This condition leaves more space to develop the WNPAC, which induces overestimated precipitation over southern China in the model. In addition, the mean-state cold tongue bias also affects the projection about future changes in CP El Niño frequency under global warming. previous studies suggested that mean-state cold tongue bias in models causes more frequent CP-type events due to the positive zonal advection feedback in central Pacific (Jiang et al. 2020).

1.4.2 Uncertainty of future El Niño diversity and its teleconnections

Under the modulation of global warming on tropical circulations, circulations related to El Niño have also undergone corresponding changes (Yu and Boer 2002; An et al. 2008; Collins et al. 2010). Previous studies suggested that there is no clear consensus on how the frequency, amplitude, spatiotemporal evolution and diversity of ENSO will change under global warming (Kim and Yu 2012; Power et al. 2013; Cai et al. 2015, 2021; Xu et al. 2017b). On one hand, under global warming, the Walker Circulation weakens, suppressing the Bjerknes feedback and leading to a reduction in the ENSO amplitude. On the another, an intensification of solar shortwave radiation can strengthen the stratification of tropical oceans, and the enhanced temperature advection will lead to an increase in the ENSO amplitude. The combination of these opposite effects might result in uncertainty in the projections of ENSO amplitude and diversity in climate models. For instance, research by Kim and Yu (2012) demonstrated that,

with global warming, the amplitude of CP El Niño is projected to increase, but there is no consensus on changes to the amplitude of EP El Niño. Another study by Xu et al. (2017b) indicated that, with global warming, SST variability during EP El Niño is expected to decrease, and there is no consistent change in SST variability during CP El Niño. Furthermore, there is no agreement on the future changes in relative frequency from CP to EP El Niño under global warming. A recent study compared future changes in intensity and frequency of EP and CP El Niño under SSP5-8.5 scenario in CMIP6 models (Freund et al. 2020). Their result indicated that the intensity and frequency of EP and CP El Niño depend on mean-state changes and Pacific decadal variability (PDV). El Niño state or La Niña state for each model can be confirmed through the west-east SST gradient. Models with projected La Niña state represent for strong warming effect in central-western pacific, which leads to more (less) frequent EP (CP) El Niño. Models with an El Niño-like state, which is significant warming effect in eastern Pacific, cannot directly affect occurrence of EP and CP El Niño. PDV is the dominating factor for the frequency of EP and CP El Niño under El Niño state. During positive (negative) PDV, more (less) EP and CP El Niño can be observed. However, PDV has less effect on the intensity of EP and CP El Niño.

1.5 Research questions and thesis outline

As discussed in this chapter, previous studies have investigated the statistical distribution of spring and summer extreme precipitation over EA and their behaviors during two types of El Niño, as well as how seasonal mean circulations during El Niño years affect seasonal mean and extreme precipitation. However, there has been less research on the atmospheric

circulations related to extreme precipitation. Additionally, the performance of EA extreme precipitation during El Niño in state-of-the-art coupled models has not been extensively studied, leaving a gap in the current research.

To address the research gap mentioned above, three research questions have been proposed, forming the basis of chapters 3-5, respectively.

- 1) We will explore what are the anomalous synoptic-scale circulations associated with extreme precipitation over EA?
- 2) We will examine how El Niño influences the likelihood of the occurrence of atmospheric systems associated with extreme precipitation in EA.
- 3) We will evaluate the ability of CMIP6 models to simulate both the climatological and El Niño-related extreme precipitation over EA, as well as the associated dynamic processes.

To tackle the first research question, we will explore the atmospheric circulation patterns related to extreme precipitation in spring and summer over EA, focusing on the differences between extreme precipitation events and climatology (see **Chapter 4** for spring and **Chapter 3** for summer). To address the second research question, we will calculate the probability of extreme precipitation events occurring in the following spring (see details in **Chapter 4**) and summer (see details in **Chapter 3**) over EA during EP (CP) El Niño. Additionally, we will investigate the large-scale circulation patterns associated with EP (CP) El Niño events to understand their contributions to the occurrence of extreme precipitation over EA. In **Chapter 5**, we will address the third research question by evaluating the ability of CMIP6 models to reproduce the anomalous atmospheric circulation patterns associated with springtime extreme

precipitation over EA, and examining the differences in occurrence probability under EP El Niño events and climatology. Our ultimate goal is to investigate the reasons behind the performance of CMIP6 models in simulating the aforementioned variables.

Table 1.1 The four RCPs Moss et al. (2010)

Name	Radiative forcing	Concentrations (p.p.m.)
RCP8.5	>8.5 Wm ⁻² in 2100	>1370 CO ₂ -equiv. in 2010
RCP6.0	~6 Wm ⁻² at stabilization after 2100	~850 CO ₂ -equiv. (at stabilization after 2100)
RCP4.5	~4.5 Wm ⁻² at stabilization after 2100	~650 CO ₂ -equiv. (at stabilization after 2100)
RCP2.6	Peat at ~3 Wm ⁻² before 2100 and then declines	Peat at ~490 CO ₂ -equiv. before 2100 and then declines

Table 1.2 ScenarioMIP experiments design for Tier-1 experiment

Name	Descriptions
SSP5-8.5	High forcing scenario: Rising radiative forcing leads to 8.5Wm ⁻² by 2100
SSP3-7.0	Medium-high forcing scenario: Rising radiative forcing leads to 7Wm ⁻² by 2100.
SSP2-4.5	Medium forcing scenario: Rising radiative forcing leads to 4.5Wm ⁻² by 2100.
SSP1-2.6	Low forcing scenario: Rising radiative forcing leads to 2.6Wm ⁻² by 2100.
SSP1-1.9	Low forcing scenario: Rising radiative forcing leads to 1.9Wm ⁻² by 2100.

2 Data and Methodology

2.1 Observational and model datasets

As mentioned in **Chapter 1**, this study focuses on how EP and CP El Niño affect boreal spring and summer extreme rainfall in EA after their peaks and using observations and simulations from CMIP6. For El Niño diversity, extreme precipitation over EA, and their related circulation based on observations. Global monthly SST with a horizontal resolution of $1^\circ \times 1^\circ$ from the Hadley Centre Global Sea Ice and Sea Surface Temperature analysis dataset (HadISST version 1.1; Rayner et al. 2003), precipitation at $0.25^\circ \times 0.25^\circ$ resolution from the Asia Precipitation-Highly-Resolved Observational Data Integration Towards Evaluation (APHRODITE version 1101; Yatagai et al. 2012), National Centers for Environmental Prediction/National Center for Atmospheric Research (NCEP/NCAR) reanalysis products (Kalnay et al. 1996), including three-dimensional wind, geopotential height, specific humidity, and temperature, from 1000 to 10hPa with 17 vertical pressure levels resolution at $2.5^\circ \times 2.5^\circ$ are used. To evaluate the contribution of TCs to the summer precipitation over EA, the Joint Typhoon Warning Center (JTWC) best track data are also used to locate TC position. Note that only TCs with maximum wind speed of 34 knots or greater (i.e., tropical storm intensity) are considered. The analysis period of the above datasets covers 1951–2007, with anomalies calculated as deviations from the climatology.

To assess the performance of CMIP6, monthly mean SST as well as daily atmospheric variables from the historical runs of 20 coupled models with the period from 1951–2014 are collected and evaluated. **Table 2.1** gives the corresponding information about the model experiments

(see also <https://pcmdi.llnl.gov/CMIP6/>). Due to the rarity of multiple realizations in models, only the first realization (r1i1p1f1) from each model is utilized. Before conducting the analyses, outputs from each model are interpolated onto the spatial grid same as observations.

2.2 Analysis methods

2.2.1 Selection of EP and CP El Niño events in observations

To focus on the interannual SST variability over the tropics, SSTAs were bandpass filtered to retain variations with periods less than seven years. Since the bandpass filter is capable of removing a significant portion of the trend present in the data, detrend analysis is not performed on SST fields. The Niño 3 index (Niño3I) is defined as the area-averaged SSTA over the equatorial eastern Pacific (5°S – 5°N , 150°W – 90°W). The El Niño Modoki index (EMI; Ashok et al. 2007) is defined as follows:

$$EMI = [SSTA]_C - 0.5 \times ([SSTA]_E + [SSTA]_W) \quad (2.1)$$

where the square brackets with the subscripts in Eq. (2.1) denote the area-mean SSTA averaged over the central tropical Pacific (C: 10°S – 10°N , 165°E – 140°W), the eastern tropical Pacific (E: 15°S – 5°N , 110°W – 70°W) and the western tropical Pacific (W: 10°S – 20°N , 125°E – 145°E), respectively. Niño3I and EMI are used to identify EP and CP El Niño events, respectively, when their December to February (DJF) values are greater than 0.8 standard deviation, then, an EP (CP) El Niño event is identified wherever the normalized Niño3I (EMI) is larger than the EMI (Niño3I) value in the same DJF season. According to these criteria, seven EP and nine CP El Niño events can be found in observations during the 1951–2007 period (**Table 2.2**).

2.2.2 Selection of EP and CP El Niño events from CMIP6 data

Previous studies have indicated that certain CMIP models exhibit inadequate accuracy in capturing SSTAs and teleconnections during CP El Niño (Wang et al. 2019a; Hou and Tang 2022). Hence, defining CP El Niño solely based on EMI is considered insufficiently rigorous. EOF analysis is widely adopted to identify whether a particular model can simulate reasonable modes of variability such as EP and CP El Niño (Xu et al. 2017a, b; Feng et al. 2019; Wang et al. 2019a). For analyzing model outputs, after removing variations larger than seven years, EOF analyses for the DJF averaged SST fields over the domain of 20°S–20°N, 120°E–80°W are carried out in each of the 20 CMIP6 models. The same process is applied to the observations, which acts as a reference when assessing model performance in simulating El Niño diversity (**Figure A1**). The spatial correlation coefficients for SST EOFs modes between observations and each model are then calculated (**Figure 2.1**). The first leading EOF mode (EOF1) of tropical Pacific can well represent EP El Niño (**Figure A2**), with the spatial correlation coefficient between observations and simulations greater than 0.8 for all models (**Figure 2.1b**). Similar to the results of Xu et al. (2017b), the observed CP El Niño SST pattern can be depicted by the second leading EOF (EOF2) in 12 models, while it resembles their third leading EOFs (EOF3) in the other 8 models (see **Figure 2.1a**, **Figure A3** and **Figure A4**). Unlike EP El Niño, the models give a diverse performance in capturing CP El Niño, with spatial correlation coefficients ranging from 0.38 to 0.83. Overall, this is consistent with previous results that EP El Niño is better reproduced than CP El Niño in coupled climate models (Xu et al. 2017b; Wang et al. 2019; Hou and Tang, 2022). A spatial correlation coefficient threshold of 0.6 is adopted so as to identify models that are capable of reproducing CP El Niño. Finally,

14 models that meet the above criteria are selected (boldface font in **Table 2.1**) to investigate the oceanic and atmospheric circulation during two types of El Niño and how they influence the EA extreme rainfall.

The standards for identifying two types of El Niño events in the study of models' evaluation are different from that for observations described in section 2.2.1. Firstly, for each model, principal components of EOF modes corresponding to EP and CP El Niño (EP and CP indices, hereafter) are utilized to identify two types of El Niño events. In particular, the first principal component (PC1) in all runs is defined as the EP index. The second (third) principal component (PC2) (PC3) in 12 (8) models whose CP El Niño SST pattern can be described as EOF2 (EOF3) SST mode is defined as CP index. Then, an EP (CP) El Niño event is found whenever the standardized EP (CP) index is greater than 1.0 (0.7) standard deviation and is also greater than the concomitant CP (EP) index. An additional condition for CP El Niño is that the EP index should be greater than -0.7 standard deviation, aiming to avoid involving EP La Niña events.

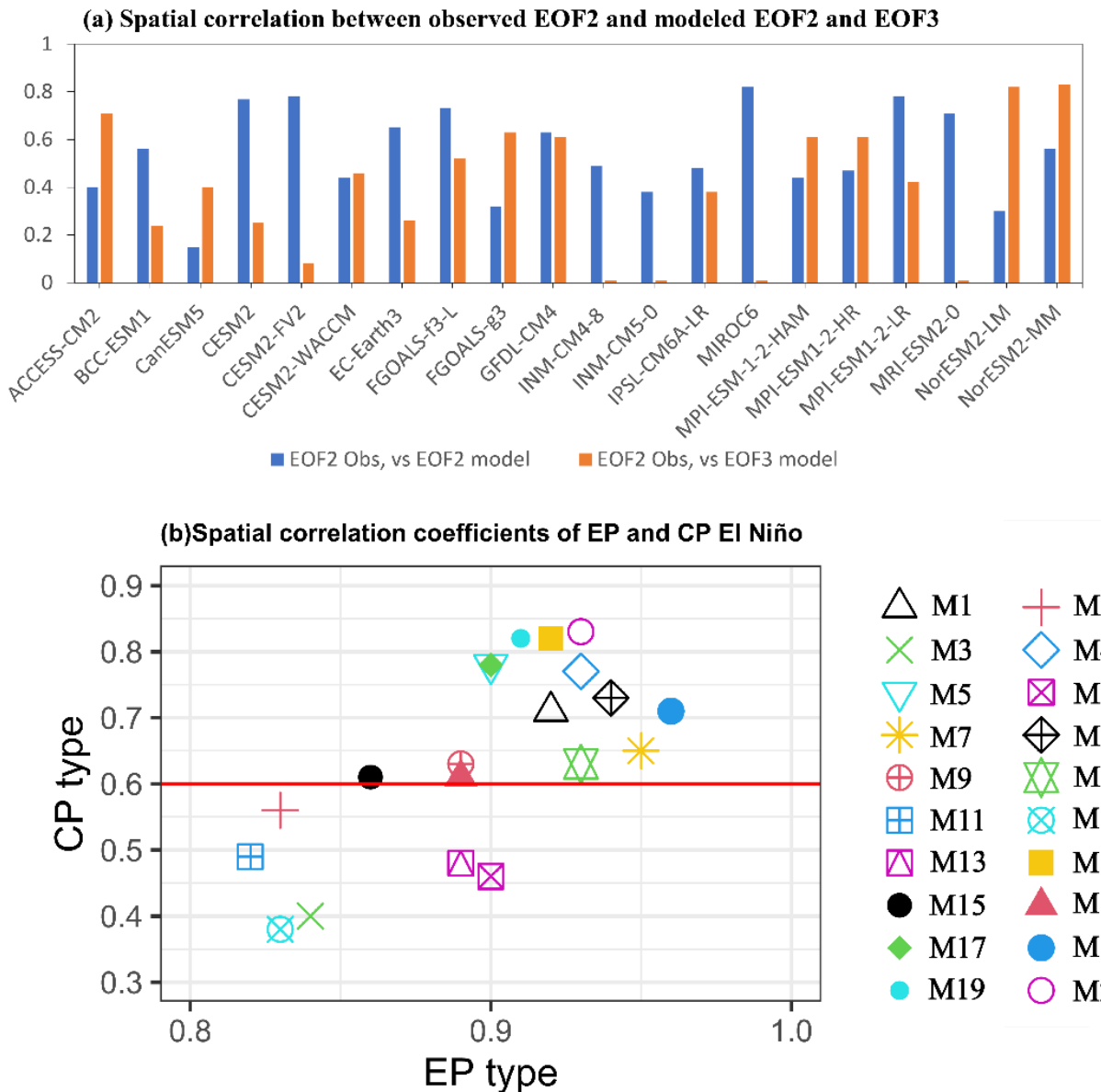


Figure 2.1 (a) Spatial correlation coefficients between the observed EOF2 and modeled EOF2 SSTAs patterns (blue bars) and those between the observed EOF2 and the modeled EOF3 (orange bars) from historical simulations of 20 CMIP6 models. (b) Scatter diagram of spatial correlations between the observed and simulated EP and CP El Niño SSTAs patterns. The solid red line represents the spatial correlation coefficient threshold of 0.6 for CP El Niño.

2.2.3 The definition of EA extreme precipitation

The extreme weather event usually refers to a variable value larger (less) than the prescribed range, a rare occurrence with a probability of less than 10% (Seneviratne et al. 2012). Since there exists a limitation in long-time series climate data and is short of agreement in defining the threshold of the extreme event, the studies related to severe weather become a challenge. To tackle this problem, at the beginning of 21 century, Expert Team on Climate Change Detection and Indices (ETCCDI), formed by World Meteorological Organization (WMO) and World Climate Research Program (WCRP), defined 27 representative climate indices to study the global and regional extreme climate (Alexander et al. 2006; Donat et al. 2013a, b; Kim et al. 2016; Yin and Sun 2018). As for indices of extreme rainfall event, the descriptions are shown in **Table 2.3**, and diverse methods of computation for extreme rainfall threshold is given in **Appendix**.

Precipitation is a typical point process featuring spatial and temporal discontinuities (Malik et al. 2012; Wulf et al. 2012). Therefore, with a focus on EA extreme precipitation, using a prescribed value (i.e., 20mm/day) is inappropriate to define the extreme rainfall event. In our study, percentile approach is adopted to define the extreme precipitation event for each grid. It is widely recognized that daily precipitation data fit well into gamma distributions (Lui et al. 2019; Martinez-Villalobos and Neelin 2019). In this study, we use the parametric gamma distribution to characterize the daily mean precipitation during wet days defined as daily precipitation above 0.1 mm. The two-parameter gamma distribution function is given by:

$$f(x) = \frac{1}{\beta^\alpha \Gamma(\alpha)} x^{\alpha-1} e^{-x/\beta} \quad (\alpha, \beta, x > 0) \quad (2.2)$$

where x is the daily precipitation during wet days, α is the shape parameter characterizing the shape of the gamma distribution, and β is the scale parameter representing the spread of the gamma distribution, which can be interpreted as a measure of the variability of the daily mean precipitation. $\Gamma(\alpha)$ is the gamma function. Following Lui et al. (2019), the Kolmogorov-Smirnov (K-S) test is adopted to test the goodness of fit of the gamma distribution. The K-S test is a statistical method utilized to determine whether a given dataset follows a specified theoretical distribution function. This is accomplished by evaluating the maximum deviation between the empirical cumulative distribution function (CDF) and the theoretical CDF:

$$D_n = \max_x |F_n(x) - F(x)| \quad (2.3)$$

where $F_n(x)$ represents the empirical CDF for a dataset with a sample size of n, and $F(x)$ represents the theoretical CDF. The null hypothesis is rejected at a given significance level if the statistics exceed a critical value in a standard table.

2.2.4 TC extreme precipitation in summer

Landfalling TCs in summer can cause heavy rainfall events over EA (Chang et al. 2012; Zhang et al. 2017; Zhao et al. 2021), it is important to assess contributions of TCs to summer extreme precipitation. According to criteria proposed in previous studies (Jiang and Zipser 2010; Guo et al. 2017a; Lui et al. 2019), precipitation within 5° radius from a TC center is attributed to TCs. Here TC-related precipitation greater than the threshold of extreme precipitation (see section 2.2.3) is defined as TC extreme precipitation. With this approach, extreme precipitation in summer can be regarded as TC and non-TC related extremes, the latter of which can be triggered by a strong monsoon or frontal systems.

2.2.5 Probability of occurrence for extreme daily rainfall related to EP and CP El Niño

The relative influence of EP to CP El Niño events on extreme precipitation can be quantified by the risk ratio (RR ; Sun et al., 2017):

$$RR = \frac{P(E)}{P(E')} \quad (2.4)$$

where $P(E)$ represents the probability of extreme precipitation events during all wet days in the EP El Niño phase, while $P(E')$ indicates the probability of extreme precipitation events during all wet days in the CP El Niño phase. Additionally, the chi-square test is used to evaluate the significance of the precipitation extremes difference during EP and CP El Niño phases.

2.2.6 Moisture budget analysis

Moisture budget analysis is utilized to delineate the underlying physical processes related to precipitation over EA (Wang et al. 2017). The formula for moisture budget is expressed as follows, which shows that the regional precipitation (P) is regarded as a balance between local evaporation from the surface (E) and vertically integrated moisture flux transport (\vec{Q}).

$$P = -\nabla \cdot \vec{Q} + E \quad (2.5)$$

In this study, we focus on the anomalous vertically integrated moisture flux transport (\vec{Q}) during EP and CP El Niño, as well as the anomalies related to extreme rainfall events. The vertically integrated moisture flux vector \vec{Q} is given by (Peixto and Oort, 1992):

$$-\nabla \cdot \vec{Q} = -\frac{1}{g\rho_w} \nabla \cdot \int_{p_s}^{p_t} (q \vec{V}) dp \quad (2.6)$$

where the g is the gravitational acceleration, $\vec{V} = (u, v)$ is the horizontal wind vector, q is the specific humidity, ρ_w is the density of water, p_t is the upper-level pressure (300 hPa),

and the p_s is the surface pressure. $-\nabla \cdot \vec{Q} > 0$ denotes the convergence of moisture flux, and $-\nabla \cdot \vec{Q} < 0$ denotes the divergence of moisture flux.

2.2.7 Temperature advection

It is widely recognized that persistent precipitation in EA is closely associated with atmospheric baroclinicity, which can lead to anomalous cold and warm advection due to the large meridional temperature gradient (Grotjahn et al, 2003). To unveil the linkage between these systems and extreme rainfall events in EA, we calculate the horizontal temperature advection

$(\frac{\partial T}{\partial t})_{adv}$) at 850 hPa:

$$\frac{\partial T}{\partial t}_{adv} = - \left(u \frac{\partial T}{\partial x} + v \frac{\partial T}{\partial y} \right) \quad (2.7)$$

where the $\frac{\partial T}{\partial x}$ and $\frac{\partial T}{\partial y}$ are zonal and meridional temperature gradients at 850 hPa, u and v are zonal and meridional wind at 850 hPa, respectively.

2.2.8 Wave activity flux analysis for stationary Rossby waves

The wave activity flux analysis is widely used to explore the propagation of Rossby waves induced by oceanic and land forcing factors (Kosaka and Nakamura 2006; Liu et al. 2014; Feng et al. 2017; Qian et al. 2019). In this study, wave activity flux analysis is utilized to investigate the stationary Rossby waves induced by EP El Niño. This method is able to quantify wave energy propagation on the basis of mean flows. Plumb wave activity flux (Plumb 1985) and T-N wave activity flux (Takaya and Nakamura 2001) are usually applied to diagnose wave activity evolution characteristics. Plumb (1985) proposed three-dimensional wave activity flux for stationary Rossby wave to represent the propagation direction of the wave energy on the

basis of a conservation relation of small-amplitude stationary eddies on a zonally uniform basic flow. The formulation of Plumb flux (F_s) are as follows (Plumb 1985):

$$F_s = \frac{P}{P_0} \cos\varphi \times \begin{cases} v'^2 - \frac{1}{2\Omega \sin 2\varphi} \frac{\partial(v'\Phi')}{\partial\lambda} \\ -u'v' + \frac{1}{2\Omega \sin 2\varphi} \frac{\partial(u'\Phi')}{\partial\lambda} \\ \frac{f}{S} \left[v'T' - \frac{1}{2\Omega \sin 2\varphi} \frac{\partial(T'\Phi')}{\partial\lambda} \right] \end{cases} \quad (2.8)$$

where the “–” and “’” are the zonal mean and zonal deviation, respectively. φ , λ and Φ represent latitude, longitude and geopotential. $f = 2\Omega \sin \varphi$ donates Coriolis parameter. a and Ω are earth radius and the rotation rate of the earth, respectively. $\frac{P}{P_0}$ is pressure scaled by 1000 hPa and S is the static stability. In the background of westerly mean flows, F_s convergence represents the aggregation of wave activity (wave sink) and F_s divergence indicates the output of wave activity (wave source).

To better diagnose the three-dimensional propagation characteristics of Rossby waves in atmosphere, Takaya and Nakamura (2001) further modified the Plumb flux to make it more suitable for complex background airflow and T–N flux was proposed. Compared with Plumb flux, the meridional component is enhanced in T–N flux, which can better describe the disturbances of Rossby waves with large amplitude embedded in the zonally westerly inhomogeneous flow. The T–N flux highly relies on the mean flows. The formulation of T–N flux (W) is as follows:

$$W = \frac{p \cos\varphi}{2|\bar{U}|} \left(\begin{array}{l} \left(\frac{U}{a^2 \cos^2 \varphi} \left[\left(\frac{\partial \Psi'}{\partial \lambda} \right)^2 - \Psi' \frac{\partial^2 \Psi'}{\partial \lambda^2} \right] + \frac{V}{a^2 \cos \varphi} \left[\frac{\partial \Psi'}{\partial \lambda} \frac{\partial \Psi'}{\partial \varphi} - \Psi' \frac{\partial^2 \Psi'}{\partial \lambda \partial \varphi} \right] \right) \\ \left(\frac{U}{a^2 \cos \varphi} \left[\frac{\partial \Psi'}{\partial \lambda} \frac{\partial \Psi'}{\partial \varphi} - \Psi' \frac{\partial^2 \Psi'}{\partial \lambda \partial \varphi} \right] + \frac{V}{a^2} \left[\left(\frac{\partial \Psi'}{\partial \varphi} \right)^2 - \Psi' \frac{\partial^2 \Psi'}{\partial \varphi^2} \right] \right) \\ \frac{f_0^2}{N^2} \left\{ \frac{U}{a \cos \varphi} \left[\frac{\partial \Psi'}{\partial \lambda} \frac{\partial \Psi'}{\partial z} - \Psi' \frac{\partial^2 \Psi'}{\partial \lambda \partial z} \right] + \frac{V}{a} \left[\frac{\partial \Psi'}{\partial \varphi} \frac{\partial \Psi'}{\partial z} - \Psi' \frac{\partial^2 \Psi'}{\partial \varphi \partial z} \right] \right\} \end{array} \right) + C_U M \quad (2.9)$$

where $\vec{U} = (U, V)$ and $\vec{V} = (u', v')$ are basic wind velocity and perturbed velocity, respectively. Ψ' , $p = \frac{\text{pressure}}{1000} \text{hPa}$ and N^2 denote the perturbation stream-function, pressure scaled by 1000 hPa and buoyancy frequency squared. C_u is used as a vector that represents the phase propagation in the direction of \vec{U} . M donates wave-activity pseudo momentum. Other parameters are identical to the plumb flux (Eq. (2.8)).

Then, assuming the Rossby wave is stationary, C_u in Eq. (2.9) would be zero. T–N wave activity Flux is as follows:

$$W = \frac{p \cos\varphi}{2|\vec{U}|} \begin{pmatrix} \frac{U}{a^2 \cos^2 \varphi} \left[\left(\frac{\partial \Psi'}{\partial \lambda} \right)^2 - \Psi' \frac{\partial^2 \Psi'}{\partial \lambda^2} \right] + \frac{V}{a^2 \cos \varphi} \left[\frac{\partial \Psi'}{\partial \lambda} \frac{\partial \Psi'}{\partial \varphi} - \Psi' \frac{\partial^2 \Psi'}{\partial \lambda \partial \varphi} \right] \\ \frac{U}{a^2 \cos \varphi} \left[\frac{\partial \Psi'}{\partial \lambda} \frac{\partial \Psi'}{\partial \varphi} - \Psi' \frac{\partial^2 \Psi'}{\partial \lambda \partial \varphi} \right] + \frac{V}{a^2} \left[\left(\frac{\partial \Psi'}{\partial \varphi} \right)^2 - \Psi' \frac{\partial^2 \Psi'}{\partial \varphi^2} \right] \\ f_0^2 \left\{ \frac{U}{a \cos \varphi} \left[\frac{\partial \Psi'}{\partial \lambda} \frac{\partial \Psi'}{\partial z} - \Psi' \frac{\partial^2 \Psi'}{\partial \lambda \partial z} \right] + \frac{V}{a} \left[\frac{\partial \Psi'}{\partial \varphi} \frac{\partial \Psi'}{\partial z} - \Psi' \frac{\partial^2 \Psi'}{\partial \varphi \partial z} \right] \right\} \end{pmatrix} \quad (2.10)$$

The first two terms in Eq. (2.10) are taken into account while computing on the horizontal direction. Therefore, the formula of horizontal T–N Wave-Activity Flux could yield as followed:

$$W = \frac{p \cos\varphi}{2|\vec{U}|} \begin{pmatrix} \frac{U}{a^2 \cos^2 \varphi} \left[\left(\frac{\partial \Psi'}{\partial \lambda} \right)^2 - \Psi' \frac{\partial^2 \Psi'}{\partial \lambda^2} \right] + \frac{V}{a^2 \cos \varphi} \left[\frac{\partial \Psi'}{\partial \lambda} \frac{\partial \Psi'}{\partial \varphi} - \Psi' \frac{\partial^2 \Psi'}{\partial \lambda \partial \varphi} \right] \\ \frac{U}{a^2 \cos \varphi} \left[\frac{\partial \Psi'}{\partial \lambda} \frac{\partial \Psi'}{\partial \varphi} - \Psi' \frac{\partial^2 \Psi'}{\partial \lambda \partial \varphi} \right] + \frac{V}{a^2} \left[\left(\frac{\partial \Psi'}{\partial \varphi} \right)^2 - \Psi' \frac{\partial^2 \Psi'}{\partial \varphi^2} \right] \end{pmatrix} \quad (2.11)$$

2.2.9 Eady growth rate

The atmospheric baroclinic instability over EA contributes to the storm track activity (Lee 2000; Chang and Fu 2002; Liao et al. 2018) and is an important cause of abnormal precipitation (Qin et al. 2017). The maximum eady growth rate (EGR) is an effective measure of atmospheric

baroclinic instability (Lindzen and Farrell 1980) and is defined as follows:

$$EGR = 0.31 \frac{|f|}{N} \left| \frac{\partial u(z)}{\partial z} \right| \quad (2.12)$$

where f is the Coriolis parameter, N is the Brunt-Väisälä frequency (where $N^2 = \frac{g}{\theta} \frac{\partial \theta}{\partial z}$, g being the acceleration due to gravity, z is the vertical coordinate, and θ is the potential temperature), $u(z)$ is the vertical profile of the eastward wind component.

Table 2.1 Description of the 20 CMIP6 coupled models analyzed in this study. The 14 models capable of simulating both EP and CP El Niño are marked in boldface font. See text for details.

Model No.	Model acronym	Country	Resolution for atmospheric variables (lon × lat grid points, vertical levels)	Resolution for oceanic variables (lon × lat grid points, vertical levels)
M1	ACCESS-CM2	Australia	192×144, L85	360×300, L50
M2	BCC-ESM1	China	128×64, L26	360×232, L40
M3	CanESM5	Canada	128×64, L49	362×292, L41
M4	CESM2	USA	288×192, L32	320×384, L60
M5	CESM2-FV2	USA	144×96, L32	320×384, L60
M6	CESM2-WACCM	USA	288×192, L70	320×384, L60
M7	EC-Earth3	Europe	512×256, L91	362×292, L75
M8	FGOALS-f3-L	China	360×180, L32	360×218, L30
M9	FGOALS-g3	China	180×90, L26	360×218, L31
M10	GFDL-CM4	USA	360×180, L33	1440×1080, L75
M11	INM-CM4-8	Russia	180×120, L21	360×318, L40
M12	INM-CM5-0	Russia	180×120, L73	720×720, L40
M13	IPSL-CM6A-LR	France	144×143, L79	362×332, L75
M14	MIROC6	Japan	256×128, L81	360×256, L63

M15	MPI-ESM-1-2-HAM	Germany	192×96, L47	256×220, L40
M16	MPI-ESM1-2-HR	Germany	384×192, L95	802×404, L40
M17	MPI-ESM1-2-LR	Germany	192×96; L47	256×220, L40
M18	MRI-ESM2-0	Japan	320×160, L80	360×364, L61
M19	NorESM2-LM	Norway	144×96, L32	360×384, L70
M20	NorESM2-MM	Norway	288×192, L32	360×384, L71

Table 2.2 Selected EP and CP El Niño events.

EP	1965/66	1972/73	1976/77	1982/83	1986/87	1991/92	1997/98		
CP	1957/58	1963/64	1968/69	1977/78	1987/88	1990/91	1994/95	2002/03	2004/05

Table 2.3 Description of extreme precipitation indices

Abbreviation	Description	Unit
Rx1day	Maximum 1-day precipitation:	mm
Rx5day	Maximum consecutive 5-day precipitation	mm
R10mm	Annual count of days when daily precipitation amount ≥ 10 mm	d
R20mm	Annual count of days when daily precipitation amount ≥ 20 mm	d
CWD	Annual maximum number of consecutive days with daily precipitation amount ≥ 1 mm	d
PRCPTOT	Annual total precipitation in wet days	mm
R95pTOT	Annual total precipitation when daily precipitation amount on a wet day > 95 percentile	mm
R99pTOT	Annual total precipitation when daily precipitation amount on a wet day > 99 percentile	mm
SDII	Simple precipitation intensity index	mm

3 Impacts of El Niño and its diversity on East Asian summertime precipitation extremes

In this chapter, based on observations, the circulation related to summer extreme precipitation over EA and how two types of El Niño affect the decaying summer extreme precipitation over EA are investigated. We will document the modulation of summer precipitation extremes by EP and CP El Niño. More importantly, a better understanding of such modulation by the two types of El Niño provides a theoretical basis for improving models' performance in predicting EA extreme rainfall.

3.1 Summertime EA precipitation extremes associated with EP and CP El Niño

We first consider the temporal evolutions of the equatorial Pacific and Indian SSTA averaged between 5°S and 5°N associated with the EP and CP El Niño events (**Figure 3.1**). For EP El Niño, positive SSTA can be found over the central to eastern Pacific, with peak values in boreal wintertime. During boreal summer of the decaying year, positive SSTA is replaced by cold anomalies in the eastern Pacific (**Figure 3.1a**). The most apparent difference between EP and CP El Niño is that, for the former, the maximum SSTA is located to the east, whereas for the latter, warming occurs west of 150°W in the tropical Pacific. During CP El Niño, weak positive SSTA first appears in the western Pacific during boreal spring, which propagates to the central Pacific and peaks in winter. Finally, positive SSTA disappears during boreal spring in the decaying year (**Figure 3.1b**). For both EP and CP El Niño, the mature phase is in boreal winter, indicating same seasonal phase-locking behavior. It is noteworthy that IO region SST is

warmer-than-normal from its peak to decaying summer during EP El Niño. Many studies show that such persistent signals can exert climatic influences after EP El Niño has dissipated (the so-called “capacitor effect”; see Xie et al. 2009, 2016). On the other hand, the IO warming counterpart during CP El Niño is less persistent, with significant warming found during the decaying spring only (**Figure 3.1b**).

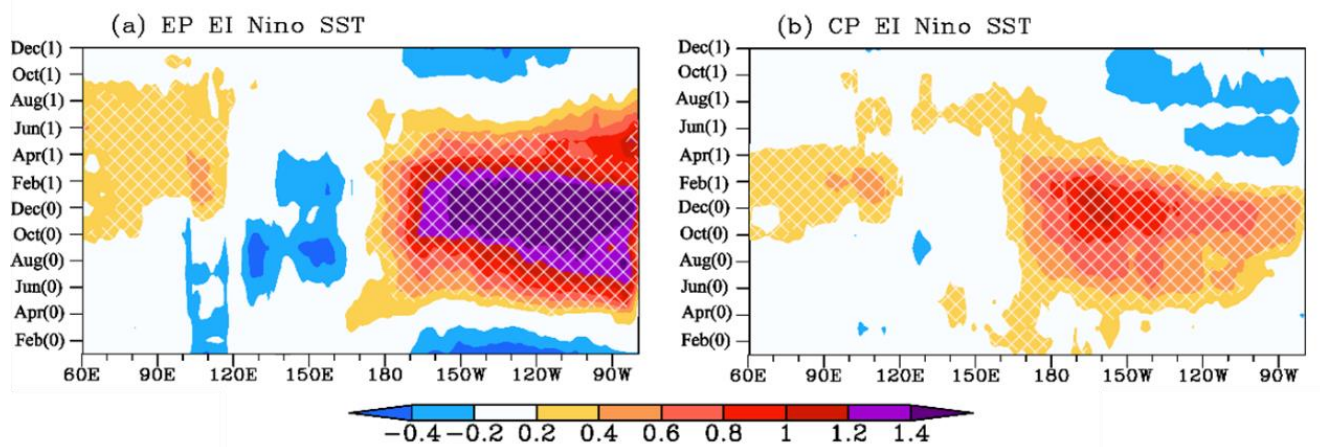


Figure 3.1 Time-longitude cross-section displays the composite equatorial SSTA (shading; units: $^{\circ}\text{C}$), averaged from 5°S to 5°N . The composite encompasses two distinct El Niño events: (a) EP El Niño and (b) CP El Niño. The label "(0)" signifies the El Niño developing year, while "(1)" corresponds to the subsequent year. Statistically significant SSTA values at the 90% confidence level are indicated by white crosses.

The climatological distribution of summertime extreme precipitation over EA is also examined. Following Kim et al. (2019), we first calculate the 95th percentile of daily precipitation based on the fitted gamma distribution for the June–July–August (JJA) season for each year from 1951 to 2007. **Figure 3.2** gives the climatology of these 95th percentile values (referred to as the “95th percentile threshold”), showing only those grids with daily precipitation probability

density function (PDF) fitted well to the gamma distribution for at least 80% of time (using the K-S test at significance level = 0.1). Values greater than 30 mm can be found over the Yangtze River, South Korea, and south of Japan. Note that intense precipitation is also seen in coastal southern China in JJA, which might be related to TC activity in summer (Chang et al. 2012; Guo et al. 2017a; Lui et al. 2019; Liu and Wang 2020). Due to their different mechanisms, TC and non-TC summertime precipitation are considered separately in this study.

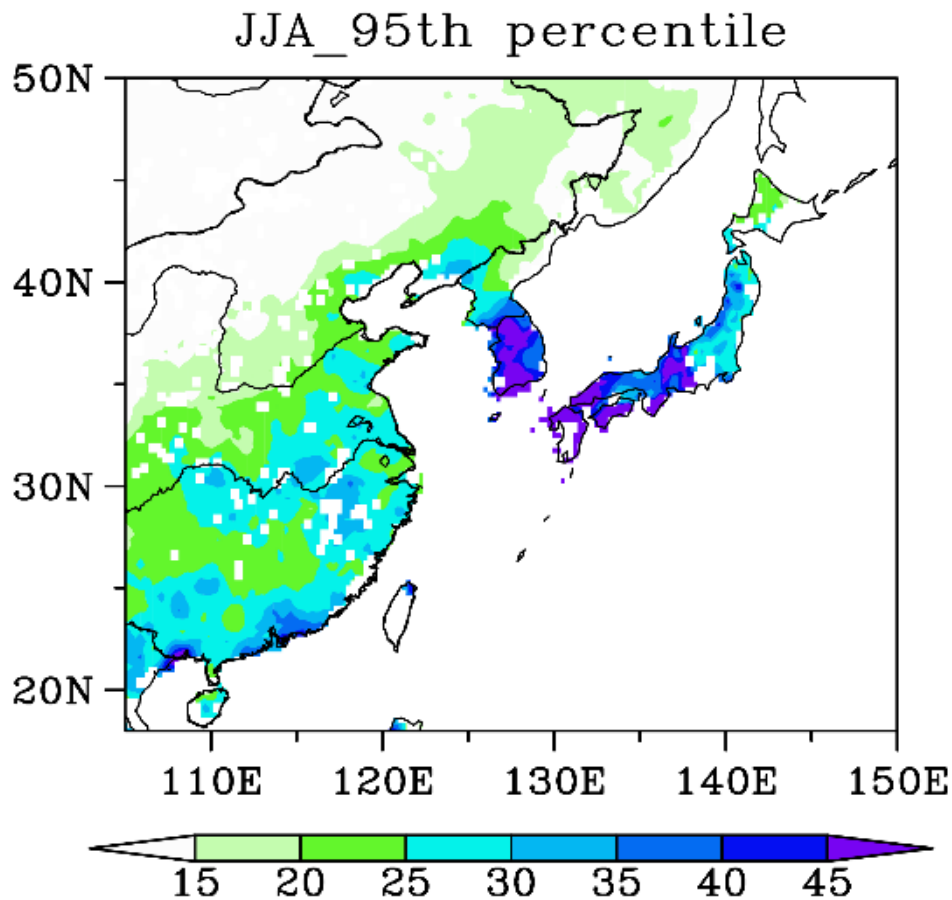


Figure 3.2 Climatology of the 95th percentile of daily precipitation (shading; units: mm day^{-1}) during the JJA season. Only grids with the precipitation PDF showing the goodness of fit of gamma distribution for at least 80% of the JJA seasons (using K-S test at 90% significance level) are shown. See text for details.

How EP and CP El Niño affect extreme precipitation frequency and intensity are now investigated. Total extreme precipitation is defined as the accumulated rainfall equal to or larger than the 95th percentile threshold for a season. Frequency is defined as the number of days within a season when daily rainfall is equal to or larger than the 95th percentile threshold, and the intensity is the 95th percentile value for a particular season. **Figure 3.3a–c** and **3.3f–h** show the composite anomalous total extreme precipitation, frequency, and intensity for EP and CP El Niño events. In general, spatial patterns of anomalous total extreme precipitation (**Figure 3.3a and 3.3f**), frequency (**Figure 3.3b and 3.3g**), and intensity (**Figure 3.3c and 3.3h**) during El Niño event are similar to each other, regardless of the type of El Niño. More intense precipitation over SYR (110°E – 122°E ; 25°N – 30°N , see red box in **Figure 3.3a and 3.3f**), and less intense precipitation over the Shandong peninsula, south of Japan and South Korea are seen during EP El Niño years (**Figure 3.3a–c**). Hereinafter the Mei-Yu rain belt in China, Baiu in Japan, Changma in South Korea are referred to as MBC (i.e., within 110°E – 135°E ; 32°N – 36°N ; see the blue box in **Figure 3.3a and 3.3f**). In contrast, there is reduced (enhanced) extreme precipitation over SYR (MBC) during CP El Niño (**Figure 3.3f–h**). Similar spatial patterns for each El Niño type can be found in the anomalous seasonal mean precipitation (**Figure 3.3d and 3.3i**), and the scale parameter (**Figure 3.3e and 3.3j**); the matching between the seasonal mean and extremes indicates that the latter is an essential contributor to the total precipitation over EA.

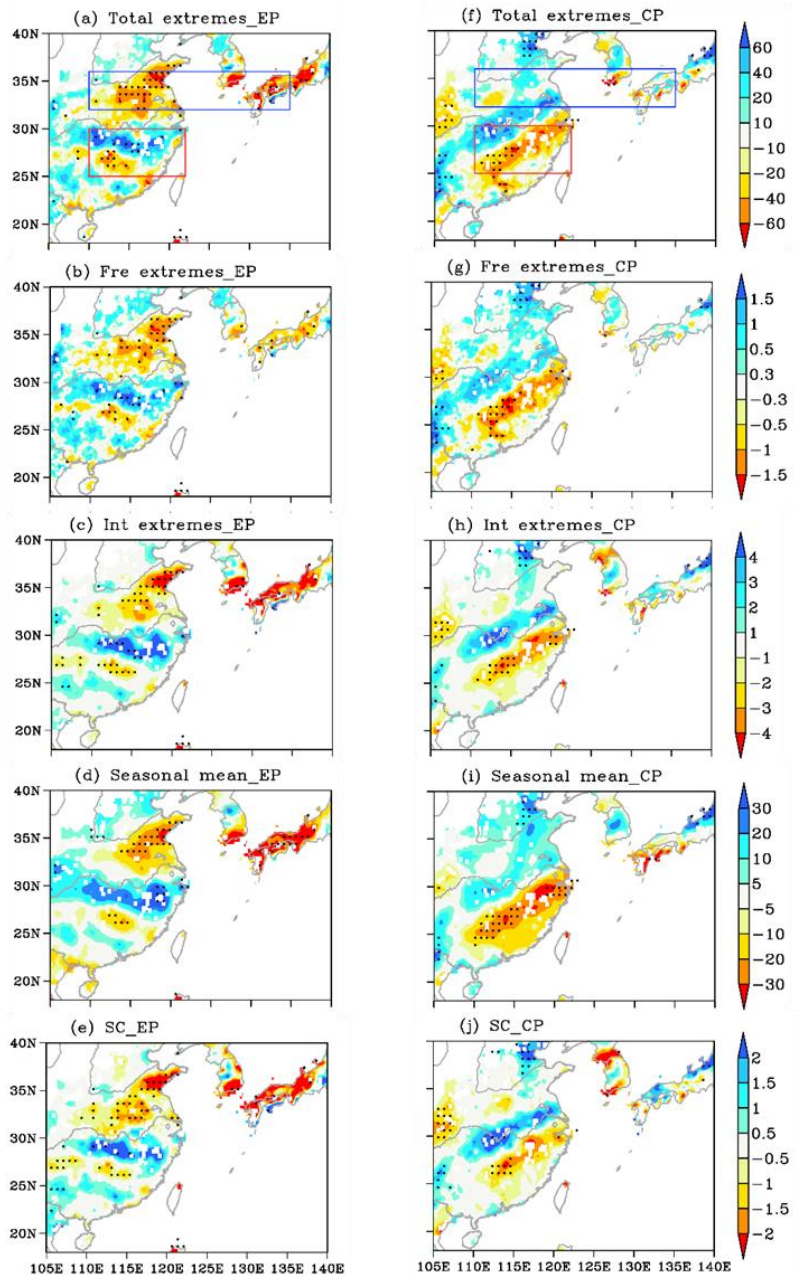


Figure 3.3 Extreme precipitation anomalies during the following JJA season of the (a–e) EP and (f–g) CP El Niño events. (a, f) total accumulated extreme precipitation (shading; units: mm season⁻¹), (b, g) extreme precipitation frequency (shading; units: days season⁻¹), (c, h) extreme precipitation intensity (shading; units: mm day⁻¹), (d, i) seasonal mean extreme precipitation (shading; units: mm season⁻¹), (e, j) scale parameter (β) of extreme precipitation (shading; units: mm day⁻¹). Black dots indicate the signals passing the 90% significance level.

3.2 TC and non-TC extreme precipitation in summer during EP and CP El Niño

3.2.1 TC precipitation during EP and CP El Niño

Here we inspect the contributions of TCs to EA precipitation and its El Niño-related variations.

TC frequency (TCF) is defined as the total count of TC occurrences within each $5^\circ \times 5^\circ$ grid box every 6 hours based on JTWC 6 hourly best track data. Only systems reaching the tropical storm (TS) intensity (local maximum wind speed > 34 knots) are calculated. TC precipitation is defined as precipitation within 5° radius from the TC center. **Figure 3.4** presents the climatology of TCF and anomalous TCF composites during two types of El Niño in the WNP basin. The most frequent TC occurrence is found east of the Luzon Strait. About two to six TCs appear per season over coastal southern China and south of Japan (**Figure 3.4a**). Reduced TCF is found in the whole WNP basin during EP El Niño (**Figure 3.4b**), while slightly less-than-normal TCs are observed over SC and south of Japan during CP El Niño (**Figure 3.4c**).

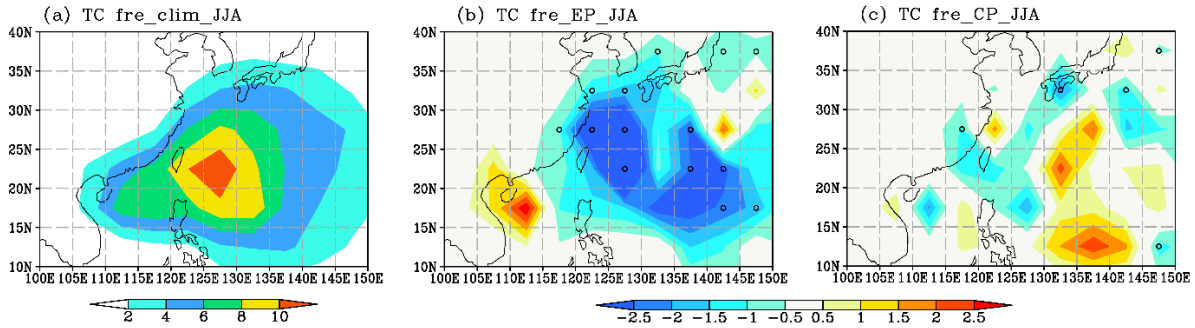


Figure 3.4 (a) Occurrence frequency of JJA mean TC (shading; units: per season). Composites of anomalous TC occurrence frequency during the JJA season associated with (b) EP and (c) CP El Niño events. TC occurrence frequency is interpolated onto the spatial grid of $5^\circ \times 5^\circ$ horizontal resolution based on the 1951–2007 JTWC best track data. Open black circles indicate the signals passing the 90% significance level.

The summertime total TC precipitation (**Figure 3.5a**) and its frequency (**Figure 3.5b**) indicate the strongest extreme TC precipitation over coastal southern China, south of Japan, and South Korea, consistent with previous studies (Lee et al. 2010; Liu and Wang 2020). TC precipitation during EP and CP El Niño are compared in **Figure 3.6**. Fewer TCs in the WNP basin lead to less TC-related precipitation over eastern coastal China, south of Japan, and Korea during both EP and CP El Niño (**Figure 3.6a and 3.6d**). Similar results can be found in total TC extreme precipitation (**Figure 3.6c and 3.6f**). In terms of the frequency of TC extreme precipitation, it is reduced over SYR and Taiwan during EP El Niño (**Figure 3.6b**), but otherwise there is no obvious change during CP El Niño (**Figure 3.6e**). Overall, EP El Niño affects both the frequency and total extreme TC precipitation over eastern coastal China, while CP El Niño only influences the total extreme TC precipitation.

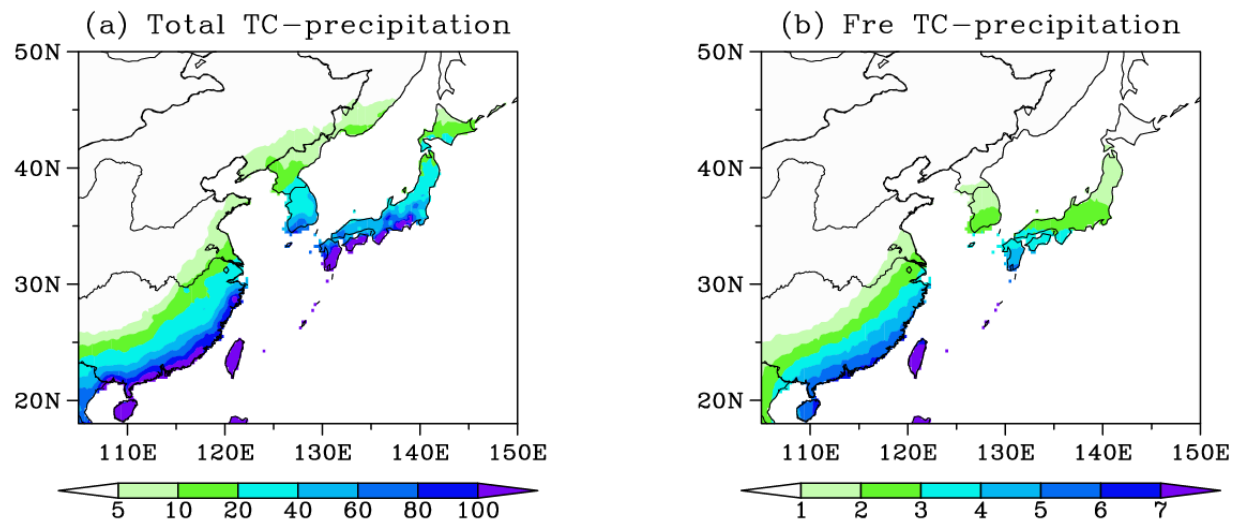


Figure 3.5 TC precipitation in JJA. (a) total accumulated TC precipitation (shading; units: mm season⁻¹), (b) TC precipitation frequency (shading; units: days season⁻¹)

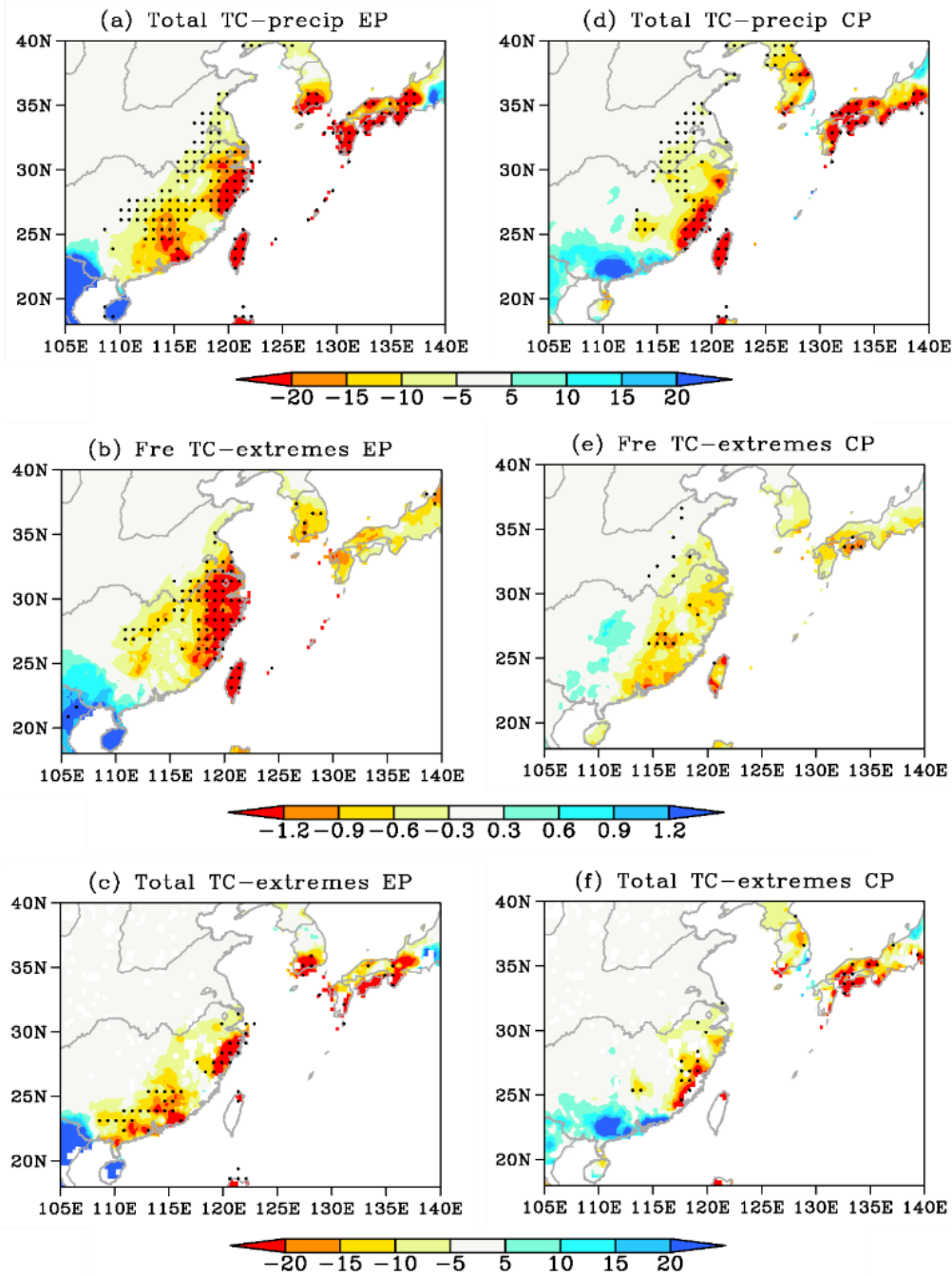


Figure 3.6 Extreme precipitation anomalies associated with TCs during the following JJA of the (a–c) EP and (d–f) CP El Niño events. (a, d) TCs-induced total precipitation (shading; units: mm season^{-1}), (b, e) TCs-induced extreme precipitation frequency (shading; units: days season^{-1}), (c, f) TCs-induced total accumulated extreme precipitation (shading; units: mm season^{-1}). Black dots indicate the signals passing the 90% significance level.

3.2.2 Non-TC precipitation during EP and CP El Niño

The distribution of non-TC extreme precipitation in JJA can be obtained after removing TC-related data (**Figure 3.7a**). It is clear that the spatial pattern of non-TC extreme precipitation is almost the same as that due to the total precipitation, indicating that non-TC extreme rainfall is the main contributor to the total. Results are similar when comparing non-TC total extreme precipitation to that due to total rainfall for EP and CP El Niño (**Figure 3.7b and 3.7c and Figure 3.3a and 3.3f**). This further indicates that TCs play a negligible role in determining large-scale extreme precipitation.

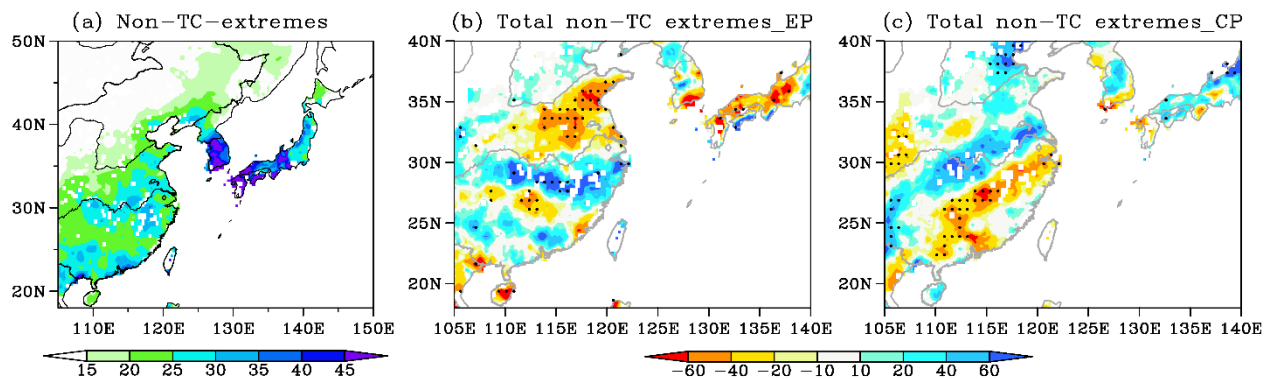


Figure 3.7 (a) Same as Figure 3.2 except for non-TC extreme precipitation. (b), (c) same as Figure 3.3(a), (b) except for non-TC related extreme precipitation during (b) EP, (c) CP El Niño in JJA(1).

Table 3.1 presents the *RR* of JJA extreme precipitation in SYR and MBC for EP vs. CP El Niño. In the *RR* equation (refer to **Chapter 2**), $P(E)$ ($P(E')$) represents the ratio of days with daily precipitation exceeding the 95th percentile climatology for a specific region during the decay summer of CP (EP) El Niño, to the total number of wet days observed during CP (EP) El Niño decay summers. It is important to note that the specific region referred to here can

either be SYR or MBC. RR is 1.45 for extreme precipitation over SYR, which indicates that its probability of occurrence in this area during EP El Niño is 45% larger than that during CP El Niño. For MBC, RR is found to be 0.66, which indicates that the probability of extremes during EP El Niño is 34% less than that during CP El Niño. All probabilities of extreme precipitation occurring in those regions pass the 90% significance level via the chi-square test.

The daily precipitation PDF based on gamma distribution over SYR (MBC) during EP and CP El Niño is further studied (**Figure 3.8**). The goodness fit of the SYR (MBC) PDF to the gamma distribution during EP and CP El Niño is first examined. The peak value of SYR (MBC) daily precipitation PDF during EP (CP) El Niño is less than that during CP (EP) El Niño, which indicates more light rainfall events during CP (EP) El Niño. In addition, the more right-skewed SYR (MBC) daily precipitation PDF under the influence of EP (CP) El Niño indicates more intense extreme precipitation events, with the 95th percentile being 18.2mm/day (13.7mm/day) during EP El Niño and 16.3mm/day (15.8mm/day) during CP El Niño, respectively.

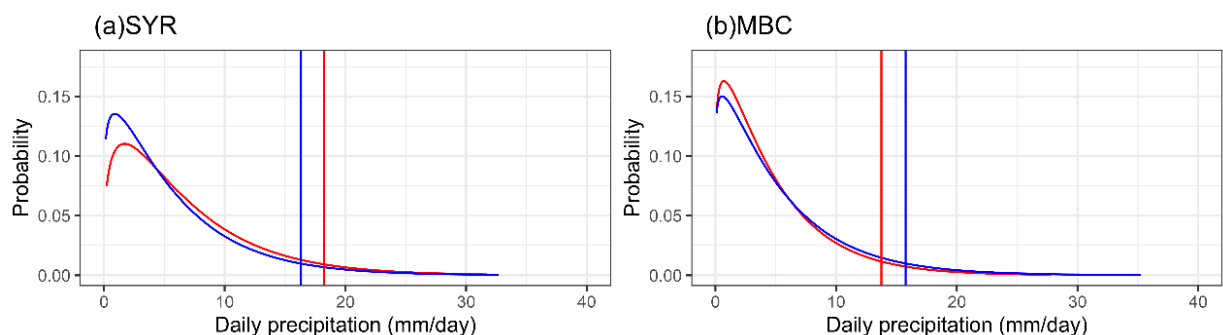


Figure 3.8 Daily precipitation probability density function (PDF) based on gamma distribution during EP (red curve) and CP El Niño (blue curve) events over (a) SYR and (b) MBC. The 95th percentile values of the daily precipitation associated with EP (CP) El Niño are indicated by red (blue) vertical lines in (a) and (b), respectively.

3.3 Mechanisms of non-TC extreme precipitation changes during EP and CP

El Niño

3.3.1 Circulation associated with non-TC extreme precipitation

Circulation patterns during days of extreme precipitation over SYR and MBC are now examined. We first calculate the daily precipitation over SYR (MBC) by averaging precipitation over 110°E – 122°E , 25°N – 30°N (see the red box in **Figure 3.3a–b**) (110°E – 135°E , 32°N – 36°N (see the blue box in **Figure 3.3a–b**)). The climatology of 95th percentile daily precipitation averaged over SYR (MBC) is found to be 16.5mm/day (14.9mm/day). These values are used as thresholds to extract the typical circulation features associated with extreme precipitation in these regions; whenever the corresponding daily precipitation exceeds the threshold, circulation maps for that particular day are archived. We now inspect the composite circulation anomalies based on these archived maps. For non-TC precipitation, when extreme precipitation events occur over SYR, an anticyclonic anomaly at 850 hPa over SCS can be found (not shown). This acts to bring abundant moisture from the WNP basin to SYR (**Figure 3.9a**), feeding the persistent heavy Mei-Yu rainfall here. In the mid-troposphere, obvious upward motion can be seen over SYR (**Figure 3.9b**). In contrast, when extreme events occur in MBC, the anomalous anticyclone is located more to the north (not shown), which contributes to heavy Mei-Yu rainfall in MBC. There is also strong upward motion over MBC at 500 hPa (**Figure 3.9e**). In addition, northerly winds can be observed when extreme events occur both over SYR and MBC (**Figure 3.9a and 3.9d**), which presumably can lead to a stronger Mei-Yu rain belt by cold air advection.

In the upper level, the WJ is enhanced south of 40°N when extreme precipitation occurs over SYR (**Figure 3.9c**); the WJ feature, however, is located more to the north during extreme events in MBC (**Figure 3.9f**). Note that the location of SAH when extreme precipitation occurs over SYR (**Figure 3.9c**) is more to the south compared to MBC extremes (**Figure 3.9f**). Still, SAH in both cases is westward displaced relative to climatology (blue contour in **Figure 3.9c and 3.9f**). Previous studies show that Mei-Yu precipitation can be influenced by the placement of these circulation elements (Sampe and Xie 2010; Cai et al. 2017; Wei et al. 2017). To the south of WJ, intense precipitation is induced due to the upward motion to the south of the jet entrance (Sanders and Hoskins 1990; Liang and Wang 1998; Zhang and Zhao 2004; Li et al. 2021d). Liu et al. (2020) indicate that the Mei-Yu front activity is closely related to the SAH placement. In particular, the eastward extension of SAH and the westward extension of WPSH together contribute to abundant moisture supply and induced upward motion over the Yangtze River area. Our study found that the southward (northward) displaced SAH is accompanied by the southward (northward) extension of WJ (**Figure 3.9c and 3.9f**). 105°E–125°E averaged meridional overturning circulation during SYR (MBC) extremes are shown in **Figure 3.10**. When extreme precipitation occurs over SYR (MBC), the southward (northward) extension of SAH is accompanied by the southward (northward) displacement of an upward branch of secondary circulation in 20°N–30°N (30°N–38°N), which induces the Mei-Yu rainfall over SYR (MBC) (**Figure 3.9b and 3.9e**). Downward motion can be found in the latitude of 10°N–20°N (20°N–30°N) during extremes over SYR (MBC), acting to strengthen the WPSH in the low levels (**Figure 3.9a and 3.9d**), The latter of which is the principal element for moisture supply from WNP to SYR (MBC).

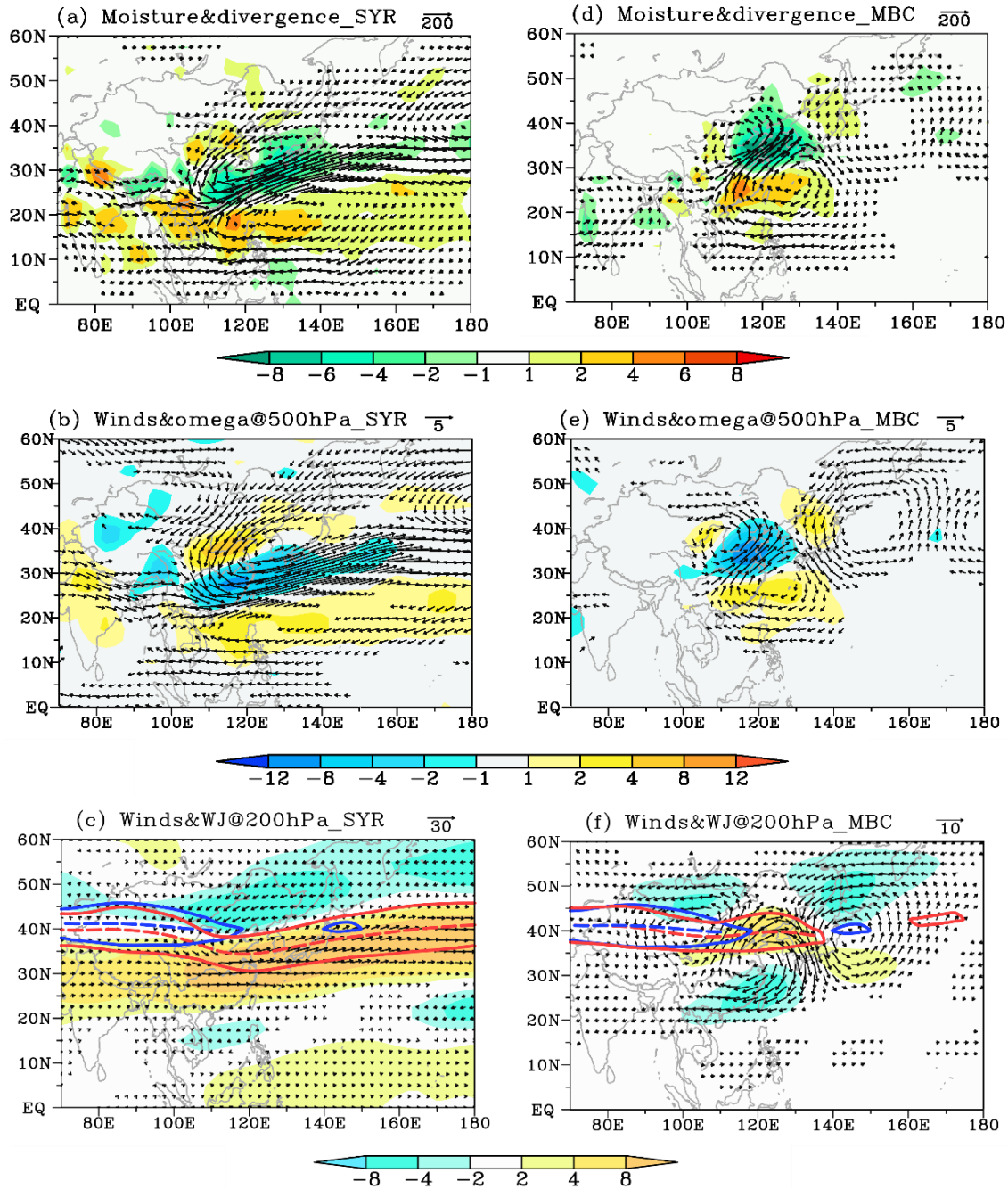


Figure 3.9 Anomalous lower- and upper-level atmospheric circulations associated with the extreme precipitation days in JJA over (a–c) SYR and (d–f) MBC. (a, d) Anomalous vertically integrated moisture flux (vectors; units: $\text{kg m}^{-1} \text{s}^{-1}$) and its divergence (shading; units: mm day^{-1}); only moisture flux anomalies $> 20 \text{ kg m}^{-1} \text{s}^{-1}$ are shown. (b, e) Anomalous 500 hPa wind (vectors; units: m s^{-1}) and pressure velocity (shading; units: $10^{-2} \text{ Pa s}^{-1}$); only vectors with

magnitudes greater than 1 m s^{-1} are shown. (c, f) Anomalous 200 hPa wind (vectors; units: m s^{-1}) and its zonal component (shading; units: m s^{-1}); only vectors with magnitudes greater than 1 m s^{-1} are shown. The solid red line and red dashed line in (c, f) represent the contours of 25 m s^{-1} zonal wind at 200 hPa and the WJ axis for the extreme precipitation days over (c) SYR and (f) MBC in JJA, the blue lines represent the same for climatology.

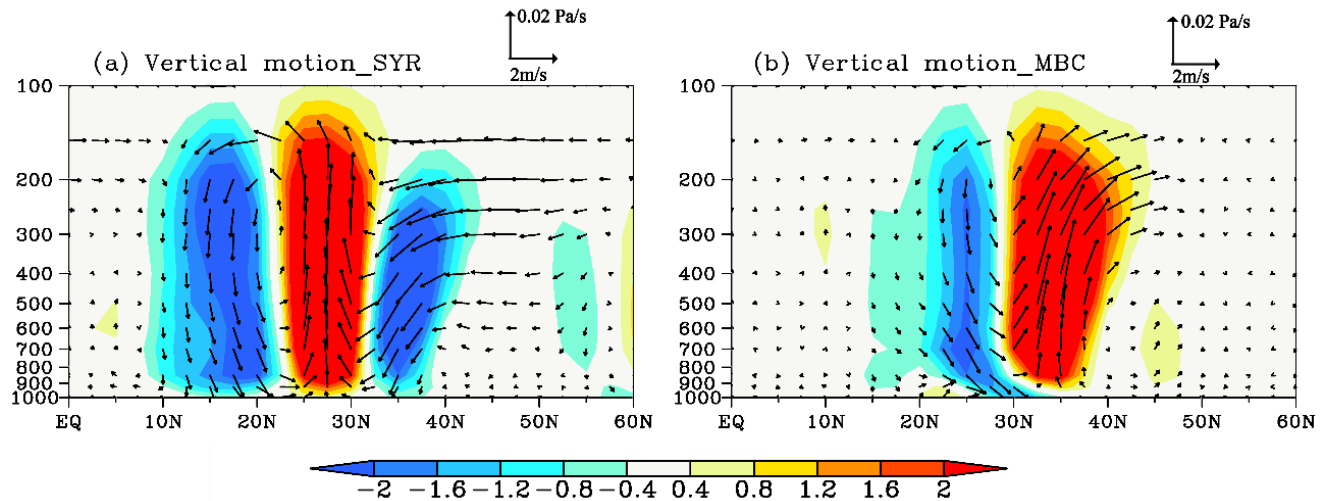


Figure 3.10 Anomalous local Hadley circulation (vectors; meridional wind and vertical pressure velocity, see scale arrow at upper right) and pressure velocity composites (shading; units: $10^{-2} \text{ Pa s}^{-1}$) averaged over 105°E – 125°E for the extreme precipitation days in JJA over (a) SYR and (b) MBC.

3.3.2 Circulation anomalies during EP and CP El Niño years

We now examine how the two types of El Niño can affect extreme precipitation over SYR and MBC and the related large-scale circulation changes. A low-level anticyclone over SCS (**Figure 3.11a**) and 500 hPa upward motion anomalies over SYR can be found during EP El Niño (**Figure 3.11b**), consistent with circulation patterns typically of SYR extreme precipitation (**Figure 3.9a**). In contrast, during CP El Niño, an anomalous anticyclone is located more to the north (**Figure 3.11d**), with upward motion observed over MBC (**Figure 3.11e**). This is reminiscent of circulations during extreme precipitation in MBC (**Figure 3.9d**). These suggest that EP (CP) El Niño event provides favorable conditions of southward (northward) displacement of the WPSH, inducing southward (northward)-displaced Mei-Yu rainfall and higher probability of extreme events occurring over SYR (MBC). In addition, anomalous northerly winds in the lower level are found both during EP and CP El Niño, contributing to bringing cold airflow from the continent in high latitude to the south, which provides a favorable condition to the form of Mei-Yu rain belt and promotes the occurrence of extreme events over EA.

Figure 3.11c and 3.11f present winds at 200 hPa during EP and CP El Niño years. The results show that WJ is more to the south (north) than the normal in EP (CP) El Niño phase, providing the condition of southward (northward)-displaced WJ during days of extreme events over SYR (MBC). The location of SAH shows more to the south during EP El Niño than during CP El Niño, resulting in the southward extension of the Mei-Yu rainfall during EP El Niño.

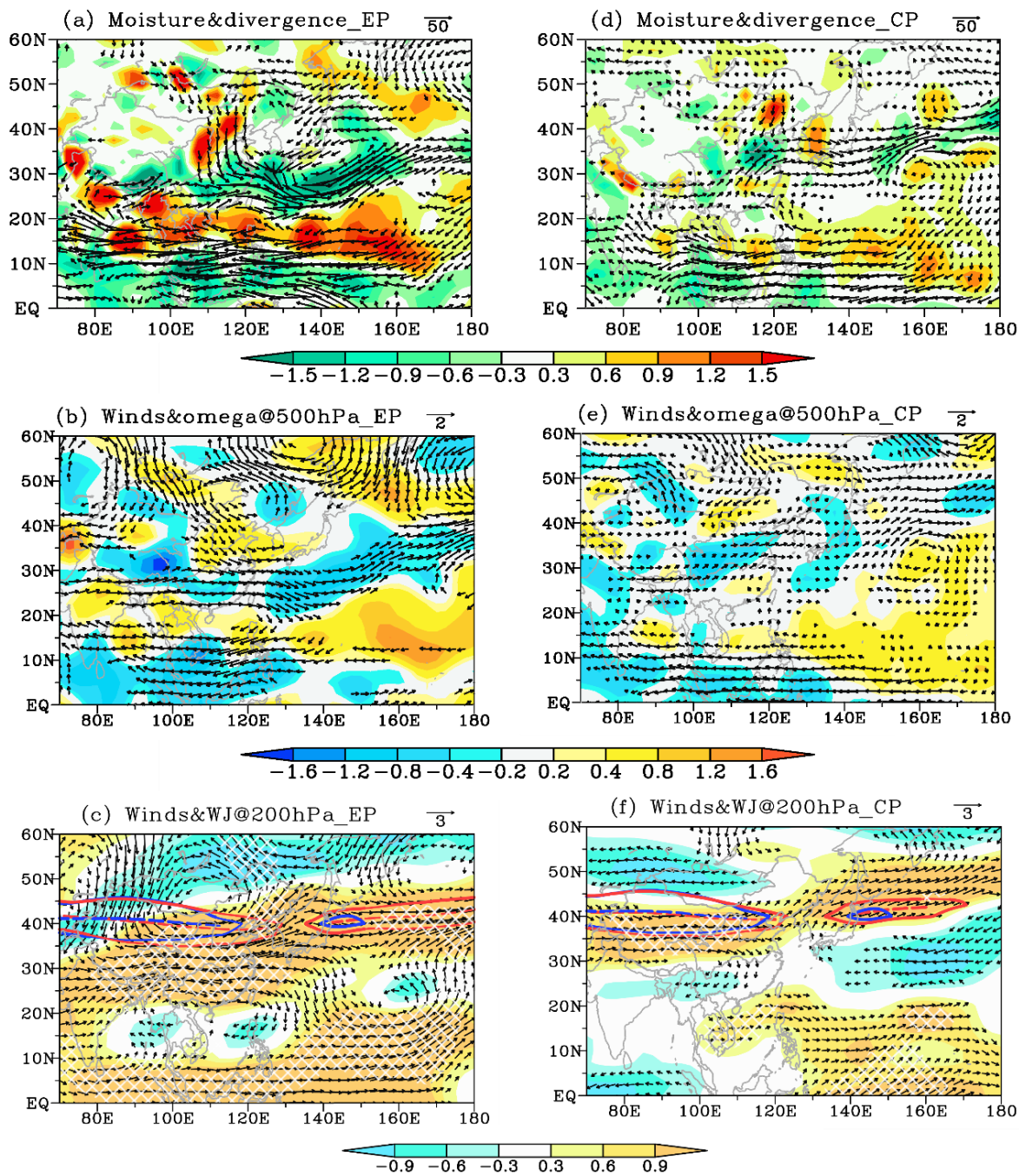


Figure 3.11 Same as Figure 3.9, except for the composites during the following JJA season of the (a–c) EP and (d–f) CP El Niño events. Only vectors with magnitudes greater than (a, d) 20 $\text{kg m}^{-1} \text{s}^{-1}$, (b, e) 0.2 m s^{-1} and (c, f) 0.5 m s^{-1} are shown. White crosses indicate that the signals of (a, d) moisture flux divergence, (b, e) pressure velocity and (c, f) zonal wind anomalies passing 90% significance level.

3.4 Summary

A number of previous studies have investigated the impacts of El Niño on extreme precipitation. They tend to focus on the statistical distribution of extreme precipitation and large-scale circulation patterns due to the two types of El Niño. However, how diverse El Niño impacts the occurrence of extreme precipitation over EA has attracted much less attention. This chapter emphasizes how EP and CP El Niño events affect the probability of occurrence of extreme precipitation over EA and the associated circulation anomalies.

It was found that, during EP and CP El Niño, changes in total summer extreme precipitation show the opposite spatial patterns. Enhanced extreme events are observed over SYR (MBC), and suppressed extremes are seen over MBC (SYR) during EP (CP) El Niño. Many studies proposed that EA summer extreme precipitation consists of two main components: TC precipitation and non-TC precipitation. Here we show that EA experiences less-than-normal TCs making landfall during both EP and CP El Niño, which is conducive to less TC precipitation over EA. One possible reason is that the enhanced WPSH impedes TC genesis in the WNP basin. TCs are found to have minimal influence on the total extreme precipitation pattern over EA, indicating that non-TC precipitation primarily controls EA summer extremes. Opposite patterns of non-TC extreme precipitation are found during two types of El Niño. Extreme precipitation tends to be even more intense over SYR (MBC) but less so over MBC (SYR) during EP (CP) El Niño.

Based on the opposite STR/MBC distribution of non-TC extreme precipitation in SYR and MBC during EP and CP El Niño, circulation changes associated with extreme precipitation

over SYR and MBC are investigated. When extreme precipitation occurs over SYR, southward displaced SAH, WJ, and anticyclonic anomaly over SCS can be observed, which is conducive to stronger Mei-Yu rainband in SYR. When extreme precipitation occurs over MBC, northward-displaced WJ and anticyclonic anomaly on the northerner side can be found, enhancing the Mei-Yu rainfall in MBC.

How EP and CP El Niño events can affect the risk of extreme precipitation and its associated circulations over SYR and MBC are also discussed. The frequency of occurrence of extreme precipitation and its related circulations over SYR (MBC) during EP (CP) El Niño is significantly higher than that during CP (EP) El Niño phase. During EP El Niño, southward displaced SAH, WJ, and a lower-level anticyclonic anomaly over SCS can be found. This is consistent with the circulations associated with SYR extreme precipitation, suggesting that such circulation features facilitate more extreme Mei-Yu rainfall in SYR. During CP El Niño, northward displaced WJ and an anomalous anticyclone over the north of SCS can be observed. Such circulation patterns similar to those might induce higher frequency of heavy Mei-Yu rainfall in MBC.

Figure 3.12 presents the SSTAs in decaying summer during EP and CP El Niño. Warm SSTA over tropical IO region (see red box in **Figure 3.12a**) can be found during EP El Niño. The displacement of SAH directly modulated by tropical IO warming has been proposed by previous works (Huang et al. 2011; Chen et al. 2016; Liu and Duan 2017). They suggest that warm SST in tropical IO region can lead to anomalous equivalent potential temperature in the atmospheric boundary layer, resulting in heating that can elevate low-latitude geopotential

height in the upper level. Stronger and southward displaced SAH can then displace WJ southward. Due to the abnormal upward induced by the displacement of the jet axis in the upper level, a southward extension of the anticyclonic anomaly in the lower troposphere and Mei-Yu rainfall can be observed. In contrast, warm SSTA can be observed over MC (see blue box **Figure 3.12b**), but not over the tropical IO during CP El Niño. Without the IO warming, SAH is more to the north than EP El Niño; the northward displacement of the upward and downward motion can be found, which causes Mei-Yu rainfall over MBC.

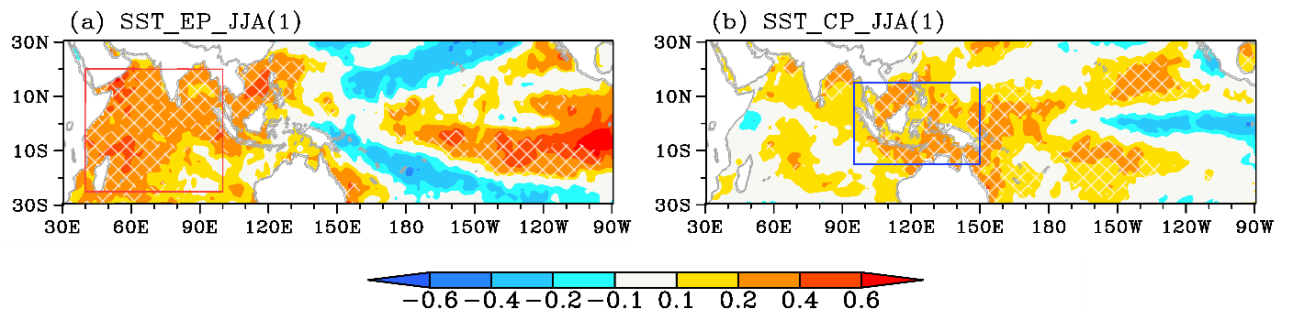


Figure 3.12 SSTA composite (shading; units: $^{\circ}\text{C}$) during the following JJA of the (a) EP and (b) CP El Niño events. The red box in (a) and the blue box in (b) denote the tropical IO and MC, respectively. The white crosses indicate that signals pass the 90% significance level.

We further analyze the mechanism that leads to SST warming over MC during CP El Niño in subsequent summer. During decaying spring of CP El Niño, an anticyclonic anomaly is observed over WNP, which extends westward to approximately 80°E (**Figure 3.13**). This broad anticyclonic circulation anomaly results in significant positive downward short wave radiation flux on its southern side (**Figure 3.13a**) and persists until following summer (**Figure 3.13b**). Consequently, this persistent circulation pattern further contributes to the SST warming in the

MC region. The observed SST warming in MC, in turn, plays a role in maintaining the anticyclonic anomaly over WNP by modulating the local Hadley circulation.

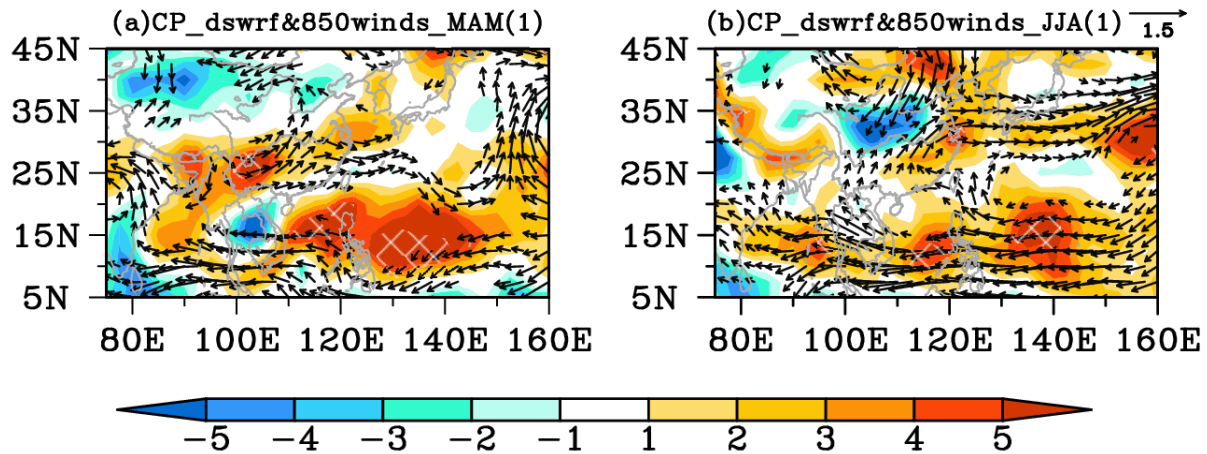


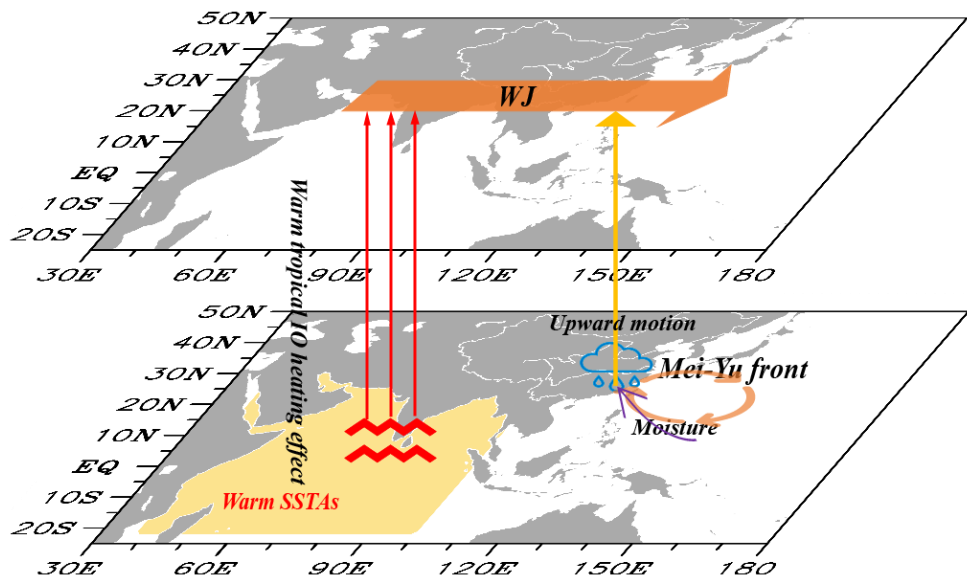
Figure 3.13 Anomalous downward short wave radiation flux (shading; units: W/m^2) and 850 hPa wind (vectors; units: m s^{-1}) during CP El Niño in subsequent spring and summer. Only vectors with magnitudes greater than 0.2 m s^{-1} are shown. The white crosses indicate that signals of downward short wave radiation flux pass the 90% significance level.

The possible mechanism of two types of El Niño affecting extreme precipitation can be summarized in **Figure 3.14**. During EP El Niño, the southward extension of SAH at 200 hPa is forced by warm SSTA over tropical IO via heating troposphere, which causes the southward displacement of WJ (**Figure 3.14a**). The southward displaced secondary circulation can be found in the south of the jet axis, with upward motion in 25°N – 30°N and downward motion in 25°N – 30°N and 30°N – 38°N individually, which causes anticyclonic anomaly over SCS and Mei-Yu front over SYR. The upward motion can accelerate the convergence over SYR in the south of the jet entrance. Meanwhile, the downward motion branch in low latitude enhances the WPSH in the lower troposphere, which can bring abundant moisture from the WNP basin

to SYR via southwesterly winds. During CP El Niño (**Figure 3.14b**), the location of SAH is more to the north than that of EP El Niño since the warm SSTAs over IO almost disappear and positive SSTAs over MC can be found. Northward jet WJ is related to Hadley circulation anomalies, with the upward motion branch in 30°N – 40°N . The convergence is more likely to occur in MBC, where the upward motion can be found. At the same time, the northward displaced WPSH anomaly in the lower troposphere causes a high risk of moisture transported to MBC.

In this chapter, we focus on interpreting how EP and CP El Niño events affect the circulations related to non-TC summer extreme precipitation over EA. The observed results indicate that EP (CP) El Niño provides a favorable (unfavorable) condition for extreme rainfall over SYR (MBC) by modulating the location of anticyclonic anomaly over WNP. Whether the EA extreme rainfall and its related mechanisms obtained from observed results can be captured by modern coupled models will be stressed in **Chapter 4** and **Chapter 5**.

a) EP_JJA(1)



b) CP_JJA(1)

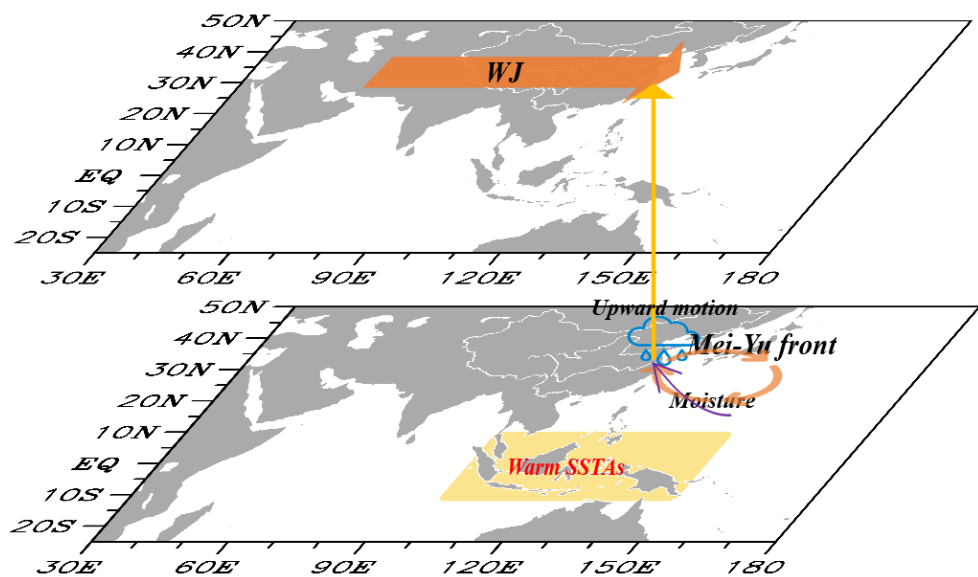


Figure 3.14 Schematic diagram illustrating the mechanism for causing extreme precipitation changes over SYR and MBC during the following JJA season of the (a) EP and (b) CP El Niño events.

Table 3.1 Risk Ratio (*RR*) of JJA extreme precipitation during EP versus CP El Niño over SYR and MBC.

Region/Season	<i>RR</i>	P value
SYR/JJA	1.45	0.037
MBC/JJA	0.66	0.06

4 Evaluating CMIP6 in simulations of spring extreme precipitation over EA

Chapter 3 examines the changes in extreme summer precipitation over EA. Extreme rainfall also occurs in spring and is a significant contribution to the annual total. In this chapter, we first delve into mechanisms behind spring (March–April–May (MAM)) extreme rainfall over EA and identify an index in relation to such extremes. In addition, using simulations from 20 CMIP6 models (as listed in **Table 2.1**), we evaluate state-of-the-art coupled models' ability to reproduce EA spring extreme precipitation and associated dynamic processes. Finally, we assess the bias of these models.

4.1 Spring extreme precipitation over EA based on observations and CMIP6 models

The springtime precipitation characteristics over EA from observations and models are first inspected. **Figure 4.1** presents the spatial patterns of the seasonal mean precipitation (**Figure 4.1a and 4.1b**) and rainy extreme (**Figure 4.1c and 4.1d**) based on observations (**Figure 4.1a and 4.1c**) and the multi-model ensemble (MME) mean for 20 CMIP6 models (**Figure 4.1b and 4.1d**). The observed spatial distribution of spring seasonal mean (**Figure 4.1a**) and extreme precipitation (**Figure 4.1c**) in EA exhibits a similar pattern, with intense precipitation concentrated in Southern China (SC, 112°E–122°E, 22°N–26°N), the Yangtze River Basin (YRB, 112°E–122°E, 26.5°N–34°N), and South Korea and South Japan (SK–SP, 125°E–140°E, 31.5°N–36°N). The MME mean is generally able to reproduce these patterns, although it underestimates the extreme precipitation in SC and SK–SP.

Here, we further focus on the southern EA region (SEA, encompassing the SC, YRB, and SK-SP regions), where the observed 95th percentile value is more than 30mm/day in most grid boxes in the area. Physical processes leading to extreme precipitation in SEA, using observations and CMIP6 historical simulations, will be investigated.

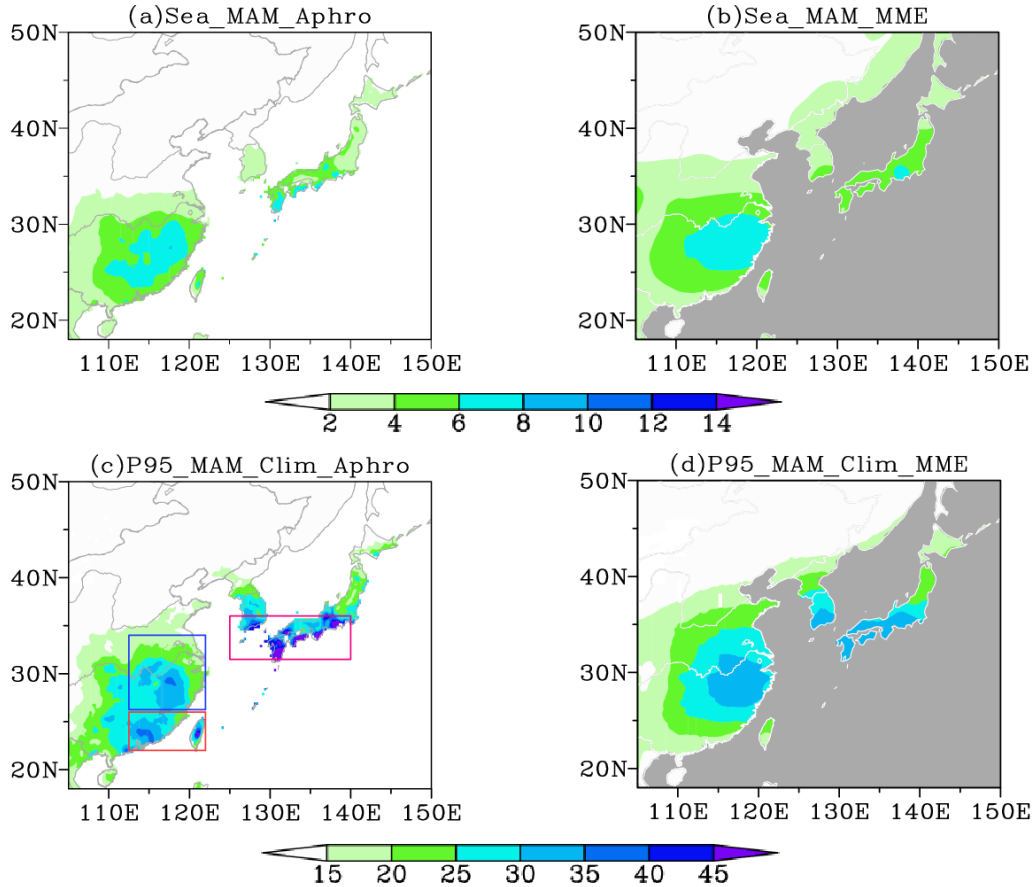


Figure 4.1 (a, b) Seasonal precipitation mean (shading; units: mm day^{-1}) and (c, d) climatology of the 95th percentile of daily precipitation (shading; units: mm day^{-1}) during the MAM season based on (a, c) APHRODITEv1101 and (b, d) MME mean of 20 models.

4.2 The circulations related to extreme precipitation over SEA

To unveil circulation patterns related to extreme precipitation over SEA and to assess CMIP6 models' performance, SEA daily precipitation is first computed by area-averaging precipitation for identifying all extreme precipitation events. Note that the SEA region refers to SC, YRB, and SK–SP (**Figure 4.1c**); the 95th percentile of daily area-averaged precipitation (see **Chapter 2**) in MAM is used as the threshold for an extreme event. The daily precipitation exceeding this threshold is identified as an extreme event. The circulations corresponding to the SEA extreme precipitation events are then achieved and further inspected. **Figure 4.2** depicts the composite anomalies of SEA extreme precipitation-day (extreme-day, hereafter) moisture flux and its divergence obtained using observations (**Figure 4.2a**) and MME mean (**Figure 4.2b**). It can be seen that CMIP6 MME well captures the observed anomalies of extreme-day moisture transport, with moisture convergence over SC–SK–SP associated with the low-level southwest airflow from the East Bay of Bengal (EBOB). However, in the YRB region (especially the north of YRB), there is less moisture convergence and even divergence based on both observations and the MME mean. It indicates that the spring extreme rainfall over YRB is less affected by moisture transport.

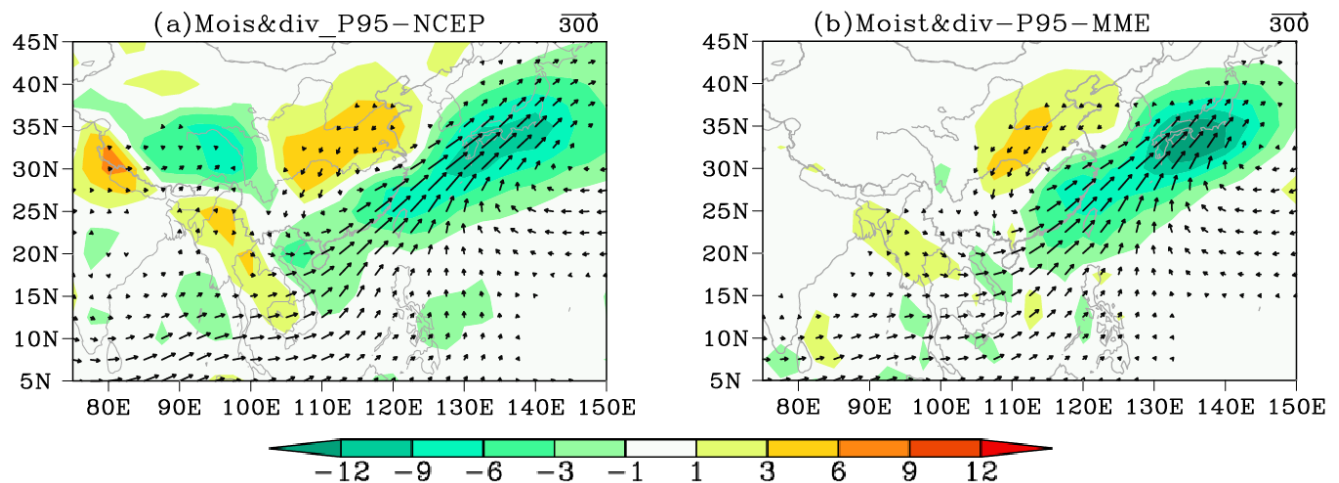


Figure 4.2 The anomalies of vertically integrated moisture flux (vectors; units: $\text{kg m}^{-1} \text{s}^{-1}$) and its divergence (shading; units: mm day^{-1}) associated with the extreme precipitation days in MAM over SEA based on (a) NCEP reanalysis data and (b) MME mean of 20 models; only moisture flux anomalies $> 20 \text{ kg m}^{-1} \text{s}^{-1}$ are shown.

Previous studies have indicated that the strong atmospheric baroclinic instability caused by the increased meridional temperature gradient is a significant contributor to heavy precipitation over EA (Vaid and San Liang 2015; Song and Ahn 2022). Here, the meridional temperature gradient anomalies at 850 hPa on extreme-day are investigated in both observations (**Figure 4.3a**) and MME (**Figure 4.3b**, see **Figure A5** for each model), with a typical tri-pole pattern characterized by positive anomalies centered in SCS and northern China and negative anomalies over the Yangtze River. This anomalous temperature gradient pattern indicates southward (northward)-shifting cold (warm) advection originating from Northern China (the low latitude). When extreme rainfall occurs in SEA, we observe a typical "cold-warm temperature advection (TA) dipole" pattern at 850 hPa over EA, with a low-level cyclonic

anomaly over SEA (**Figure 4.4a**) that is well-captured by MME mean (**Figure 4.4b**, see **Figure A6** for each model). Therefore, the cold-warm TA dipole due to the increasing local temperature gradient plays a leading role in spring extreme precipitation over SEA in both observations and the CMIP6 models. The warm advection is due to the warm, moist airflow brought by the southwest airflow from the EBOB, while the cold advection is related to the southward shift of cold airflows from Northern China.

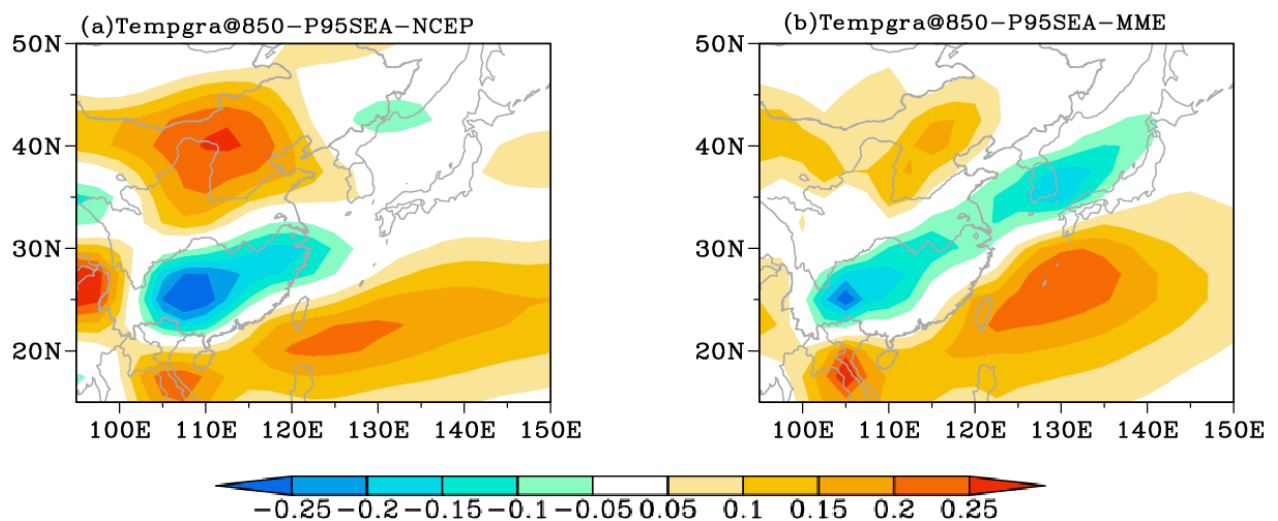


Figure 4.3 Same as Figure 4.2, but for 850 hPa meridional temperature gradient (shading; units: $^{\circ}\text{C m}^{-1} \times 10^{-5}$).

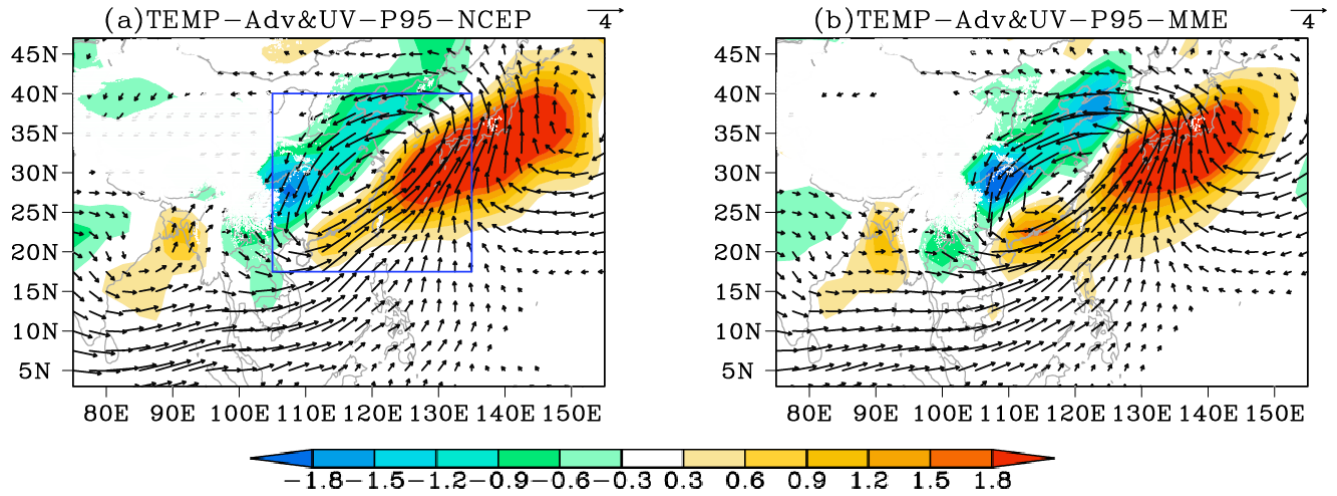


Figure 4.4 Same as Figure 4.2, but for 850 hPa wind (vectors; units: m s^{-1}) and temperature advection (shading; units: $^{\circ}\text{C day}^{-1}$); only vectors with magnitudes greater than 0.5 m s^{-1} are shown.

To further examine the daily temperature advection and its variability, EOF analysis is conducted over the area of 105°E – 135°E , 17.5°N – 40°N (shown in the blue box in **Figure 4.4a**) in MAM. Before applying EOF analysis to temperature advection fields, the fields are initially detrended in order to eliminate long-term variations caused by global warming effects. Our subsequent study demonstrates that whether or not the temperature advection fields are detrended has minimal influence on general behaviors of their associated circulations. The leading two EOF modes from observations (**Figure 4.5a**) and MME mean (**Figure 4.5b**) show a mono pole temperature advection pattern (EOF1 TA mode, not shown) and a dipole temperature advection pattern (EOF2 TA mode), respectively. It is noteworthy that EOF2 TA mode has features similar to the temperature advection pattern during extreme rain days (**Figure 4.4**), albeit with a slight northward displacement. For CMIP6 models, only those with

missing values occupying less than one-half of grid points in the domains are considered for EOF analysis. The resulting MME mean of EOF2 patterns is shown in **Figure 4.5**. Individual models' results indicate that they can generally capture the observed EOF2 TA mode, compared EOF2 in each model with MME mean temperature advection, as in **Figure A7**. Since the EOF2 TA mode is very similar to the extreme-day temperature advection pattern, SEC extreme precipitation is likely to be highly correlated with the EOF2 TA mode. To quantify the EOF2 TA mode, we define the normalized nonlinear principal component of the EOF2 TA mode, an index with synoptic-scale variability, as the temperature advection index (TAI).

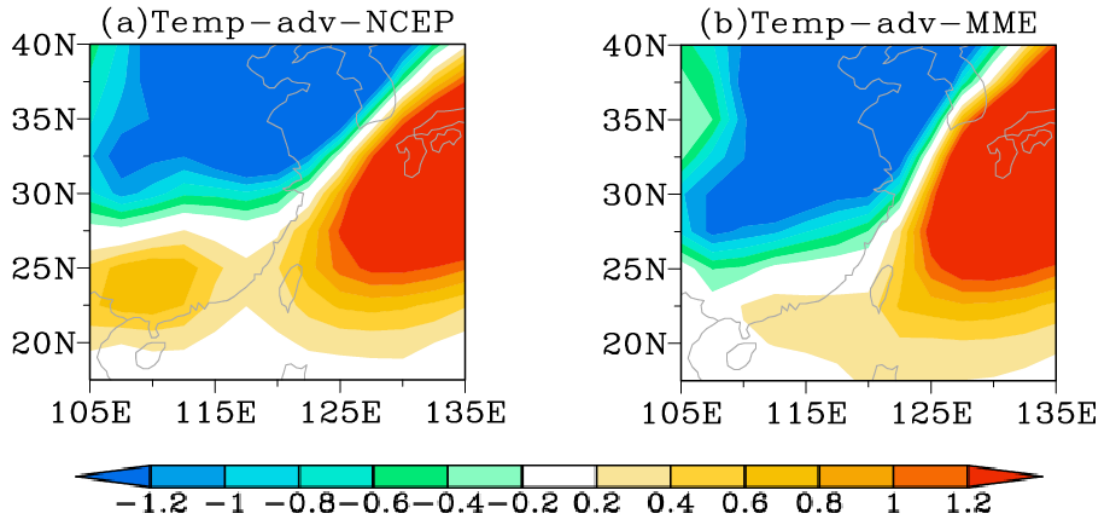


Figure 4.5 EOF2 mode of daily temperature advection (shading; units: $^{\circ}\text{C day}^{-1}$) at 850 hPa based on (a) NCEP reanalysis data and (b) the MME mean of 20 models.

To further examine the association between SEA spring precipitation and EOF2 TA mode, we regress the daily rainfall in MAM onto the TAI. Observations (**Figure 4.6a**) and MME mean (**Figure 4.6b**) show significantly above-normal daily rainfall over YRB–SK–SP. Note that there is little change in precipitation over SC, probably due to the fact that the EOF2 TA mode

centers of action are located slightly further north. Although CMIP6 models can generally capture the observed spatial distribution of precipitation, their patterns exhibit a slight eastward shift when compared to observations. In general, the YRB and SK-SP regions, where significantly increasing precipitation is found, are strongly affected by the EOF2 TA mode. However, intense precipitation in SC is likely to be more related to moisture transported from EBOB but less influenced by mid-latitude dynamics. These results from observations and CMIP6 models suggest that TAI can be an index to represent springtime extreme rainfall due to synoptic-scale activities.

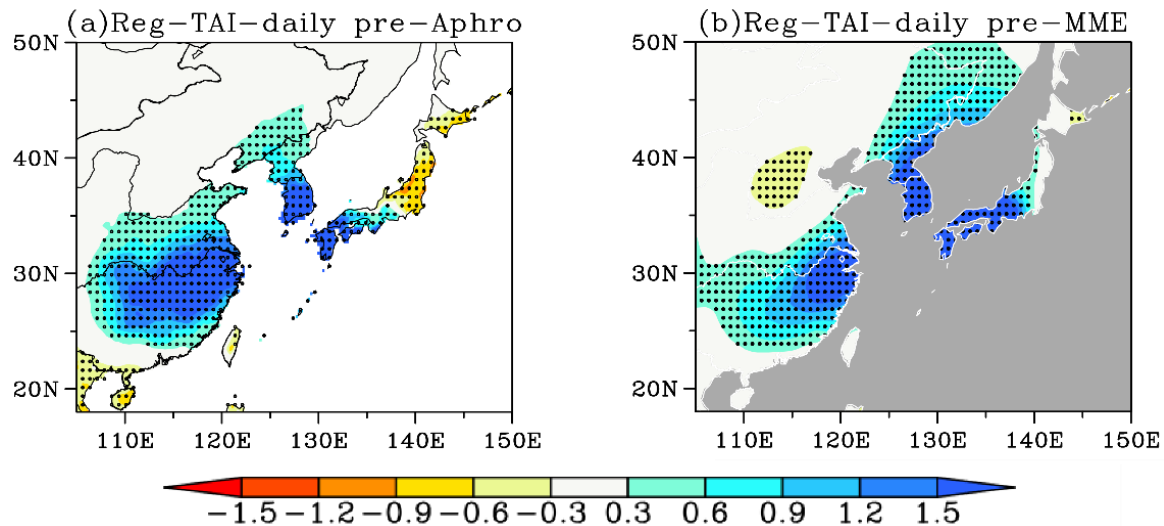


Figure 4.6 Regression map of March–May daily precipitation (shading; units: mm day^{-1}) on TAI based on (a) APHRODITEv1101 and (b) MME mean of 20 models. Black dots in (a) indicate the signals passing the 95% significance level. Black dots in (b) indicate locations over which more than 70% of models agree on the sign of precipitation anomalies between MME and each model.

The results from **Figure 4.6** indicate a significant positive correlation between TAI and daily precipitation over YRB-SK-SP, which is evident in both observational data and model

simulations. **Table 4.1** illustrates the correlation coefficients between TAI and YRB–SK–SP daily rainfall in observations and each model, and also presents the correlation coefficients between TAI and YRB–SK–SP daily rainfall during extreme precipitation days. Observational and simulated results both indicate a highly linear positive correlation between TAI and daily rainfall amount. However, only considering extreme precipitation events, this linear relationship significantly weakens, and in observations and some models, even exhibits a negative correlation.

Next, we further investigate the relationship between TAI and YRB–SK–SP extreme rainfall. **Figure 4.7** shows the relationship between TAI and YRB–SK–SP extreme precipitation in both observations and CMIP6 models. The findings suggest that, despite the absence of a significant linear relationship, a significant number of extreme precipitation events coincide with the positive phase of TAI. This indicates that TAI primarily influences the frequency of extreme precipitation occurrences rather than their intensity. Additionally, **Figure 4.7** demonstrates that the majority of extreme precipitation events exhibit a concentration of daily rainfall amounts around the threshold of the extreme event. Consequently, when compared to the climatological sense of daily rainfall, the linear correlation between TAI and daily rainfall during extreme precipitation days is noticeably attenuated.

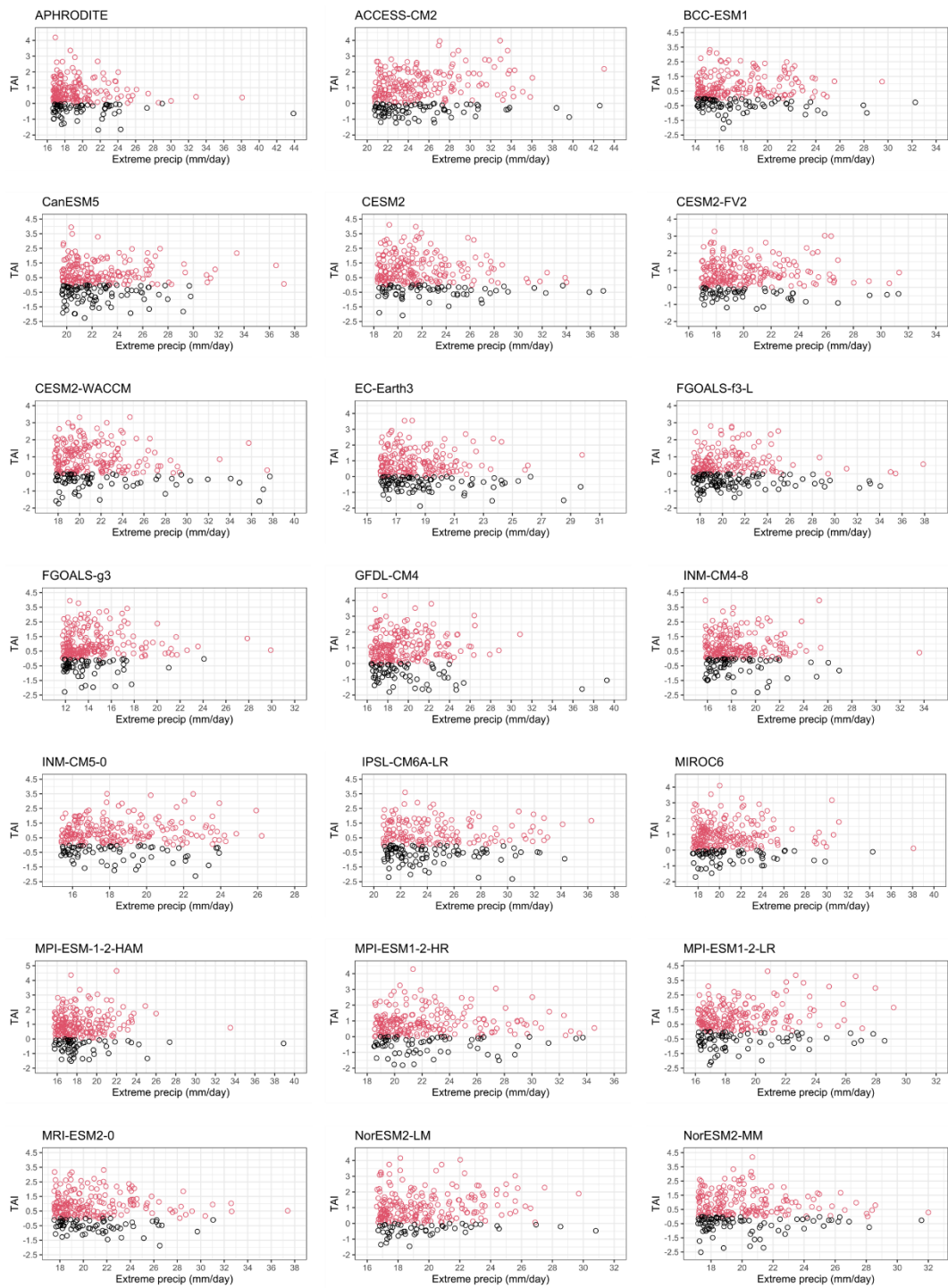


Figure 4.7 The linkage between TAI (Y-axis) and YRB–SK–SP daily rainfall (X-axis) during extreme precipitation days in observations and CMIP6 models. Red dots represent extreme precipitation events with positive phase of TAI; Black dots denote extreme precipitation events with negative phase of TAI.

We further investigate the relationship between extreme precipitation over YRB–SK–SP and TAI using the Z test to determine if there is any significant difference between extreme-day TAI and climatological TAI (all-day TAI). The daily precipitation over YRB–SK–SP is obtained by averaging the daily precipitation over that region (shown in the blue and pink boxes in **Figure 4.1c**) and the daily 95th percentile value is used as the threshold for an extreme event. Results from observations and each CMIP6 model show a significant positive relationship between TAI and extreme precipitation, with a P value far less than 0.01 (**Table 4.2**). Therefore, the TAI extracted from observations and models is not only an indicator of mean daily precipitation over YRB–SK–SP but can also capture sizable amount of variability related to precipitation extremes.

We now define a TAI-induced extreme event (TAI-extreme) to be an extreme event over YRB–SK–SP with TAI larger than zero. The proportion of TAI-extremes to all extreme events, referred to as the TAI-extreme ratio, is given in **Table 4.3**. TAI-extreme ratios in the observations and MME mean are found to be 0.72. For the 20 models, the TAI-extreme ratios range from 0.59 (FGOALS-f3-L) to 0.8 (MIROC6). Although the ratio for about half of the models is underestimated, 60% of TAI-extremes among all extreme events are identified, indicating that TAI-extremes are predominant in extreme precipitation events over YRB–SK–SP in the model environments.

4.3 Synoptic-scale circulation related to YRB-SK-SP extreme precipitation

To unveil the mechanism behind synoptic-scale extreme precipitation over YRB–SK–SP, we compare the TAI-induced daily circulation anomalies during the selected periods in MAM (TAI-all circulations, hereafter) and YRB–SK–SP extreme-day TAI-circulations (TAI-extreme 75

circulations, such as temperature, winds, geopotential height, etc., hereafter). Here the TAI-all and TAI-extreme circulation anomalies are obtained by regression using the all-day and extreme-day TAI, respectively.

To investigate the synoptic-scale mechanisms underlying the YRB–SK–SP extreme precipitation events, we compare the TAI-all circulations and TAI-extreme circulations in both observational data and CMIP6 model simulations. **Figure 4.8** depicts the 850 hPa TAI-all (**Figure 4.8a and 4.8d**), TAI-extreme (**Figure 4.8b and 4.8e**) temperature and winds, as well as the differences between the latter and the former (**Figure 4.8c and 4.8f**), based on observations (**Figure 4.8 a–c**) and MME mean (**Figure 4.8 d–f**).

Observed and simulated results indicate that the anomalous temperature at 850 hPa related to all events are characterized by cold and warm perturbations over Mongolia–Northern China and SC–SK–SP, respectively (**Figure 4.8a and 4.8d**). The lower-troposphere meridional temperature difference over EA resembles the EOF2 TA mode and is consistent with its relation with more-than-normal precipitation over YRB–SK–SP. Specifically, more precipitation over YRB is attributed to the encounter of the southward displacement of cold air from Mongolia–Northern China and warm airflow over YRB. Despite moisture flux divergence is found over YRB (**Figure 4.9a–b**), intense precipitation still occurs (**Figure 4.6**). The northward displacement of warm air temperature gradient from EBOB is conducive to moisture convergence over SK–SP through the southwesterly airflow, resulting in more precipitation over SK–SP (**Figure 4.9a and 4.9d**).

Moreover, compared with TAI-all circulation anomalies, observed and simulated results show

that the TAI-extreme circulations depict significantly decreased temperature over Mongolia–Northern China accompanied by enhanced northerly flow (**Figure 4.8c and 4.8f**). The strong northerly airflow originating from northern China is the primary factor driving more frequent frontal activity over YRB, which significantly increases the likelihood of extreme precipitation events in the YRB region. Additionally, TAI-extreme circulations in both observations (**Figure 4.9c**) and MME mean (**Figure 4.9f**) reveal the presence of anomalous cyclonic circulations over EA. The southwesterly airflow on the eastern side of this cyclonic circulation facilitates the transport of moisture from low latitudes to the SK–SP region, resulting in an excessive occurrence of extreme precipitation over SK–SP.

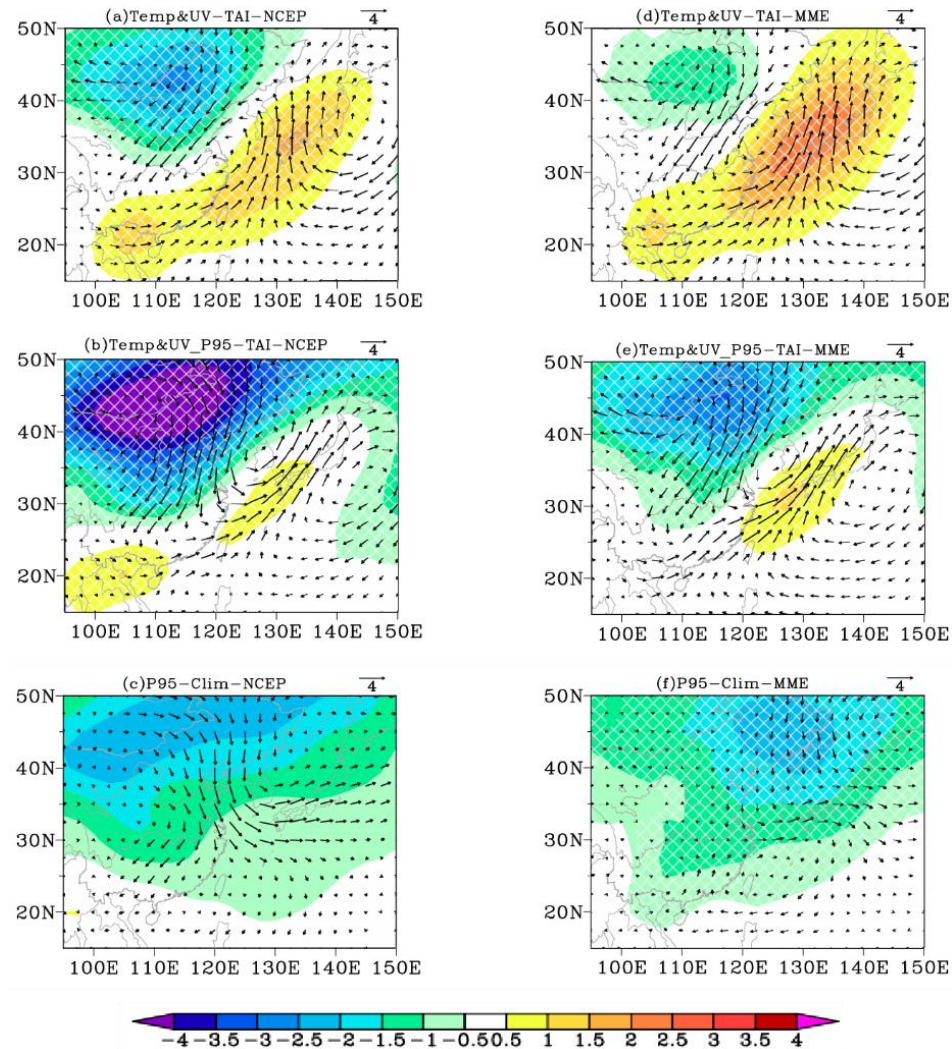


Figure 4.8 Anomalies of March–May 850 hPa daily temperature (shading; units: $^{\circ}\text{C}$) and 850 hPa daily wind (vectors; units: m s^{-1}) obtained by regressing onto (a, d) all-day TAI in MAM and (b, e) extreme-day TAI in MAM based on (a, b) NCEP data and (d, e) MME mean of 20 models. Differences between the TAI-extreme and TAI-all temperature (shading; units: $^{\circ}\text{C}$) and daily wind (vectors; units: m s^{-1}) based on NCEP data and MME mean of 20 models are given in (c) and (f), respectively; only vectors with magnitudes greater than 0.1 m s^{-1} are shown. The white crosses in (a, b) indicate that temperature anomalies pass the 95% significance level, and white crosses in (d, e) indicate locations over which more than 70% of models agree on the sign of temperature anomalies between MME and each model.

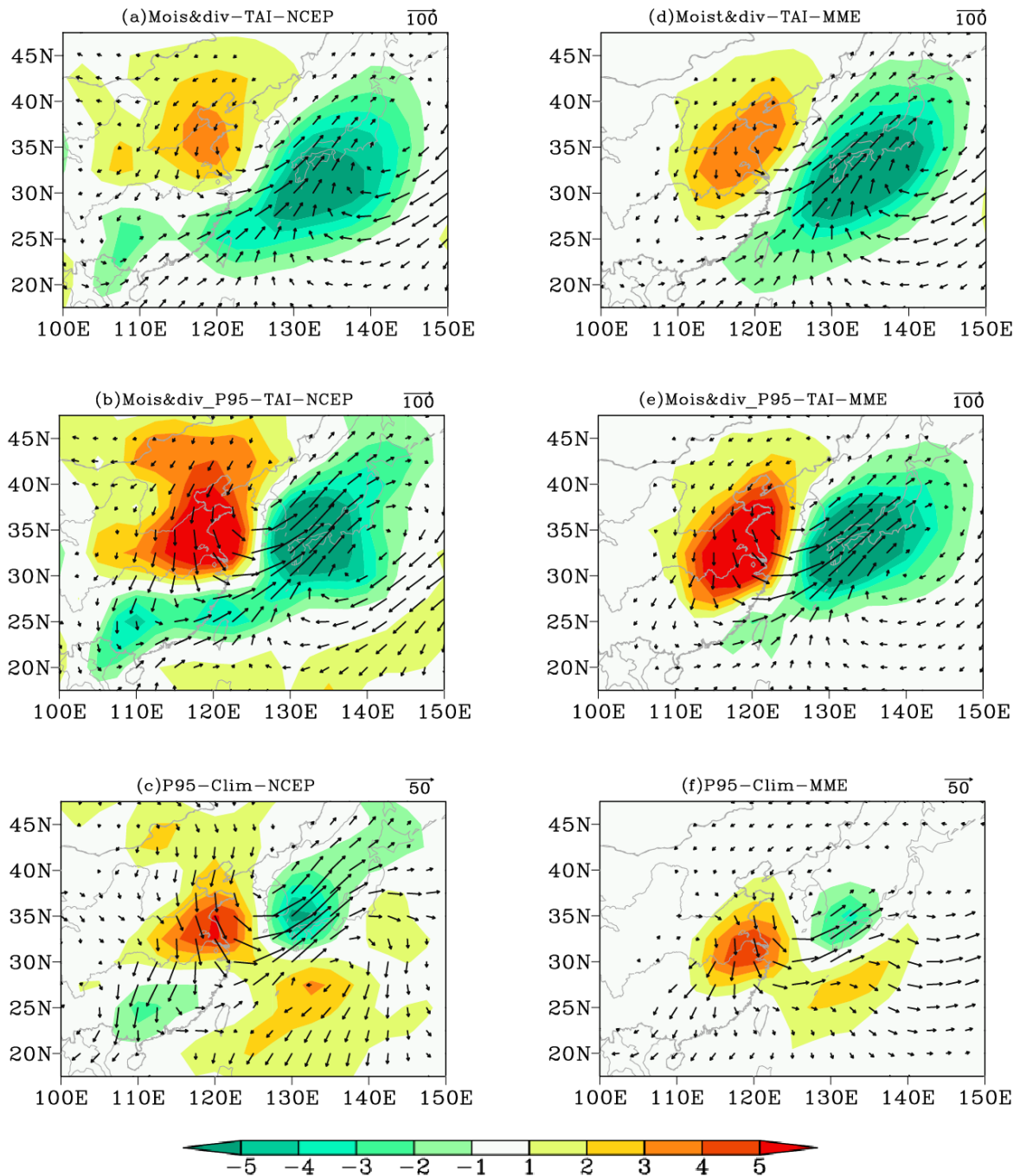


Figure 4.9 Same as Figure 4.8, but for vertically integrated moisture flux (vectors; units: $\text{kg m}^{-1} \text{s}^{-1}$) and its divergence (shading; units: mm day^{-1}). Only moisture flux anomalies greater than (a, b, d, e) $10 \text{ kg m}^{-1} \text{s}^{-1}$ and (c, f) $5 \text{ kg m}^{-1} \text{s}^{-1}$ are shown.

Upper-troposphere circulation anomalies linked to the EOF2 TA mode are further explored.

Figure 4.10 shows the 250 hPa geopotential height anomalies obtained by regressing onto all-day TAI (**Figure 4.10a and 4.10d**) and YRB–SK–SP extreme-day TAI (**Figure 4.10b and 4.10e**) based on observations (**Figure 4.10a–b**) and MME mean (**Figure 4.10d–e**). The observed and simulated results from TAI-all anomalies show wave features in geopotential height across Siberia, Mongolia, Northern China and reaching the Pacific (**Figure 4.10a and 4.10d**). The negative (positive) anomalies over Mongolia–Northern China (SC–SK–SP) contribute to shifting the cold air southward (warm air northward) in the lower troposphere (**Figure 4.8a and 4.8d**) with strengthened upper-troposphere trough. Compared to TAI-all geopotential height, observed and model-generated results show a significantly strengthened upper-troposphere trough over Mongolia–Northern China that extends even further to cover the entire Eurasian continent and Pacific for TAI-extreme anomalies. Although MME mean well captures these upper-level wave anomalies, the anomalies in MME mean are weaker than observations (**Figure 4.10c and 4.10f**), indicating the simulated extreme precipitation over YRB–SK–SP is less affected by synoptic-scale waves than observations. Overall, observations and MME mean show that EA extreme rainfall is deeply affected by synoptic-scale waves in upper troposphere.

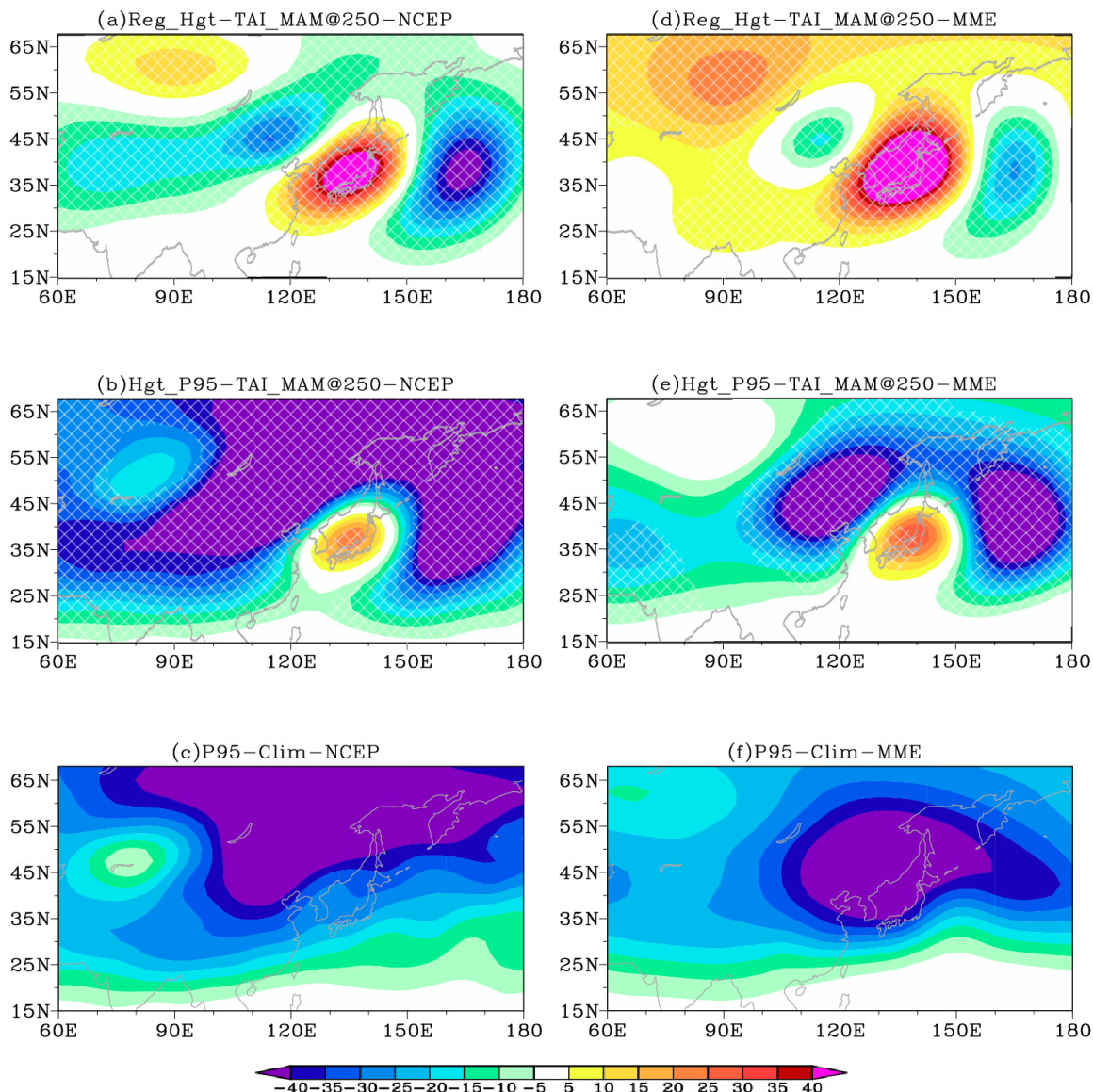


Figure 4.10 Same as Figure 4.8, but for 250 hPa geopotential height anomalies (shading, units: m)

4.4 Model bias for synoptic-scale precipitation over YRB-SK-SP

The findings in section 4.3 indicate that although the MME mean can generally capture synoptic-scale circulation anomalies, there are still biases present in the models. Specifically, the upper-level geopotential height pattern characterized by a wave train in the model-simulated TAI-all resembles the observations, but the magnitude between them differs (**Figure 4.10a and 4.10d**). Moreover, there are biases in moisture transport in the models. The models overestimate divergence over YRB, accompanied by northerly wind bias in this area. Conversely, there is a southwesterly wind bias that brings abundant moisture from the Pacific to the SK-SP region, resulting in an overestimated convergence in situ (**Figure 4.11**). The bias in simulated moisture convergence or divergence may cause an overestimation or underestimation of daily rainfall intensity, respectively.

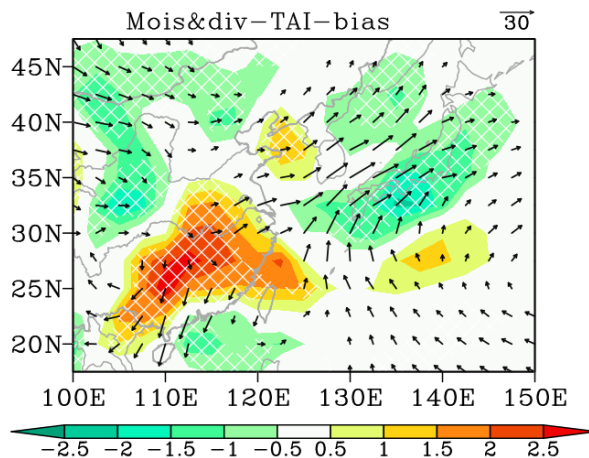


Figure 4.11 Biases of MME mean for TAI-all vertically integrated moisture flux (vectors; units: $\text{kg m}^{-1} \text{s}^{-1}$) and its divergence (shading; units: mm day^{-1}). Black dots in (a) indicate locations over which more than 80% of models agree on the sign of anomalies of daily precipitation biases between MME and each model. Only moisture flux anomalies greater than $5 \text{ kg m}^{-1} \text{s}^{-1}$ are shown.

4.5 Summary

In this chapter, we have discovered that synoptic-scale activities play a significant role in modulating extreme spring precipitation over EA, and we have provided an interpretation of the underlying physical processes involved. We use the 95th percentile values of daily precipitation from 20 CMIP6 models and observations from APHRODITE to identify extreme events. After examining the spatial distribution of spring extreme rainfall in observations and models, it has been found that the SEA region, which comprises SC, YRB, and SK-SP, experiences significant levels of extreme rainfall during this season. To better comprehend the mechanisms behind spring extreme precipitation over SEA, our initial focus is on examining the circulation patterns that are linked to such extreme rainfall events. Both observational data and MME mean indicate that the extreme precipitation over SEA is primarily a result of moisture being transported from the EBOB via southerly airflow. Furthermore, both observations and MME mean indicate that the 850 hPa temperature gradient associated with SEA extreme precipitation exhibits a tri-pole pattern, which is characterized by positive anomalies over SCS and northern China, and negative anomalies over YRB region. These anomalies in the 850 hPa temperature gradient promote the southward displacement of cold air and the northward displacement of warm air, resulting in the confrontation between cold and warm air over SEA. This cold-warm air confrontation, referred to as the "cold-warm TA dipole", is a primary characteristic of SEA extreme precipitation. We then apply EOF analysis to daily temperature advection over EA. Both observed and simulated results indicate that the EOF2 TA mode resembles the "cold-warm TA dipole" mode. This similarity implies that the EOF2 TA mode could serve as a possible predictor for intense precipitation over SEA. The TAI
83

obtained from the EOF2 TA mode can be an indicator for representing synoptic-scale extreme rainfall activities over YRB–SK–SP based on both observational data and CMIP6 models.

To gain a better understanding of the synoptic-scale processes that result in extreme rainfall over YRB–SK–SP, the study compares the TAI-all and TAI-extreme circulations. The TAI-all circulations (see **Figure 4.12**), responsible for day-to-day precipitation variations, show synoptic-scale waves in the upper troposphere. The upper-level trough (ridge) over Mongolia–Northern China (SC–SK–SP) displaces cold (warm) air southward (northward), resulting in a confrontation between cold and warm air in the lower troposphere. The southward displacement of cold air primarily causes intense rainfall over YRB (shown in the blue box in **Figure 4.11**), and northward-displaced warm air acts as a guiding airflow to transport moisture from EBOB to SK–SP, resulting in intense precipitation over SK–SP (shown in the pink box in **Figure 4.12**).

On the other hand, the TAI-extreme circulations help interpret the physical mechanism related to synoptic-scale extreme rainfall. The enhanced trough over Mongolia–Northern China in the upper-level extends across the entire Eurasian continent. More intense cold air from Northern China in the lower troposphere due to the enhanced upper-level trough leads to increased extreme precipitation over YRB. Moreover, the strengthened upper-troposphere trough enhances the southwesterly airflow along SK–SP, which contributes to moisture transport from low latitudes, leading to more intense extreme precipitation over SK–SP. The comparison between TAI-all and TAI-extreme circulations helps identify the specific atmospheric conditions and circulation patterns that cause extreme rainfall events in the region.

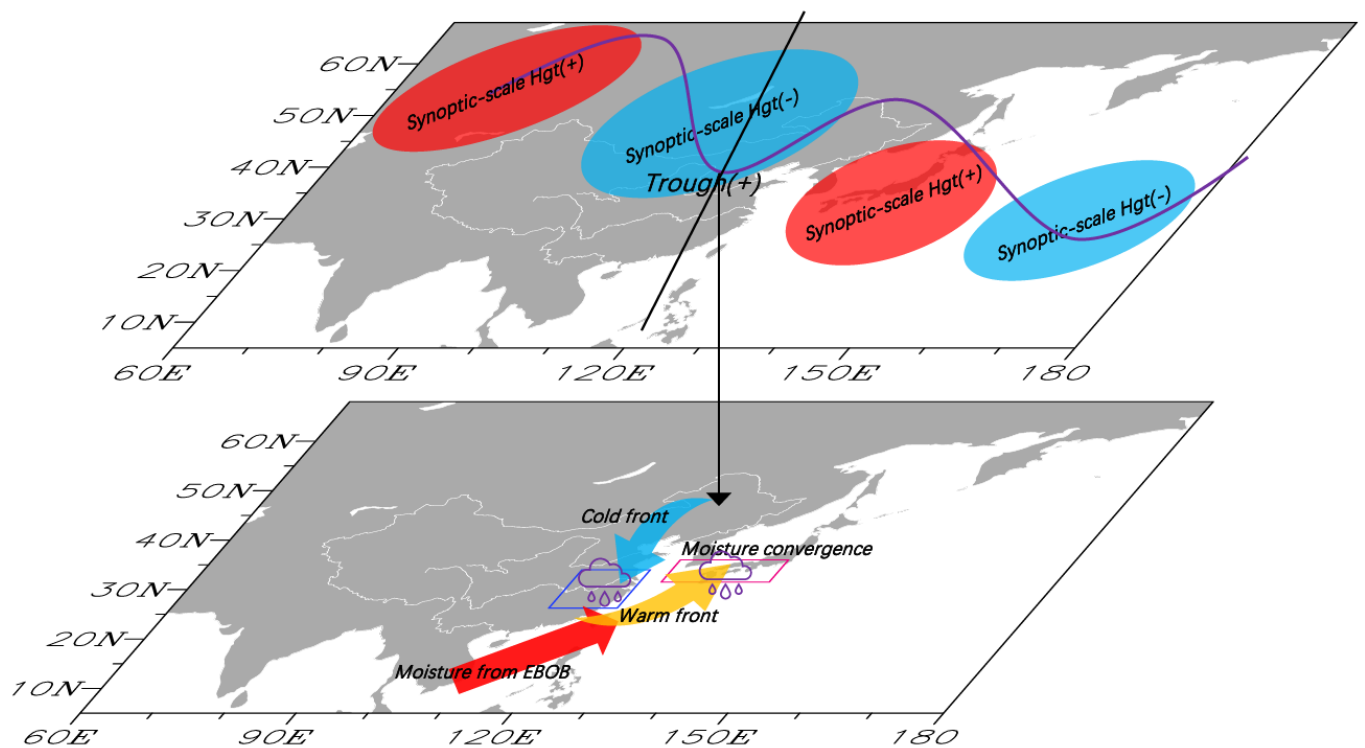


Figure 4.12 Schematic diagram illustrating the mechanisms leading to TAI-all precipitation changes over YRB–SK–SP. See text for details.

Table 4.1 The correlation coefficient between TAI and YRB-SK-SP daily rainfall for climatological sense (TAI-daily rainfall) and for extreme precipitation days (TAI-extreme daily rainfall). The results of observations and models are presented below.

Model	TAI-daily rainfall	TAI-extreme daily rainfall
ACCESS-CM2	0.4	0.16
BCC-ESM1	0.29	0.01
CanESM5	0.27	0.02
CESM2	0.37	-0.21
CESM2-FV2	0.33	-0.00
CESM2-WACCM	0.37	-0.14
EC-Earth3	0.34	-0.10
FGOALS-f3-L	0.22	-0.1
FGOALS-g3	0.31	0.06
GFDL-CM4	0.39	-0.02
INM-CM4-8	0.32	-0.01
INM-CM5-0	0.29	0.04
IPSL-CM6A-LR	0.23	0.03
MIROC6	0.36	-0.05
MPI-ESM-1-2-HAM	0.34	0.03
MPI-ESM1-2-HR	0.36	-0.00
MPI-ESM1-2-LR	0.32	0.13
MRI-ESM2-0	0.32	-0.05
NorESM2-LM	0.4	0.07
NorESM2-MM	0.32	-0.04
Observations	0.3	-0.12

Table 4.2 Z test for the extreme-day TAI and all-day TAI in observations and each individual model.

Model	Z value	P value
ACCESS-CM2	5.33	<<0.01
BCC-ESM1	8.64	<<0.01
CanESM5	6.31	<<0.01
CESM2	11.4	<<0.01
CESM2-FV2	11.95	<<0.01
CESM2-WACCM	10.36	<<0.01
EC-Earth3	8.25	<<0.01
FGOALS-f3-L	5.18	<<0.01
FGOALS-g3	10.2	<<0.01
GFDL-CM4	7.51	<<0.01
INM-CM4-8	8.36	<<0.01
INM-CM5-0	10.37	<<0.01
IPSL-CM6A-LR	5.00	<<0.01
MIROC6	12.76	<<0.01
MPI-ESM-1-2-HAM	11.76	<<0.01
MPI-ESM1-2-HR	10.08	<<0.01
MPI-ESM1-2-LR	9.01	<<0.01
MRI-ESM2-0	9.66	<<0.01
NorESM2-LM	12.67	<<0.01
NorESM2-MM	9.17	<<0.01
Observations	8.93	<<0.01

Table 4.3 The TAI-extreme ratio in observations and each CMIP6 model

Model	TAI-extreme ratio
ACCESS-CM2	0.62
BCC-ESM1	0.70
CanESM5	0.66
CESM2	0.75
CESM2-FV2	0.78
CESM2-WACCM	0.73
EC-Earth3	0.66
FGOALS-f3-L	0.59
FGOALS-g3	0.77
GFDL-CM4	0.68
INM-CM4-8	0.74
INM-CM5-0	0.75
IPSL-CM6A-LR	0.60
MIROC6	0.80
MPI-ESM-1-2-HAM	0.78
MPI-ESM1-2-HR	0.76
MPI-ESM1-2-LR	0.71
MRI-ESM2-0	0.74
NorESM2-LM	0.79
NorESM2-MM	0.69
MME	0.72
Observations	0.72

5 Evaluating the El Niño impacts on spring precipitation extremes over EA in CMIP6

In **Chapter 4**, we find that synoptic-scale spring precipitation extremes over EA are related to the cold-warm TA dipole mode. Using the TAI index, it can capture synoptic-scale variations related to extreme rainfall over YRB–SK–SP. Our analysis also demonstrates that CMIP6 models perform well in reproducing associated synoptic-scale circulations in this region. Building upon these results, we further examine the influence of EP and CP El Niño events on extreme rainfall in spring over EA and their performance in 14 selected models (as indicated in boldface in **Table 2.1**).

5.1 Spring EA precipitation extremes associated with EP and CP El Niño

In this chapter, we utilize EOF analysis to identify EP and CP El Niño events in both observations and models, instead of solely relying on the Niño3I and EMI indices. This approach is adopted because certain models fail to accurately capture SSTAs during El Niño (see **Figure 2.1**). By employing EOF analysis on SST fields, we can effectively depict variations in SST that are associated with both two types of El Niño. To assess the ability of 14 selected CMIP6 models to reproduce characteristics of EP and CP El Niño (see **Chapter 2**), we compared model-generated Pacific–Indian SSTAs with observations (**Figure 5.1a and 5.1b**) using composite analyses. **Figure 5.1c** shows the model-generated SSTA in the developing boreal winter during the peak of EP El Niño, and **Figure 5.1d** for CP El Niño events. Results show that the MME mean is able to represent El Niño and its diversity. For EP El Niño, SSTA characterized by positive/negative/positive signals over the equatorial central to eastern

Pacific/western Pacific/tropical Indian Ocean, is observed during the mature phase (boreal winter) in both observations and models. The observed and MME mean show that SST for CP El Niño exhibits a tri-pole pattern, featuring anomalous warming in the central Pacific and cooling in the eastern and western Pacific. **Figure A8** and **Figure A9** in the **Appendix** display the SSTAs corresponding to each model for EP and CP El Niño, respectively.

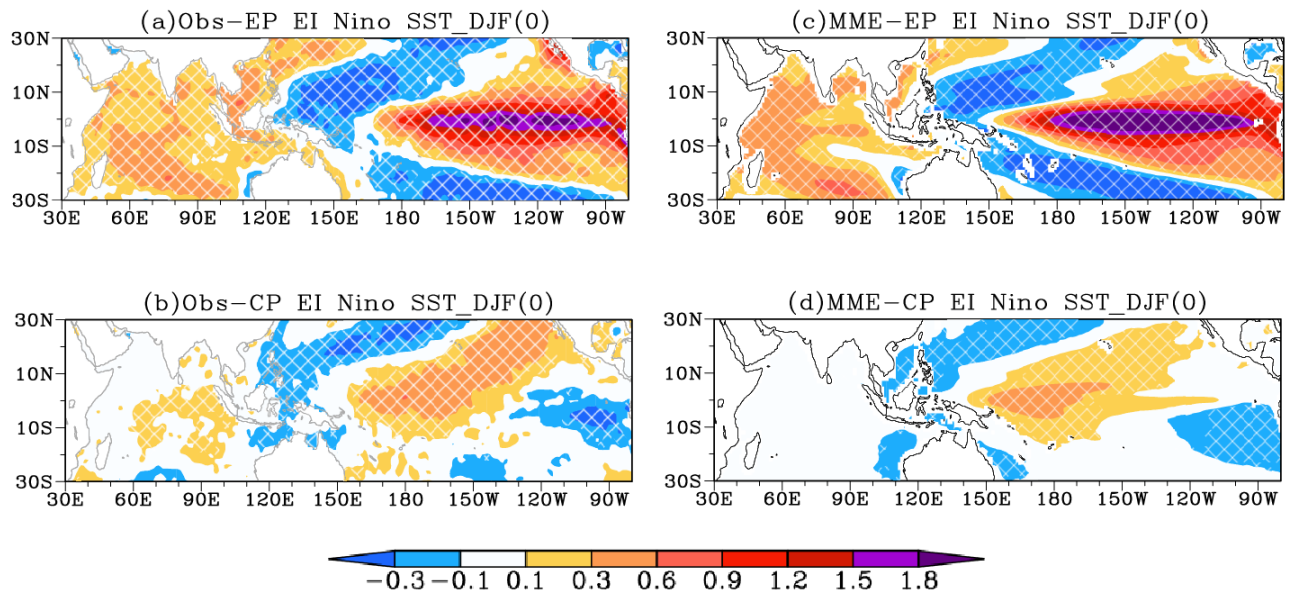


Figure 5.1 Composite SSTA (shading; units: $^{\circ}\text{C}$) during the DJF(0) for (a, c) EP and (b, d) CP El Niño events based on (a–b) observations and (c–d) CMIP6 MME mean of 14 models. The white crosses for observations denote SSTA that are statistically significant at the 95% confidence level, and the white crosses for models indicate more than 70% of models agree on the sign of SSTA between MME and each model.

We now examine the impact of EP and CP El Niño events on the decaying spring extremes over EA and assess the ability of 14 CMIP6 models to reproduce these observed impacts.

During EP El Niño events (**Figure 5.2a–d**), both observed (**Figure 5.2a, 5.2b, 5.2e, and 5.2f**) and simulated (**Figure 5.2c, 5.2d, 5.2g and 5.2h**) results show increased seasonal total precipitation (**Figure 5.2a, 5.2e, 5.2c and 5.2g**) and extreme precipitation (**Figure 5.2b, 5.2f, 5.2d and 5.2h**) over SEA. In contrast, observations show decreased seasonal total precipitation (**Figure 5.2e**) and extreme precipitation (**Figure 5.2f**) over SEA during CP El Niño events; while those features are poorly reproduced in the MME (**Figure 5.2g–h**). Overall, both observations and models show that the extremes account for a large proportion of seasonal total precipitation and that their spatial distributions are similar, indicating that extreme precipitation is a significant contributor to the seasonal total for the two types of El Niño.

Due to the varying ability of models to simulate EP and CP El Niño impacts, we will separately examine these two types of El Niño in the following study. Specifically, we will first investigate how the EP El Niño type modulates rainfall over SEA. We will then explore the reasons for the observed reduction in springtime extreme rainfall over SEA during CP El Niño and evaluate models' performance in capturing such phenomenon.

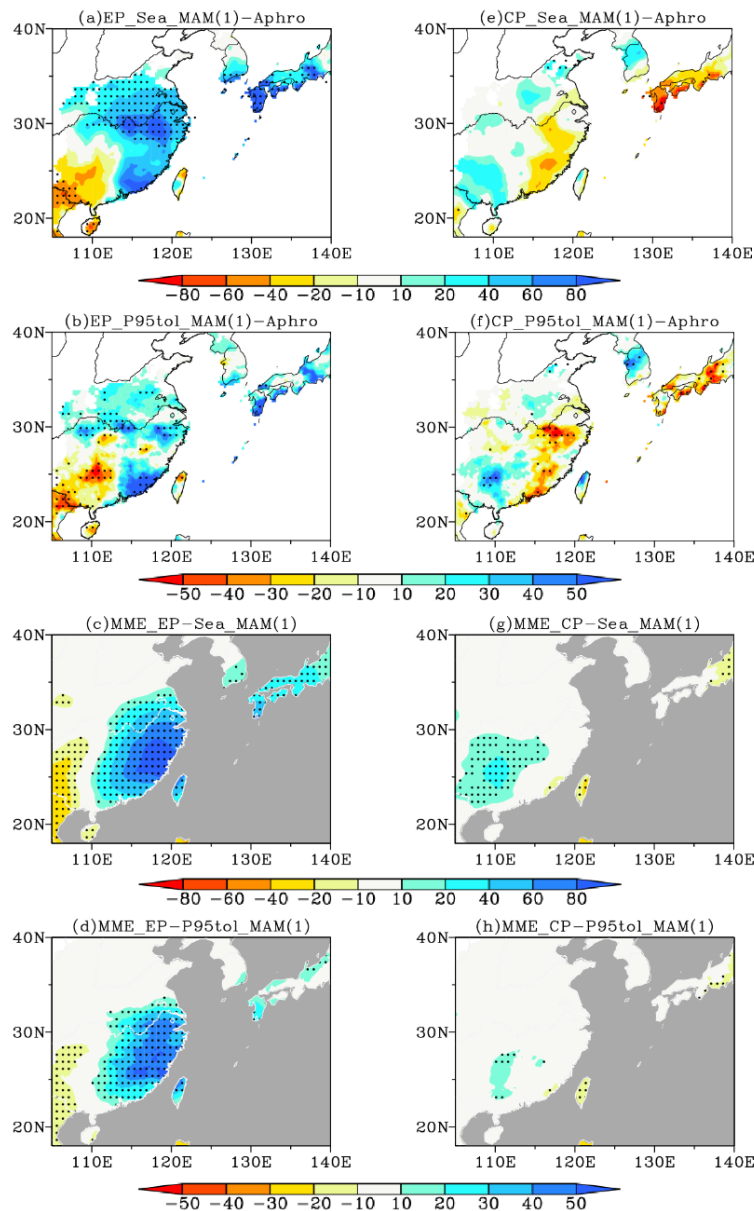


Figure 5.2 Precipitation anomalies during the following MAM season of the (a–d) EP and (e–h) CP El Niño events based on (a, b, e, f) APHRODITEv1101 and (c, d, g, h) MME mean of 14 selected models. (a, e, c, g) total accumulated seasonal precipitation (shading; units: mm season⁻¹), (b, f, d, h) total accumulated extreme precipitation (shading; units: mm season⁻¹). Black dots for (a–f) indicate the signals passing the 90% significance level. Black dots for (c–h) indicate locations over which more than 70% of models agree on the sign of precipitation anomalies between MME and each model.

5.2 Large-scale circulation during EP El Niño

To understand the influence of EP El Niño on spring extreme rainfall over SEA, we first analyzed the associated circulation anomalies. **Figure 5.3** gives the observed (**Figure 5.3a**) and simulated (**Figure 5.3b**) moisture flux and its divergence during EP El Niño events. Observations (**Figure 5.3a**) and MME mean (**Figure 5.3b**) reveal the presence of a low-level anticyclone feature in WNP. Such an anticyclone acts to transport warm and moist air from low latitudes to SEA, leading to above-average precipitation here. It is seen that both observations and the MME mean give the same feature present over WNP during EP El Niño, which provides favorable conditions for extreme precipitation over SEA.

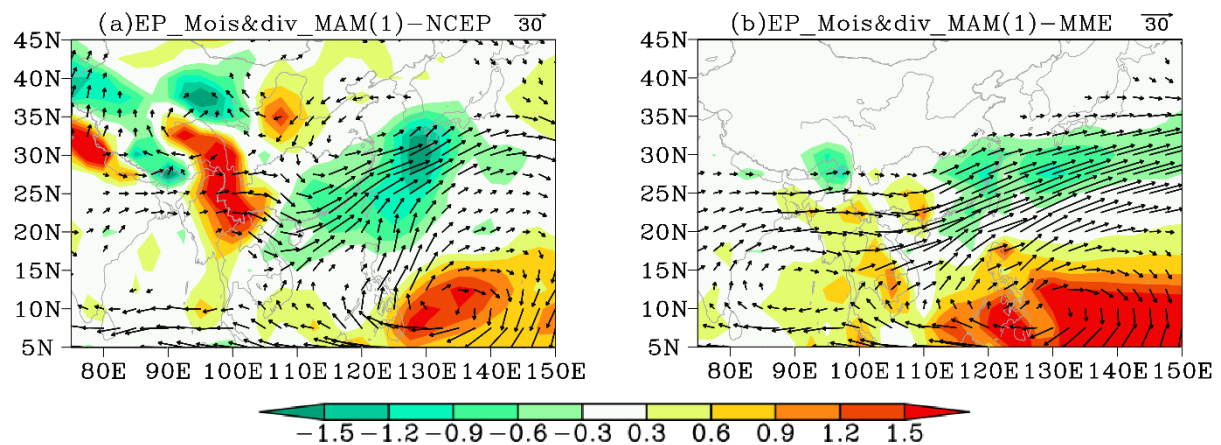


Figure 5.3 Anomalous vertically integrated moisture flux (vectors; units: $\text{kg m}^{-1} \text{s}^{-1}$) and its divergence (shading; units: mm day^{-1}) during the following MAM season of the EP El Niño events based on (a) NCEP and (b) MME mean of 14 selected models. Only moisture flux anomalies $> 5 \text{ kg m}^{-1} \text{s}^{-1}$ are shown.

SSTA in the equatorial region can drive local convection and diabatic heating, inducing upper-tropospheric circulation anomalies in remote areas through the propagation of Rossby waves to mid-high latitudes (Hoskins and Karoly 1981). To understand the extra-tropical Rossby wave dispersion during EP El Niño, the 250 hPa wave activity flux is analyzed. **Figure 5.4** shows the composite 250 hPa geopotential height anomalies and the associated wave activity flux during EP El Niño events, for observations (**Figure 5.4a**) and MME mean (**Figure 5.4b**). Regarding observations, wave activity flux can be observed throughout the entire northern Eurasian continent, extending to EA. This zonally oriented stationary wave pattern (SWP) is characterized by alternating positive and negative geopotential height anomalies along the East Asian westerly jet (EAJ) (**Figure 5.4a**). In contrast, in the MME mean, the SWP is absent during EP El Niño (**Figure 5.4b**). Thus, CMIP6 models exhibit poor performance in capturing the mid-high latitude SWP during EP El Niño events. Additionally, both observed and simulated results indicate that over the North Pacific–North America (PNA) region, the atmospheric circulation anomalies exhibit a wave train-like pattern, starting from the North Pacific with negative anomalies, propagating northeastward, and ultimately penetrating into the central-western part of North America with positive anomalies. However, in comparison to observations, the MME shows a stronger and equatorward-displaced PNA wave pattern.

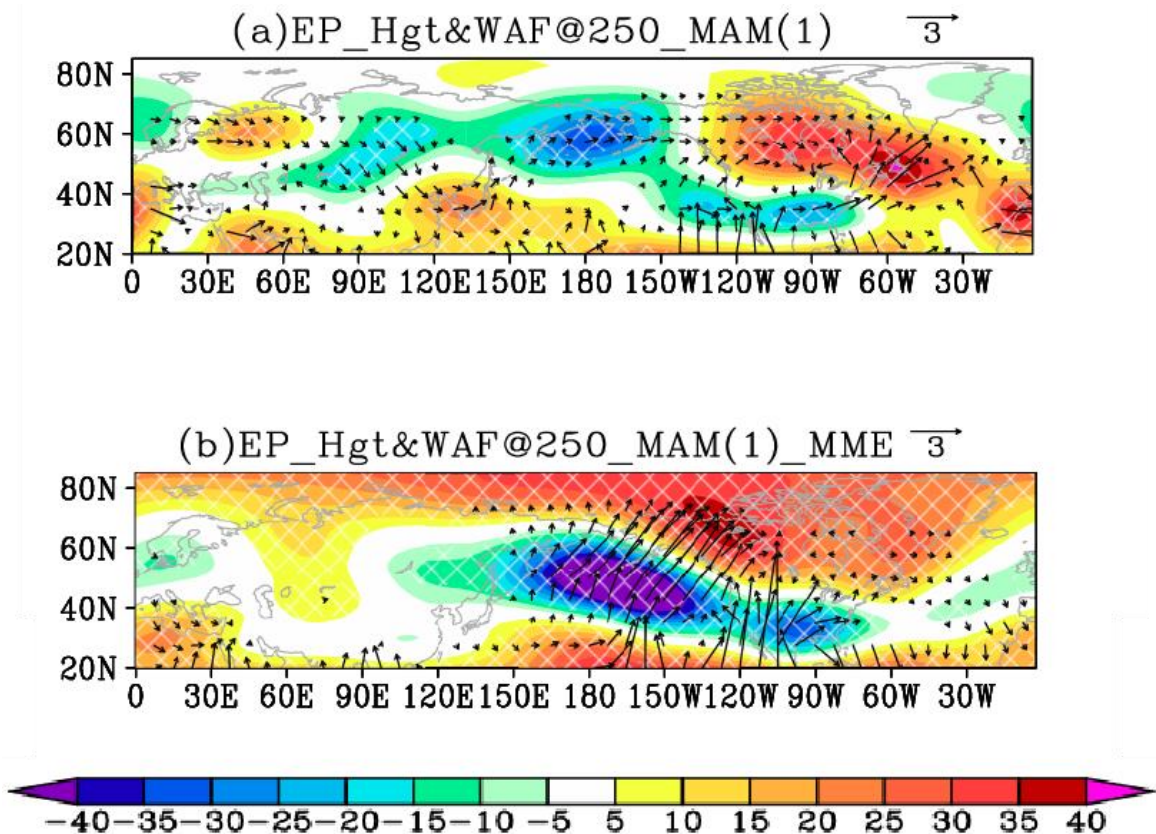


Figure 5.4 Same as Figure 5.3 but for 250 hPa wave activity flux (vectors; units: $\text{m}^2 \text{ s}^{-2}$) and 250 hPa geopotential height anomalies (shading; units: m). The vectors less than $0.2 \text{ m}^2 \text{ s}^{-2}$ are omitted. The white crosses in (a) indicate that geopotential height anomalies passing the 95% significance level. The white crosses in (b) indicate locations over which more than 70% of models agree on the sign of geopotential height anomalies between MME and each model.

Since the observed SWP teleconnection is trapped along the EAWJ (**Figure 5.4a**), EAWJ variations during EP El Niño are also investigated. From observations, enhanced EAWJ is found during EP El Niño (**Figure 5.5a**), consistent with previous studies (Horel, J.D. 1981; Wang 2002; Yang et al. 2002). However, note that the EAWJ anomaly cannot be reproduced

by the MME mean (**Figure 5.5b**). The poor performance of MME mean in simulating SWP teleconnection is likely due to the missing EAWJ anomalies during EP El Niño in models.

The possible reason for the poor performance of models in capturing EAWJ and SWP teleconnection is now considered. **Figure 5.6** presents the observed (**Figure 5.6a**) and simulated (**Figure 5.6b**) climatology of 250 hPa zonal winds, as well as the model biases (**Figure 5.6c**). The observed (**Figure 5.6a**) and simulated (**Figure 5.6b**) upper-level zonal winds show a strong wind belt across the EA in the axis of 20°N–40°N with a maximum wind speed larger than 35m s^{-1} . Although MME mean can generally capture upper-level background winds, biases of the 250 hPa zonal winds, characterized by a positive-negative-positive tri-pole pattern, still exist, our finding echoes those in previous studies about the model mean state as well (Ma et al. 2015; FU et al. 2020).

The poor simulation of EP El Niño-related EAWJ and SWP might be attributed to the bias of the mean-state zonal wind. For one thing, the underestimation of EAWJ background (see **Figure 5.6c**) has been demonstrated to reduce the SWP prediction skill (Li et al. 2021c). For another, the positive bias of the mean-state zonal wind in low latitudes (see **Figure 5.6c**) indicates an equatorward-displaced EAWJ background, which is likely to have a less impact on circulations in mid-high latitudes. Consequently, models fail to reproduce the EAWJ and SWP during EP El Niño. Furthermore, the enhanced and equatorward-displaced PNA wave train during EP El Niño in MME might be due to the simulated equatorward displacement of the mean-state EAWJ.

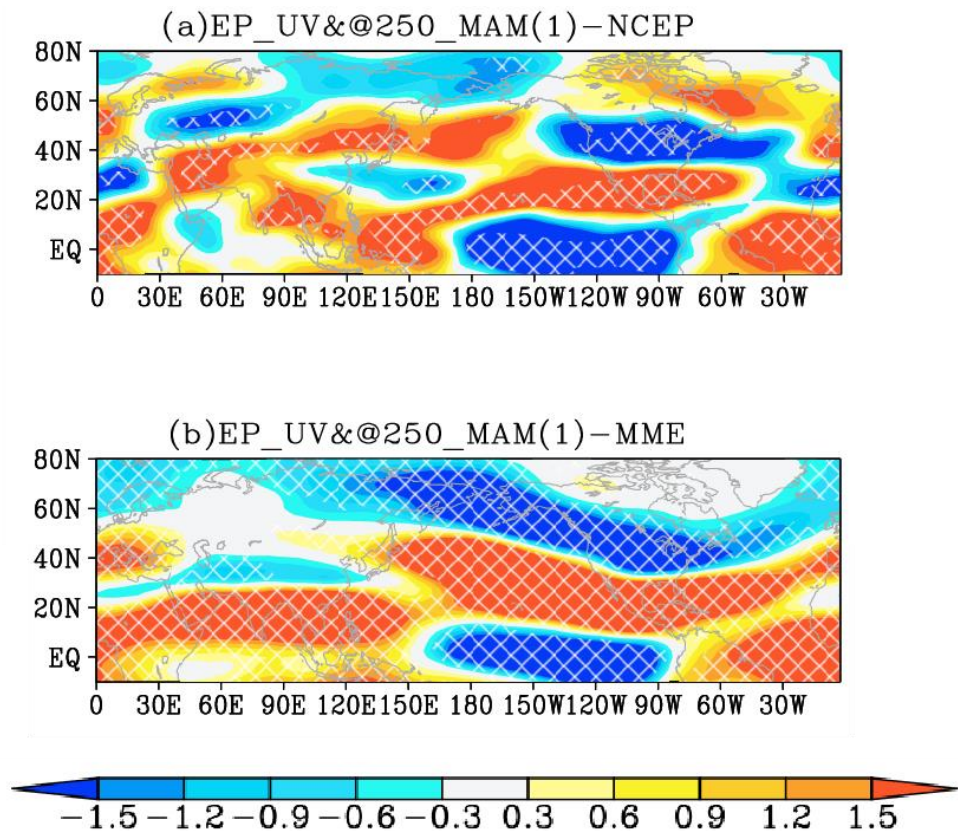


Figure 5.5 Same as Figure 5.3, but for 250 hPa zonal wind (shading; units: m s^{-1}). The white crosses in (a) indicate zonal wind anomalies passing the 95% significance level. The white crosses in (b) indicate locations over which more than 70% of models agree on the sign of zonal wind anomalies between MME and each model.

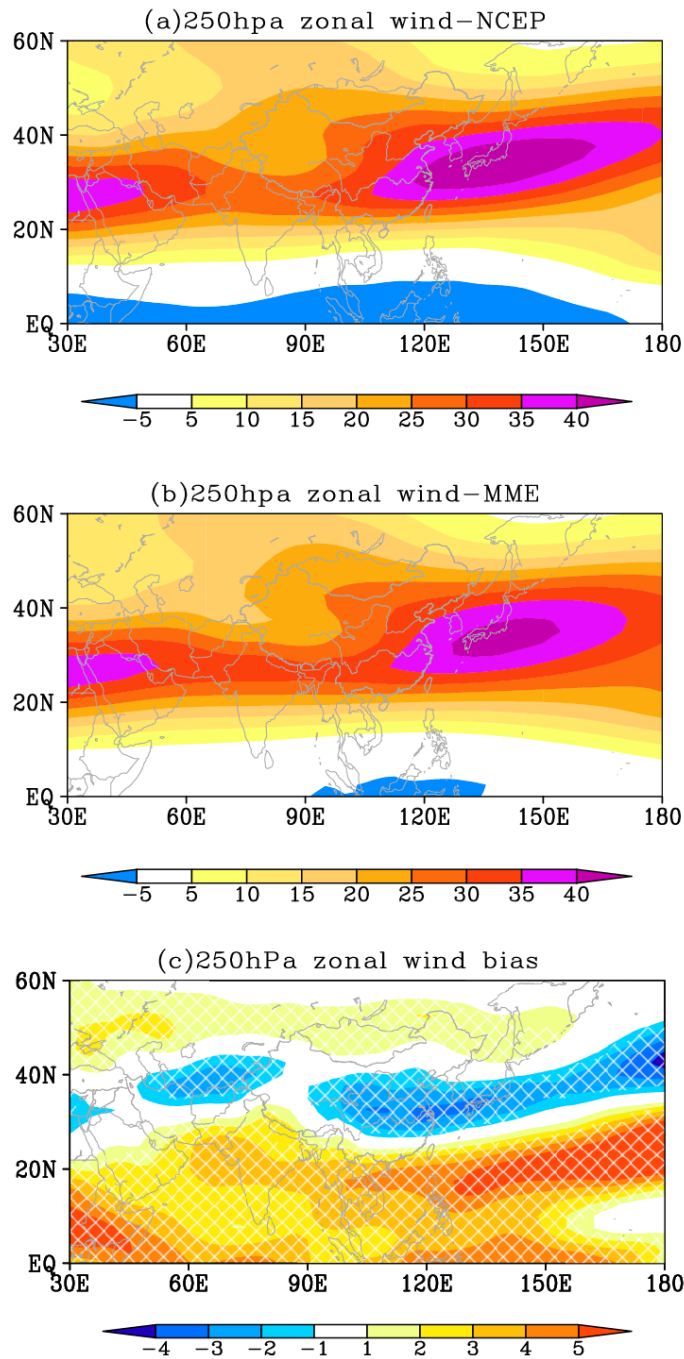


Figure 5.6 Climatology of 250 hPa zonal winds (shading; units: m s^{-1}) based on (a) NCEP reanalysis data and (b) MME mean of 14 models. (c) Climatological ensemble-mean 250 hPa zonal wind biases (shading; units: m s^{-1}) from the reanalysis climatology. White crosses in (b) indicate locations over which more than 70% of models agree on the sign of zonal wind between MME and each model.

A previous study has indicated that diabatic heating bias in models is a significant factor contributing to the bias observed in stationary waves (Park and Lee 2021). Here, we examine the anomalous vertically integrated (from surface to 300 hPa) atmospheric apparent heat source during EP El Niño based on observations (**Figure 5.7a**) and models (**Figure 5.7b**) (as described in detail by Hsu and Li, 2011). Observational results indicate that there are positive heat source anomalies observed in tropical eastern Pacific and tropical IO, while negative anomalies are found in tropical western Pacific. In the tropical region, heat source anomalies exhibit a similar pattern to SSTAs during EP El Niño events. This suggests that the SSTAs in the tropical region can directly trigger tropical diabatic heating anomalies. In addition, a distinct pattern of alternating positive and negative heat source anomalies can be observed in the extratropical region, originating from the North Atlantic and permeating across the northern Eurasian continent. This pattern bears similarities to upper-level SWP. Additionally, during EP El Niño, there is evidence of a PNA wave pattern-like pattern present in heat source anomalies. This finding suggests that EP El Niño not only impacts the climate in tropical regions but also plays a significant role in influencing circulations in the extratropical region. Thus, it is likely that the anomalous circulation patterns in the upper-troposphere in mid-high latitudes during EP El Niño (such as SWP and EAWJ) are driven by SSTAs in the tropical regions.

In contrast, MME mean overestimates heat source anomalies in tropical and PNA region. However, it fails to capture heat source anomalies that are associated with upper-level SWP. As a result, the models' poor performance in simulating the SRP and EAWJ during EP El Niño is not solely attributed to the background EAWJ bias, but is also influenced by the heating bias present during EP El Niño.

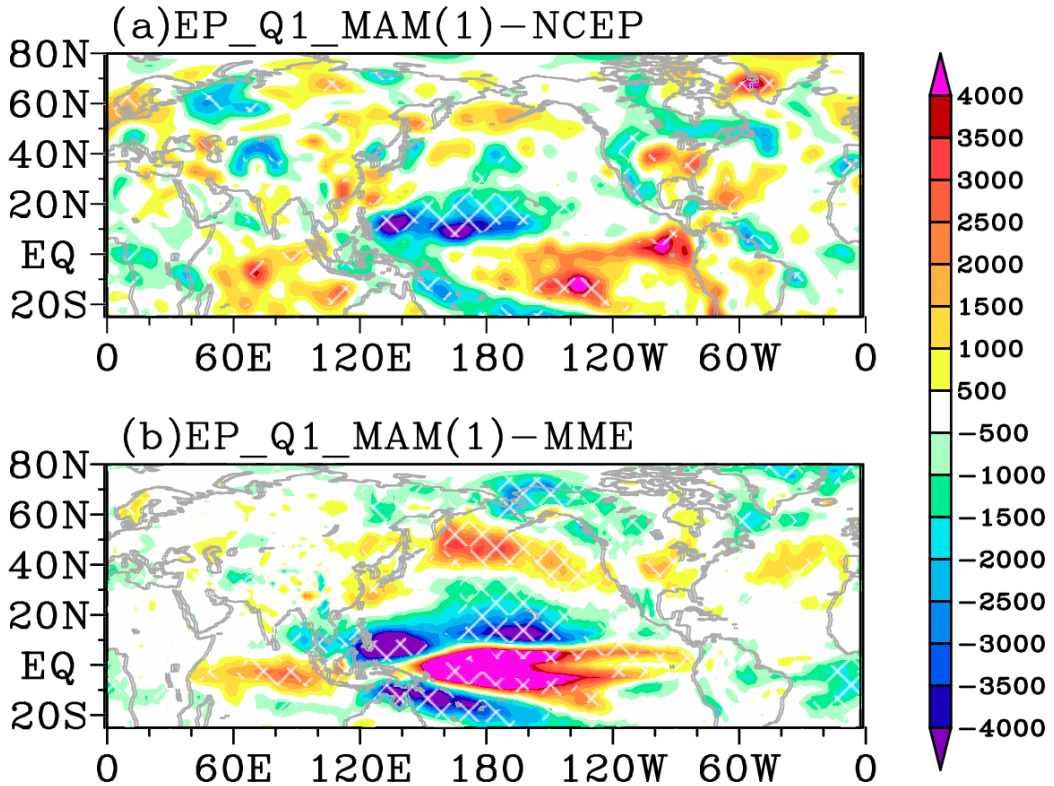


Figure 5.7 Same as Figure 5.3, but for vertically integrated atmospheric apparent heat source (shading; units: $\text{K kg m}^{-2} \text{ day}^{-1}$). The white crosses in (a) indicate heat source anomalies passing the 90% significance level. The white crosses in (b) indicate locations over which more than 70% of models agree on the sign of heat source anomalies between MME and each model.

5.3 Relationship between circulations related to EA extreme precipitation events and EP El Niño

Observations and models indicate that during EP El Niño, there are intense total precipitation extremes in SEA (as shown in **Figure 5.2b and 5.2d**), which is attributed to the presence of a seasonal mean lower-level anticyclonic anomaly over WNP (as depicted in **Figure 5.3**). As for day-to-day SEA extreme precipitation events, they are primarily attributed to moisture transported from EBOB (see **Figure 4.2**). Here, it is crucial to understand the connection

between seasonal mean circulation anomalies during EP El Niño and day-to-day circulation anomalies associated with SEA precipitation extremes.

We first investigate the SEA daily precipitation PDF distribution under the influence of EP El Niño based on observations. Considering the varying magnitudes of the increase in total extreme precipitation amounts among the SC, YRB, and SK–SP regions, separate studies are conducted on the daily precipitation PDFs for each of these regions. Results indicate that, when compared with climatology, the SC region exhibits a lower peak value in its daily precipitation PDF and a more right-skewed distribution during EP El Niño (**Figure 5.8a**). This suggests a decrease in light rainfall events and an increase in intense precipitation extreme events in the SC region. Note that the 95th percentile of daily precipitation in the SC region during EP El Niño is 1mm/day higher than that during all wet days (**Figure 5.8a**). This indicates that EP El Niño events are associated with a higher frequency of extreme precipitation events in the SC region. The YRB (**Figure 5.8b**) and SK–SP (**Figure 5.8c**) regions also exhibit a right-skewed PDF for daily precipitation under the influence of EP El Niño. However, the increase in 95th percentile of daily rainfall during EP El Niño is relatively smaller in the YRB region (0.43mm/day) and SK–SP region (0.48mm/day) compared to the SC region. This finding aligns with the total extreme precipitation anomalies illustrated in **Figure 5.2b**. The significant difference in the PDF of daily precipitation in SEA between the conditions of EP El Niño and climatology indicates that the seasonal mean circulations during EP El Niño have a profound impact on synoptic-scale circulation anomalies that are associated with SEA extreme precipitation events. Specifically, on the western side of lower-level anticyclonic circulation anomalies over WNP, the intensified southwesterly flows create favorable conditions for

moisture transport from EBOB to SEA on a synoptic scale.

We then examine the models' performance in simulating the impacts of EP El Niño on the PDF distribution of daily precipitation in SEA (**Figure A12**, **Figure A13** and **Figure A14**). The results suggest that the majority of the models can effectively capture the right-skewed PDF of daily precipitation in SEA during EP El Niño. Furthermore, the most models show that there is an increase in the 95th percentile of daily rainfall in SEA. Therefore, models are generally successful in replicating the observed connection between seasonal mean circulations during EP El Niño and synoptic-scale circulations related to SEA precipitation extremes. Only a few models exhibit poor ability to simulate the intensity of extreme precipitation changes during EP El Niño. For instance, while models from EC-Earth3 and CESM2 effectively replicate the right-skewed PDF of daily precipitation in SEA during EP El Niño, they fall short in capturing the heightened 95th percentile of daily rainfall in SEA during EP El Niño when compared to climatology.

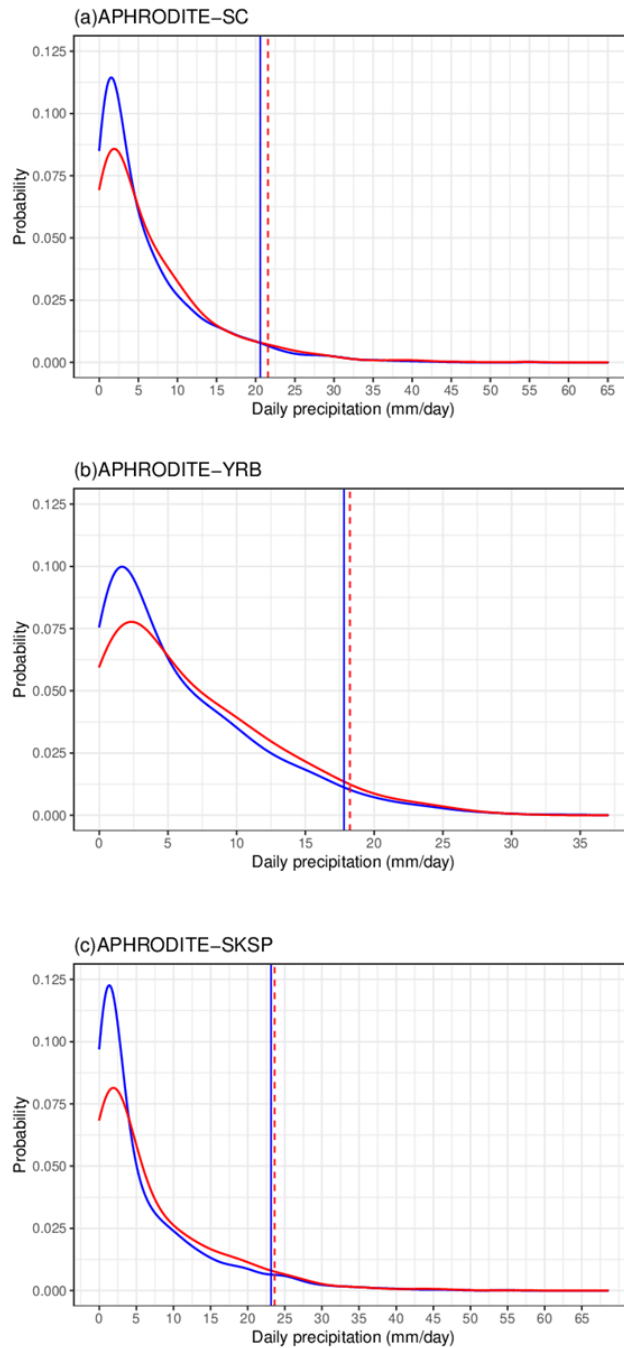


Figure 5.8 Daily precipitation probability density function (PDF) during EP El Niño (red curve) and all wet days (blue curve) events over (a) SC, (b) YRB and (c) SK-SP. The 95th percentile values of the daily precipitation associated with EP El Niño (climatology) are indicated by red (blue) vertical dashed (solid) lines in (a-c).

5.4 TAI-extreme precipitation over YRB-SK-SP during EP El Niño

The TAI-extreme precipitation over YRB-SK-SP has been elaborated in **Chapter 4**. Based on observations and CMIP6 models, all TAI-extreme ratios are about around 0.6 or more (**Table 4.3**), indicating that extreme events are closely related to the synoptic-scale circulation and related temperature advection over EA. In this Chapter, we investigate how EP El Niño might modulate a circulation background conducive to TAI-extremes.

We first examine the difference between all-day TAI and that the same but during EP El Niño only (EP-all-day TAI, hereafter). Observations show a significant positive TAI with a P value less than 0.05 using the Z test. It is found that two models namely CESM2-FV2 and MPI-ESM1-2-HR can differentiate such a difference (**Table 5.1**). This result suggests that EP El Niño is conducive to the occurrence of the EOF2 TA mode. However, most models show a poor ability to capture the TAI changes.

To further understand such impacts of EP El Niño on TAI-extremes, we compare the TAI-extreme ratio during EP El Niño (EP-TAI-extreme ratio, hereafter) with the TAI-extreme ratio computed using all years of data. **Table 5.2** presents EP-TAI-extreme, TAI-extreme ratios, using observations, the MME mean of 14 models, and also those from CESM2-FV2 and MPI-ESM1-2-HR. The observed EP-TAI-extreme ratio (0.85) is much larger than the TAI-extreme ratio (0.72), confirming that EP El Niño can provide a conducive environment to TAI-extremes over YRB-SK-SP. By contrast, no difference is found between EP-TAI-extreme and TAI-extreme ratios in MME mean, both being 0.72. On the other hand, a significant difference is found between EP-day TAI and all-day TAI in CESM2-FV2 and MPI-ESM1-2-HR, their EP-

TAI-extreme ratios are further inspected. There are only slight differences between EP-TAI-extreme and TAI-extreme ratios. Although CESM2-FV2 and MPI-ESM1-2-HR can capture significantly positive TAI during EP El Niño, they cannot reproduce changes in TAI-extreme precipitation during EP El Niño. In the following part, we focus on two issues: Firstly, based on observation, what favorable synoptic-scale circulations can EP El Niño provide for TAI-extremes? Another issue is why, in CMIP6 models, TAI-extremes during EP El Niño are not enhanced compared with climatology.

5.5 TAI-all circulations modulated by EP El Niño

We now study possible mechanisms leading to more TAI-extreme events during EP El Niño in observations, we compare TAI-all circulations during EP El Niño (EP-TAI-all circulations, hereafter) with TAI-all circulations. The aim is to understand what kinds of advantageously synoptic-scale conditions for TAI-extremes over YRB–SK–SP are provided by EP El Niño. In addition, by comparing the EP-TAI-all and TAI-all circulations in models, we interpret why CMIP6 models cannot reproduce more TAI-extremes occurring during EP El Niño.

To examine synoptic-scale circulation and its changes during EP El Niño, the TAI-all (**Figure 5.9a and 5.9d**), EP-TAI-all (**Figure 5.9b and 5.9e**) precipitation are first compared based on observations (**Figure 5.9a–b**) and MME (**Figure 5.9d–e**). From observations, although EP-TAI-all and TAI-all precipitation shares an identical pattern with positive anomalies over YRB–SK–SP, differences also exist between the former and the latter. To be specific, EP-TAI-all precipitation over YRB–SK–SP increases compared to that for TAI-all anomalies (**Figure 5.9c**), indicating that EP El Niño events can enhance precipitation over EA. Thus, a significant

increase is found in the TAI-extreme ratio during EP El Niño (**Table 5.2**). Note that nearly no precipitation change due to the synoptic-scale activities is found over SC because EP El Niño-related precipitation over SC is principally owing to interannual-scale anticyclonic anomaly over WNP but is less affected by mid-latitude disturbances. In contrast, although the MME mean can generally reproduce the EP-TAI-all and TAI-all precipitation pattern, their difference is insignificant. This is consistent with the result shown in **Table 5.2**, meaning that models fail to capture changes in TAI-extreme precipitation during EP El Niño.

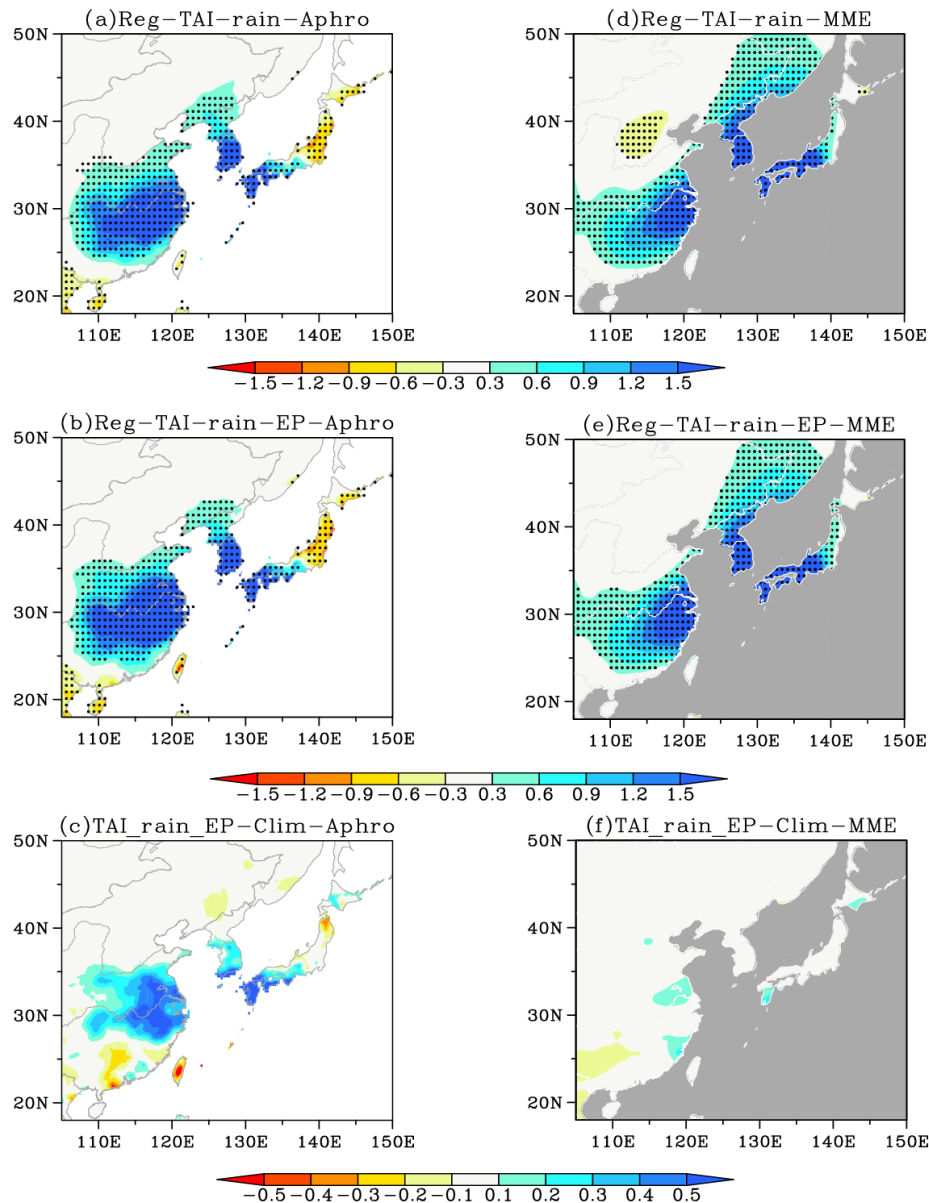


Figure 5.9 Anomalies of March–May daily precipitation (shading; units: mm day^{-1}) obtained by regressing onto (a, d) all-day TAI in MAM and (b, e) EP-all-day TAI, and (c, f) the difference between the latter and the former based on (a–c) NCEP data and (d–f) MME mean of 14 models. The black dots in (a–b) indicate precipitation anomalies passing the 95% significance level, and the black dots in (d–e) indicate locations over which more than 70% of models agree on the sign of anomalies of precipitation anomalies between MME and each of model.

Two issues will be addressed according to the difference between the EP-TAI-all and TAI-all precipitation over YRB–SK–SP. Based on observations, how EP El Niño enhances the synoptic-scale precipitation over YRB–SK–SP will be first investigated. Why MME mean fails to reproduce enhanced TAI-all precipitation over YRB–SK–SP during EP El Niño will be then inspected. **Figure 5.10** presents the TAI-all (**Figure 5.10a and 5.10d**) and EP-TAI-all (**Figure 5.10b and 5.10e**) 250 hPa geopotential height, as well as the difference between the latter and the former (**Figure 5.10c and 5.10f**), based on observations (**Figure 5.10a–c**) and MME mean (**Figure 5.10d–f**). As for TAI-all (**Figure 5.10a and 5.10d**) and the EP-TAI-all (**Figure 5.10b and 5.10e**) circulation anomalies, both observations (**Figure 5.10a and 5.10b**) and MME mean (**Figure 5.10d and 5.10e**) show the significant wave-like perturbations in the geopotential height. These upper-level disturbances, with the deep upper trough (ridge) over Mongolia–Northern China (SC–SK–SP), are linked to the lower-tropospheric southward (northward) displacement of cold (warm) advection. Based on observations, since the EP-TAI-extreme ratio is much larger than the TAI-extreme ratio (**Table 5.2**), It is proposed that EP El Niño might provide a suitable condition for TAI-extreme circulations. The differences between EP-TAI-all and TAI-all geopotential height at 250 hPa are further inspected to verify this hypothesis. The EP-TAI-all trough-ridge activity is found to be enhanced, featured with more negative (positive) anomalies over Lake Baikal–Mongolia–Northern China (Japan) (**Figure 5.10c**). Results from **Chapter 4** suggest that the deepened troughs and ridges in relation to the EOF2-TA mode can lead to more intense synoptic-scale extreme precipitation over YRB–SK–SP. Therefore, the more active synoptic-scale waves in the upper troposphere during EP El Niño might play a critical role in enhancing extreme precipitation over YRB–SK–SP. By contrast,

MME mean cannot reproduce the observed wave train and wave activity (**Figure 5.10f**), thus there is no significant difference between the EP-TAI-extreme and the TAI-extreme ratios.

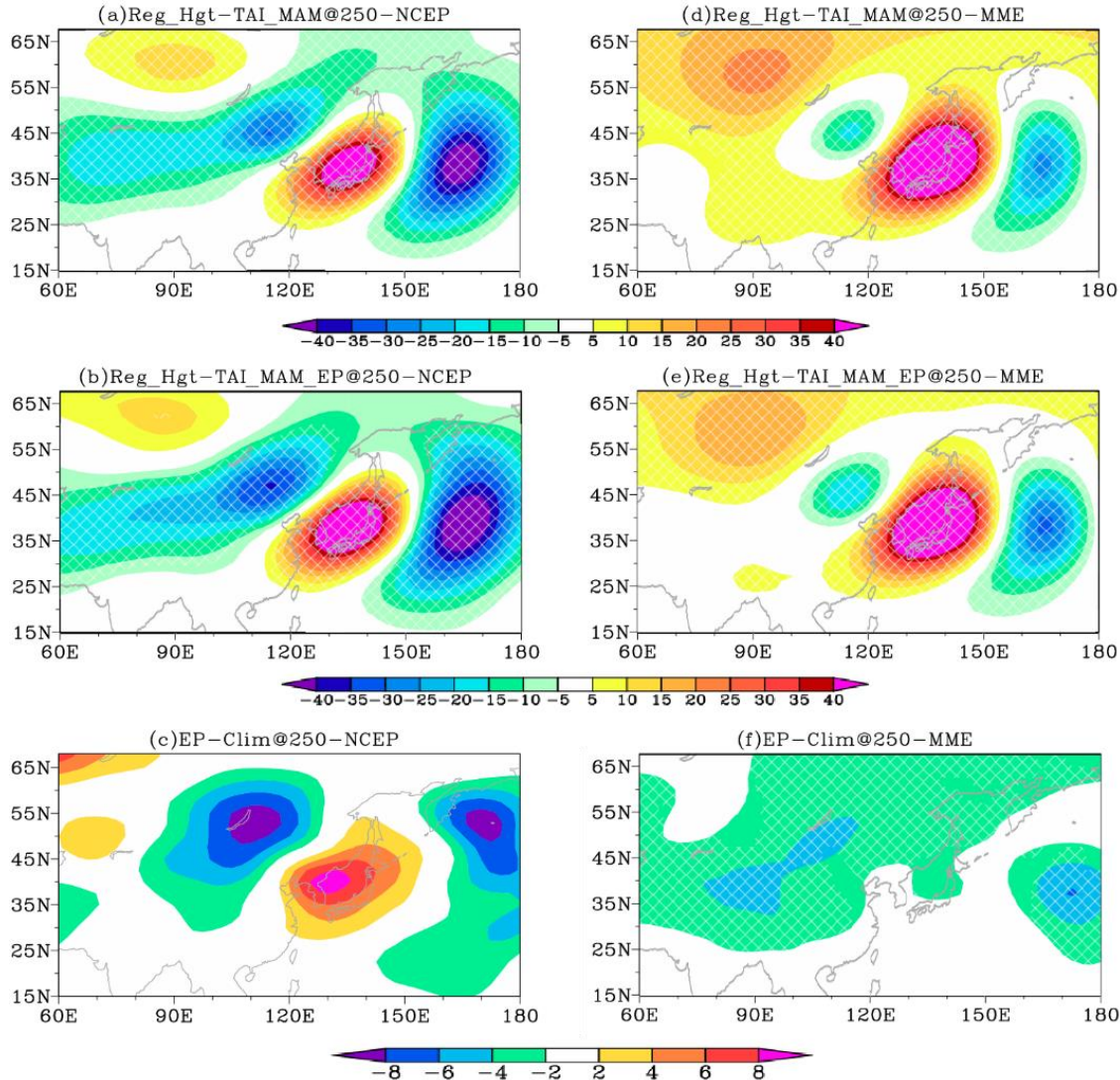


Figure 5.10 Same as Figure 5.9 but for 250 hPa geopotential height anomalies (shading; units: m). The white crosses in (a, b) indicate that geopotential height anomalies pass the 95% significance level. White crosses in (d–f) indicate locations over which more than 70% of models agree on the sign of geopotential height anomalies between the MME mean and each model.

We further investigate the synoptic-scale circulation anomalies in the lower troposphere during EP El Niño, with a focus on 850hPa temperature and winds. The observed (**Figure 5.11a–b**) and simulated (**Figure 5.11d–e**) results show that, comparing the EP-TAI-all (**Figure 5.11b and 5.11e**) with TAI-all (**Figure 5.11a and 5.11d**) 850 hPa temperature, both of them share the north-south oriented temperature dipole pattern, i.e. anomalous cooling (warming) over Mongolia–Northern China (SC–SK–SP). From observations, the difference between the EP-TAI-all and TAI-all temperature shows the negative (positive) anomalies over Mongolia–Northern China (SC–SK–SP), indicating a stronger meridional temperature gradient over EA during EP El Niño (**Figure 5.11c**). The enhanced atmospheric baroclinicity can cause stronger frontal activities from Northern China to YRB region, thus more intense extreme precipitation over YRB. In the upper level, the associated trough-ridge pattern is also strengthened accordingly during EP El Niño (**Figure 5.10c**); the enhanced trough over Mongolia–Northern China is conducive to the southward shift of cold air originating from Northern China, which is an essential contributor to intense precipitation extremes over YRB. In the MME mean, no significant changes are found in temperature perturbation and meridional temperature gradient during EP El Niño (**Figure 5.11f**), which echoes the previous result that models do not capture changes in YRB extremes.

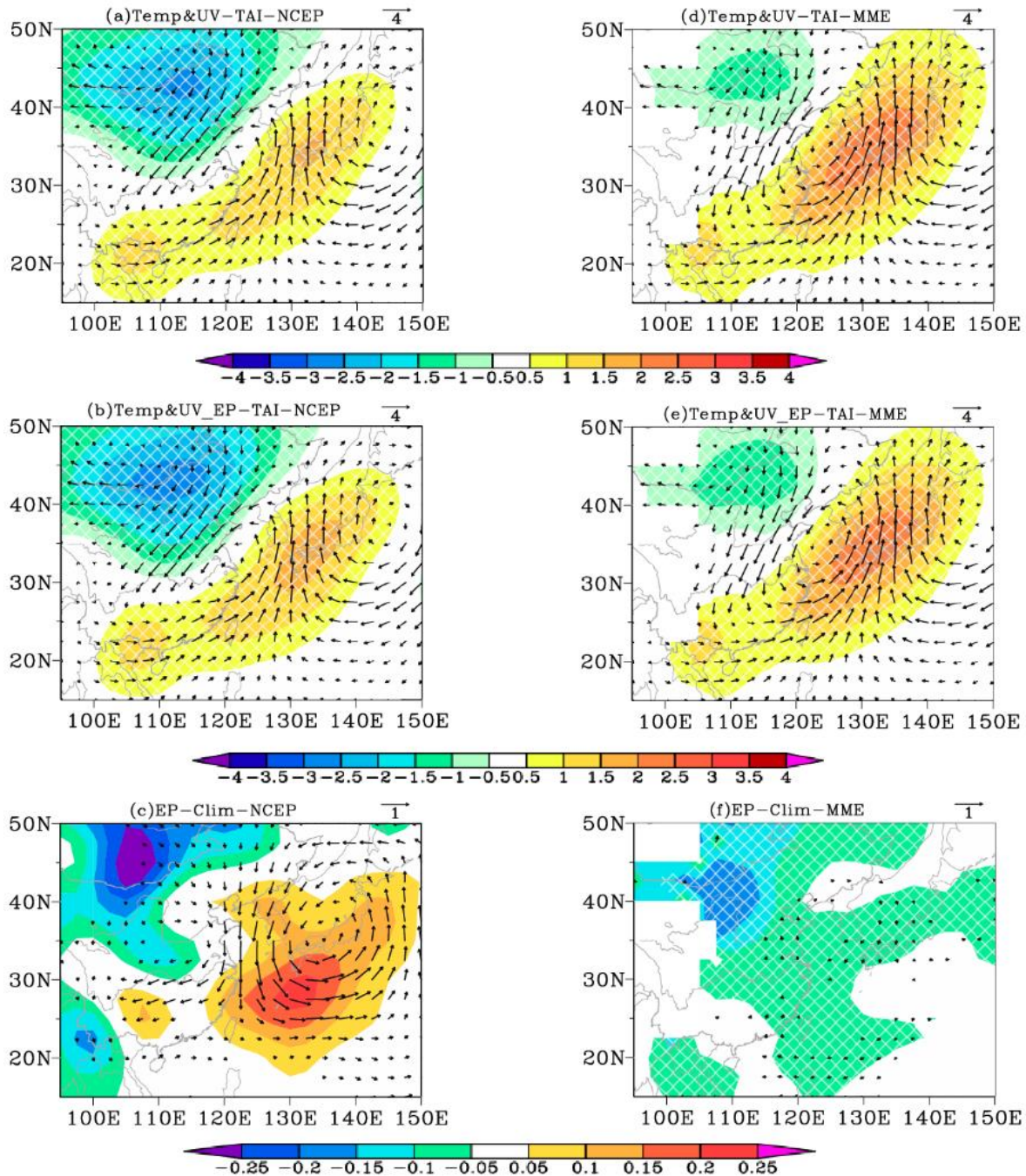


Figure 5.11 Same as Figure 5.9, but for 850 hPa temperature (shading; units: $^{\circ}\text{C}$) and 850 hPa wind (vectors; units: m s^{-1}). The white crosses in (a, b) indicate that 850 hPa temperature anomalies pass the 95% significance level, and white crosses in (d–f) indicate locations over which more than 70% of models agree on the sign of anomalies of 850 hPa temperature anomalies between MME and each of model.

Finally, moisture transport anomalies due to synoptic-scale circulation during EP El Niño are inspected. Results from observations (**Figure 5.12a–b**) and MME mean (**Figure 5.12d–e**) show that both EP-TAI-all (**Figure 5.12b and 5.12e**) and TAI-all (**Figure 5.12a and 5.12d**) are accompanied by southwest to northeast directed moisture flux along the SK–SP, contributing to moisture flux convergence over the area. In addition, the differences between EP-TAI-all and TAI-all moisture flux anomalies for observations (**Figure 5.12c**) and MME mean (**Figure 5.12f**) are explored as well. Observational data indicates that during the decaying spring of EP El Niño, there is an anomalous southwesterly airflow originating from the low-latitudes in WNP, which transports moisture from low latitudes to the SK–SP region, leading to convergence over that area (**Figure 5.12c**). The intensified ridge activity, associated with positive geopotential height anomalies over Japan in the upper troposphere (**Figure 5.10c**), plays an important role in generating the southwesterly airflow that serves as the moisture source for the SK–SP region. Therefore, synoptic-scale extreme precipitation over SK–SP is more frequent than normal during EP El Niño. In contrast, the MME mean fails to capture the upper-level synoptic-scale disturbances during EP El Niño. As a result, the moisture convergence over SK–SP is not captured by the MME mean, resulting in no changes in the TAI-related extreme precipitation ratios (**Figure 5.12f**).

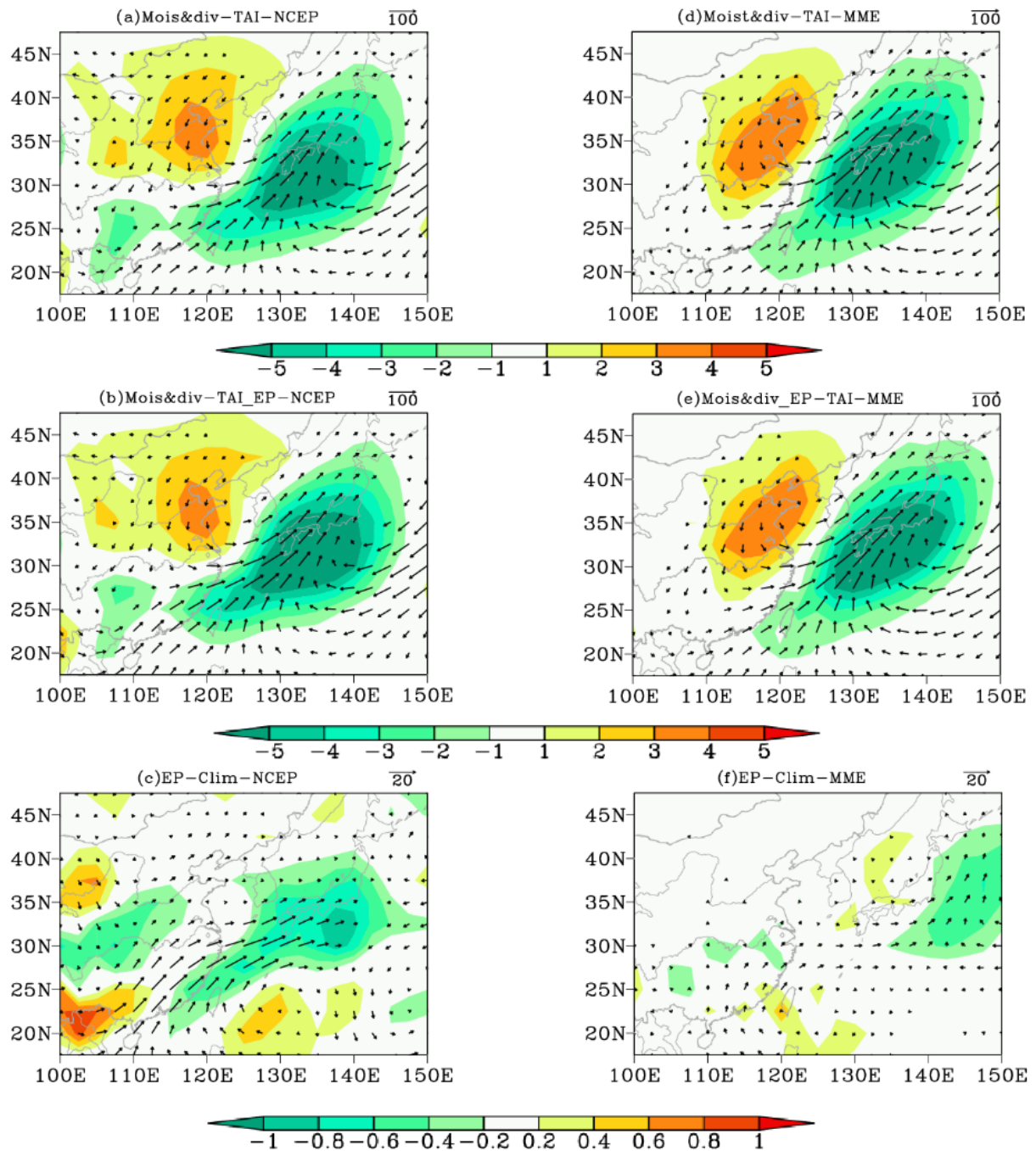


Figure 5.12 Same as Figure 5.9, but for vertically integrated moisture flux (vectors; units: $\text{kg m}^{-1} \text{s}^{-1}$) and its divergence (shading; units: mm day^{-1}). Only moisture flux anomalies greater than (a, b, d, e) $5 \text{ kg m}^{-1} \text{s}^{-1}$ and (c, f) $1 \text{ kg m}^{-1} \text{s}^{-1}$ are shown.

5.5 Mechanisms for springtime extreme precipitation during CP El Niño

We consider briefly potential mechanisms behind EA extreme precipitation changes during CP El Niño. In contrast to EP El Niño, the observed result shows suppressed seasonal mean (**Figure 5.2e**) and extreme precipitation (**Figure 5.2f**) over SEA during CP El Niño. However, CP El Niño-related precipitation pattern cannot be reproduced by the MME mean (**Figure 5.2g and 5.2h**). To investigate the reasons behind the reduced spring precipitation extremes during CP El Niño and the inadequate performance of CMIP6 models in simulating this phenomenon, we then analyze the moisture flux and its divergence during CP El Niño for both observational data (**Figure 5.13a**) and each model (**Figure A11**). Observations show the presence of moisture convergence associated with cyclonic low-level circulation near 150°N, as well as moisture divergence with northerly flow over SCS. Most models are able to simulate the wet condition near 150°N and the dry condition over SCS, but a few models, such as ACCESS-CM2 and FGOALS-g3, fail to reproduce this pattern. This finding is consistent with the research by Wang et al. (2019a). Additionally, unlike EP El Niño, the observed results reveal the existence of a lower-level anticyclonic anomaly situated west of the Philippines, extending from the WNP to EBOB (**Figure 5.13a**), which aligns with the findings of Yuan and Yang (2012). In Chapter 4, both observations and MME show that when extreme precipitation occurs over SEA, moisture mainly comes from the EBOB via strong anomalous southwesterly wind (**Figure 4.2**). This broad anomalous anticyclone over EBOB during CP El Niño could impede the moisture source from EBOB, which does not favor forming circulation related to that during extreme precipitation days over SEA. Some models, such as ACCESS-CM2, CESM2, FGOALS-g3, MPI-ESM1-2-HR, NorESM2-LM, and NorESM2-MM, are unable to reproduce the anomalous

anticyclone over EBOB. Other models, including CESM2-FV2, EC-Earth3, FGOALS-f3-L, GFDL-CM4, MIROC6, MPI-ESM-1-2-HAM, MPI-ESM1-2-LR, and MRI-ESM2-0, are capable of capturing this anticyclonic circulation spanning the EBOB region. In observations, the YRB region is primarily influenced by northerly winds originating from northeastern China. However, the models that successfully capture the lower-level anticyclonic circulation over EBOB mentioned above are unable to reproduce this characteristic. Thus, due to the deficiencies in the models' ability to simulate the circulation patterns during the decaying spring of CP El Niño, they are unable to reproduce the anomalous seasonal mean precipitation and extreme precipitation over EA. Regarding the MME mean, it successfully captures the pattern of moisture divergence in SCS and convergence east of 150°N. However, the MME mean fails to reproduce the anticyclonic circulation over EBOB and the northward airflow over YRB (**Figure 5.13b**). This deficiency results in insignificant changes in both the seasonal mean and extreme precipitation during the decaying spring of CP El Niño (**Figure 5.2g and 5.2h**). Hence, enhancing the models' capacity to simulate the large-scale circulation patterns associated with CP El Niño is crucial for improving their ability to replicate extreme precipitation over EA during the subsequent spring season.

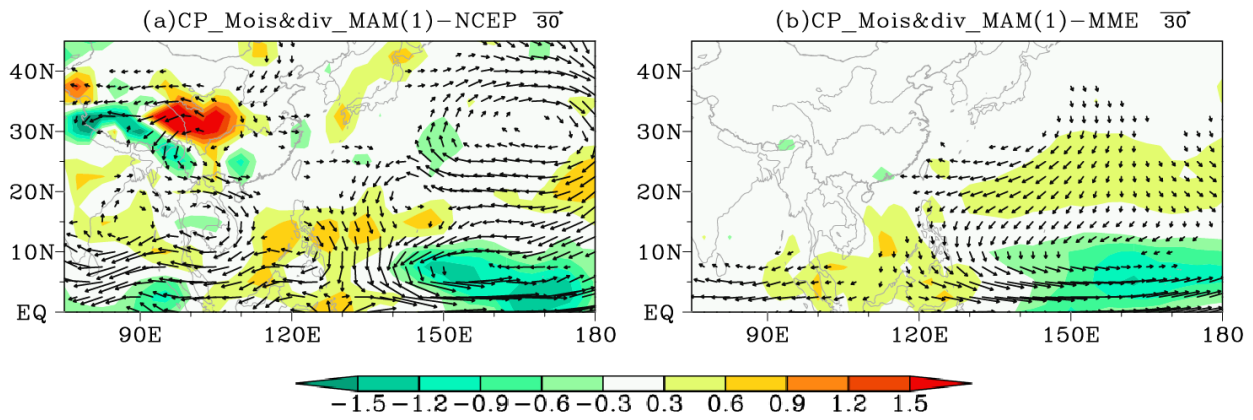


Figure 5.13 Same as Figure 5.3 but for CP El Niño. Only moisture flux anomalies $> 5 \text{ kg m}^{-1} \text{s}^{-1}$ are shown.

We further elucidate reasons behind the inability of models to replicate the anticyclonic anomaly over Indo-China during CP El Niño. Previous studies have indicated that models exhibiting a mean-state SST cold tongue bias often exhibit poor performance in reproducing the teleconnections associated with CP El Niño (Li et al. 2021b; Hou and Tang 2022). In our study, we observe a mean-state SST cold tongue bias in MME mean of CMIP6 models (see red box in **Figure 5.14**). This finding is consistent with previous studies that have also identified this bias (Wang et al. 2019a; Jiang et al. 2021). Meanwhile, based on observations, it has been observed that the tropical warming SST during CP El Niño is primarily located to the east of 150°E . However, across almost all models (**Figure A9**), there is a significant westward shift of positive SSTAs in the tropical region during CP El Niño, extending beyond 150°E . The SST bias during CP El Niño hampers the generation of an anticyclonic anomaly over the Indo-China region. Consequently, these models demonstrate a limited capability in capturing the drying signals in SC.

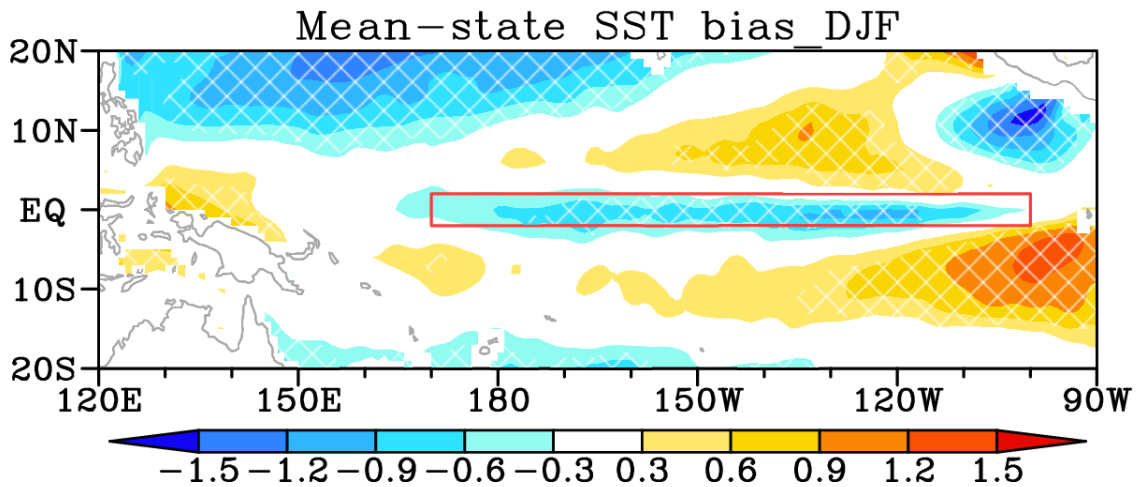


Figure 5.14 SST mean-state bias (shading; units: $^{\circ}\text{C}$) in the MME of 14 CMIP6 models. White crosses indicate locations over which more than 70% of models agree on the sign of SST bias between MME and each of model. The red box (170°E – 80°W ; 2°S – 2°N) denotes the mean-state SST cold tongue bias.

5.6 Summary

How to spring precipitation extremes over EA are affected by EP and CP El Niño is studied, using both observational data and simulations from 14 selected CMIP6 models. Both observations and the MME mean of 14 models show more (less)-than-normal total extreme precipitation over SEA during EP (CP) El Niño. The EP El Niño-related extreme rainfall is first investigated.

In terms of interannual-scale circulation variability during EP El Niño, both observations and MME show that an anticyclonic anomaly over WNP can be found, contributing to bringing

abundant moisture from the lower-latitude Pacific Ocean to SEA. This anticyclonic anomaly plays a critical role in enhancing the total extreme precipitation over SEA during EP El Niño. Due to models' outstanding performance in reproducing anticyclonic anomaly over WNP, MME mean exhibits a good ability to capture SEA total extreme precipitation anomalies during EP El Niño. Despite models being able to replicate the lower-level circulations during EP El Niño, they are unable to accurately reproduce the observed circulation anomalies in the upper troposphere. The observations demonstrate the confinement of SWP along the intensified EAWJ during EP El Niño. However, SWP and EAWJ anomalies during EP El Niño are absent from the MME mean due to the underestimated and equatorward-displaced EAWJ background.

This Chapter has demonstrated that precipitation extremes over YRB–SK–SP resulting from synoptic-scale activities are significantly increased during EP El Niño compared to the climatological conditions, but the MME mean fails to accurately replicate this change. In **Chapter 4**, it was demonstrated that synoptic-scale activities obtained from TAI dominate extreme precipitation events over YRB–SK–SP under climatological conditions. This Chapter investigates the changes in TAI-extreme ratios during EP El Niño based on observations and CMIP6 models. Observations reveal a 13% higher EP-TAI-extreme ratio compared to the TAI-extreme ratio, while both are almost equal in MME mean. Therefore, in this chapter, we also focus on how EP El Niño affects the relationship between extreme precipitation and synoptic-scale disturbances in observations and why models fail to capture such changes during EP El Niño.

In particular, we compare TAI-all and EP-TAI-all circulations to investigate the impacts of EP El Niño on extreme precipitation over YRB–SK–SP due to synoptic-scale activities. We also conduct the same analysis on 14 selected CMIP6 models to understand why these models show poor capacity in reproducing the changes in extreme precipitation due to synoptic disturbances during EP El Niño. The analysis of observations reveals that EP-TAI-all precipitation is significantly stronger than TAI-all precipitation over YRB–SK–SP during EP El Niño, indicating the influence of synoptic-scale activities. In contrast, MME mean fails to replicate such a change during EP El Niño.

We then investigate how EP El Niño triggers more-than-normal extreme precipitation due to synoptic-scale activities over YRB–SK–SP in observations. Firstly, the TAI-all and EP-TAI-all upper-troposphere circulations are examined, with a focus on 250 hPa geopotential height. Observations show strengthened upper-level waves characterized by a deepened trough over Mongolia–Northern China and an enhanced ridge over SK–SP during EP El Niño, whereas there is no enhanced upper-level trough-ridge activity during EP El Niño in MME mean. The results suggest that EP El Niño amplifies the upper-level synoptic-scale waves, possibly due to enhanced upper-level westerlies and increased atmospheric baroclinicity along the EAWJ providing favorable conditions for synoptic-scale waves. In contrast, the MME mean fails to capture the observed trough-ridge anomalies due to its poor performance in simulating the EP El Niño-related circulation anomalies in the mid-high latitudes. Specifically, according to the MME mean, the absence of SWP and positive EGR anomalies along the EAWJ during EP El Niño weakens its ability to capture synoptic-scale disturbances associated with precipitation

extremes. Therefore, the increased atmospheric baroclinicity effect plays an essential role in enhancing the upper-level waves during EP El Niño.

In observations, the enhanced synoptic-scale waves can enlarge the meridional temperature gradient over EA in the lower troposphere. Specifically, by comparing the EP-TAI-all and TAI-all temperatures and winds at 850 hPa, an enhanced southward shift of cold air is found, which is attributed to the deepened upper-level trough over Mongolia–Northern China. The cold air from Northern China spills south into YRB, resulting in more-than-normal precipitation over YRB. By contrast, the MME mean cannot reproduce the upper-level waves during EP El Niño, and the cold air in the lower troposphere cannot be captured as well. Therefore, the extreme precipitation observed over YRB caused by synoptic disturbances cannot be reflected in the MME mean.

Apart from that, we also compared the EP-TAI-all and TAI-all moisture transport. In observations, the intensified southerly airflow resulting from the strengthened upper-level ridge over Japan facilitates the moisture transport from WNP to the SK–SP region through southwesterly winds. This increased moisture transport contributes to enhanced precipitation over SK–SP, primarily driven by synoptic-scale disturbances during EP El Niño. In comparison, the MME mean cannot capture the observed moisture convergence over SK–SP, resulting in the extreme precipitation over SK–SP related to synoptic-scale activities being less affected by EP El Niño.

In observations, the intensified atmospheric baroclinicity during EP El Niño acts to enhance synoptic-scale activities related to extreme precipitation. However, the model's inability to

capture the upper-level westerlies during EP El Niño hinders its ability to accurately replicate the extreme precipitation events associated with synoptic-scale disturbances. Here, we investigate the influence of the upper-level westerlies during EP El Niño on synoptic-scale activities associated with extreme precipitation by examining the EGR anomalies at 500hPa in observations (**Figure 5.15a**) and MME (**Figure 5.15b**). Positive anomalies of EGR are observed along the EAWJ extending to the EA-Pacific region in the observations (**Figure 5.15a**), indicating stronger atmospheric baroclinicity and resulting in more synoptic-scale activities occurring in this broad area. Therefore, a higher probability of extreme precipitation events related to synoptic-scale disturbances can be observed during EP El Niño compared to climatological conditions. However, in the MME, the anomalies in EGR cannot be captured due to the deficient simulation of the upper-level westerlies under EP El Niño caused by the mean-state EAWJ bias (**Figure 5.15b**). This deficiency results in the inability to reproduce the enhanced atmospheric baroclinicity, which in turn prevents the replication of synoptic-scale activities associated with extreme precipitation.

The mechanism by which EP El Niño causes TAI-extremes in decaying boreal spring, as observed, is illustrated in **Figure 5.16**. During EP El Niño, the intensified upper-level westerlies lead to increased atmospheric baroclinicity, resulting in more synoptic-scale disturbances related to precipitation extremes over YRB–SK–SP. In upper level, the synoptic-scale waves show amplified trough-ridge activity, while the lower troposphere exhibits an enlarged meridional temperature gradient over EA. Specifically, in the rear of the deepened upper trough over Mongolia–Northern China, the southward displacement of cold air in the lower troposphere contributes to intense extreme rainfall over YRB. Additionally, the much

stronger upper-level trough-ridge activity is also conducive to the northward-displaced warm air, leading to moisture transport from WNP to SK-SP and resulting in intense extreme precipitation over SK-SP. However, the MME mean fails to replicate the EP El Niño-related westerlies due to the bias of the background flow, impeding the synoptic-scale chain reactions.

In contrast to EP El Niño, the observational data indicates that extreme precipitation over SEA is lower than normal during CP El Niño. This could be attributed to the westward extension of the anticyclonic anomaly to the EBOB, which hinders moisture transportation from the EBOB and subsequently results in less extreme precipitation over SEA. However, the MME mean fails to accurately simulate the changes in seasonal mean, as well as extreme precipitation over SEA during CP El Niño. This is primarily attributed to the deficiencies in the models' capability to reproduce the anomalous circulation patterns during CP El Niño. When compared to observations, certain models are unable to capture the anticyclonic anomaly over EBOB. Although some models successfully simulate the anticyclonic circulation over EBOB, they often misrepresent the anomalous northerly airflow over YRB as southerly airflow. Consequently, investigating impacts of CP El Niño on EA climate during the subsequent spring season remains a challenge for CMIP6 models.

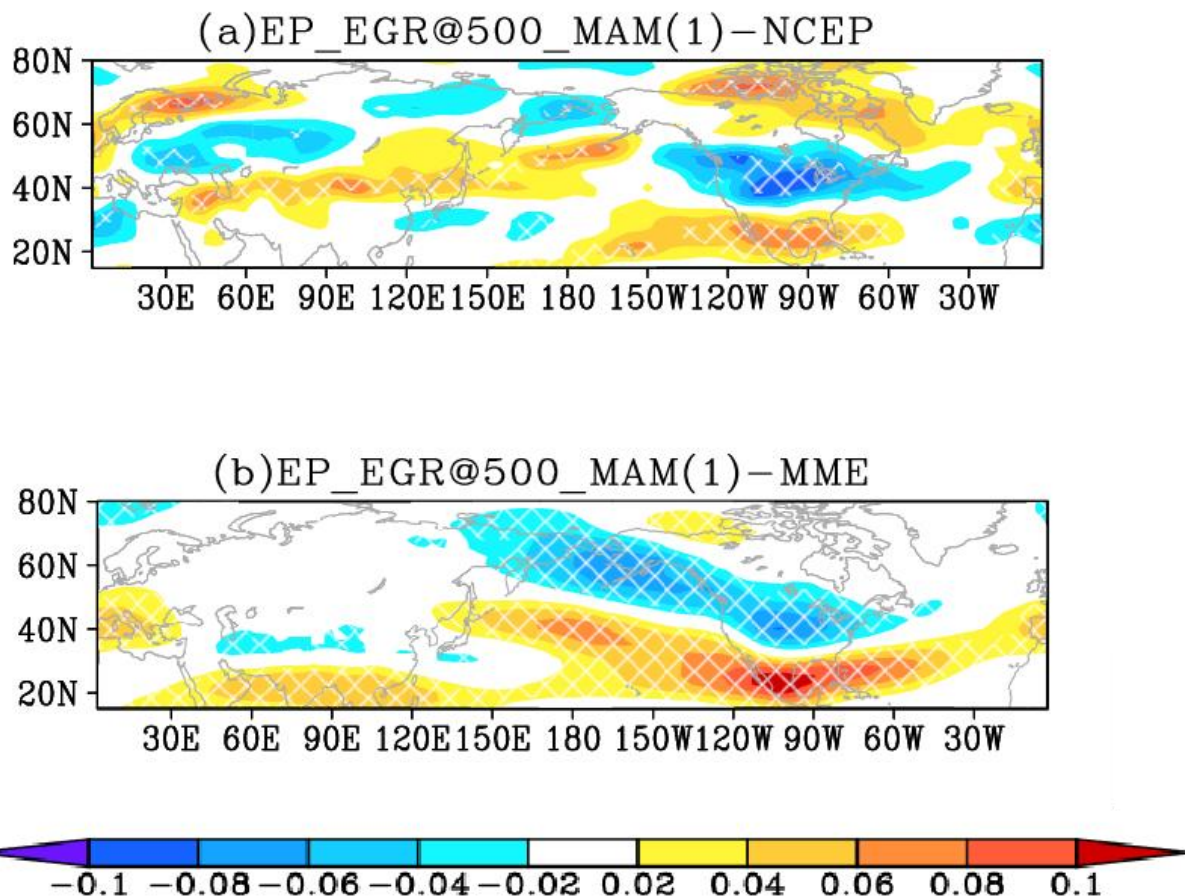


Figure 5.15 Same as Figure 5.3, but for 500 hPa EGR (shading; units: day^{-1}).

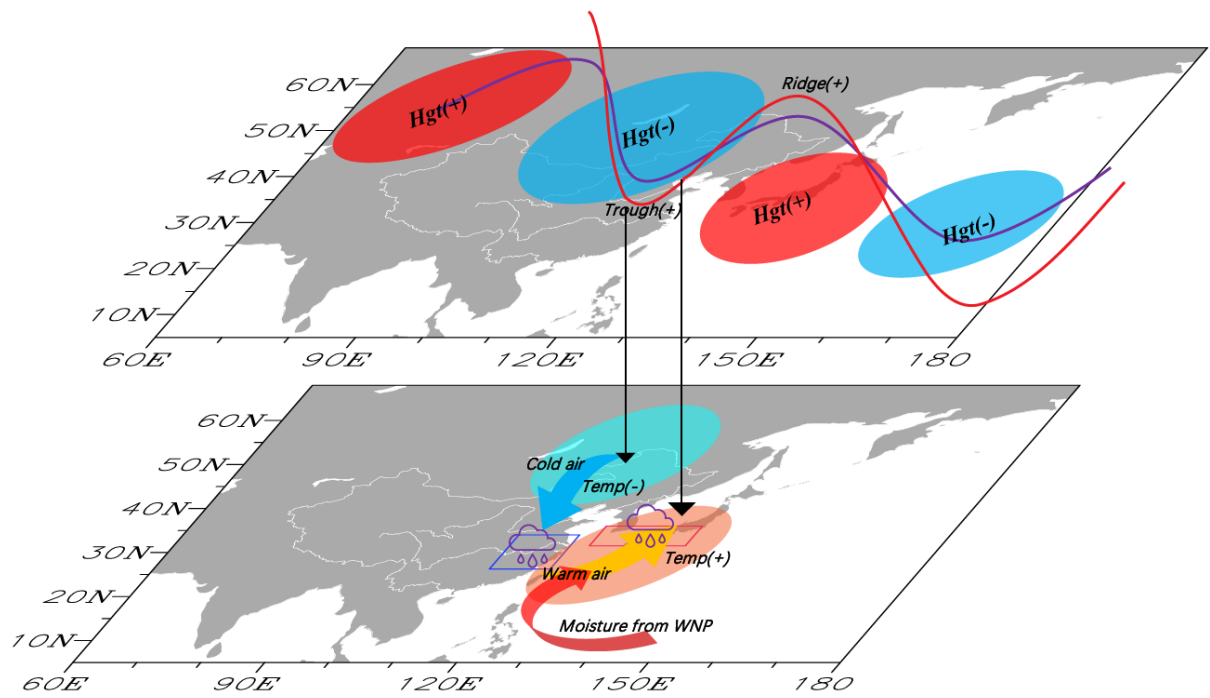


Figure 5.16 Schematic diagram illustrating the mechanisms leading to EP-TAI-all precipitation changes over YRB–SK–SP. See text for details.

Table 5.1 Z test for EP-all-day TAI and all-day TAI based on observations and 14 selected CMIP6 models. The models marked by red font indicate the corresponding P value less than 0.05.

Model	Z value	P value
ACCESS-CM2	-0.11	0.91
CESM2	1.42	0.16
CESM2-FV2	2.05	0.04
EC-Earth3	-0.58	0.56
FGOALS-f3-L	0.70	0.48
FGOALS-g3	-0.24	0.81
GFDL-CM4	-0.80	0.42
MIROC6	1.32	0.19
MPI-ESM-1-2-HAM	0.55	0.58
MPI-ESM1-2-HR	2.15	0.03
MPI-ESM1-2-LR	0.62	0.53
MRI-ESM2-0	1.11	0.27
NorESM2-LM	0.20	0.84
NorESM2-MM	1.03	0.30
Observations	2.25	0.02

Table 5.2 The EP-TAI-extreme ratio and TAI-extreme ratio based on observations, two CMIP6 models with P value less than 0.05 obtained by Z test for TAI during the days of the EP El Niño and climatology, and MME mean of 14 selected models.

Model	TAI-extreme ratio	TAI-extreme ratio for EP El Niño
CESM2-FV2	0.78	0.79
MPI-ESM1-2-HR	0.76	0.78
MME	0.72	0.72
Observations	0.72	0.85

6 Conclusion and Discussion

The overarching contribution of this thesis is to provide a new perspective to understand how different types of El Niño modulate the occurrence risk of extreme precipitation over EA. Here springtime and summertime extreme precipitation are separately investigated. Using observational data, we first investigated the statistical circulation anomalies related to summertime extreme precipitation over EA from 1951 to 2007 and interpreted what kinds of large-scale backgrounds of EA extreme rainfall in summer are provided by two types of El Niño in their decaying phases. Using observational data and CMIP6 models, we then explored the synoptic activities associated with springtime extreme rainfall over EA and illustrated how El Niño affects those synoptic-scale circulation systems. This thesis responded to three basic issues proposed in **Chapter 1**. Here we discuss and draw conclusions based on new findings in this thesis, highlighting the main novel contributions to the field.

6.1 Summer extreme precipitation modulated by two types of El Niño

Many studies investigated the circulation anomalies during EP and CP El Niño in decaying summer. However, the mechanisms by which extreme precipitation is modulated is not clear. In **Chapter 3**, using observational data, the probability of summertime extreme precipitation over SYR (MBC) for EP and CP El Niño are compared, clarifying the effect of interannual-scale circulations related to two types of El Niño on extreme precipitation over SYR (MBC). During EP (CP) El Niño, the southward (northward) displacement of WPSH and WJ triggers the circulations associated with precipitation extremes over SYR (MBC). In particular, when EP El Niño occurs, the WJ tends to be displaced southward in relation to the positioning of

WPSH, contributing to stronger vertically integrated moisture flux convergence over SYR and hence a higher probability of intense extreme precipitation there, while at the same time, there is moisture flux divergence over MBC. During CP El Niño, the convergence (divergence) over MBC (SYR) is related to local Hadley circulation anomalies, causing a higher (lower) probability of intense extreme precipitation in situ. The different flow patterns associated with El Niño diversity appear to be forced by different SST warming signals in either tropical IO or MC regions, which can induce anomalous regional atmospheric circulation that affects the behaviors of WPSH and WJ. EP (CP) El Niño is generally conducive to extreme precipitation over SYR (MBC) in decaying summer.

6.2 The modulation of EP El Niño on the relationship between spring extreme precipitation and synoptic-scale disturbances

Previous studies have investigated the modulation effect of El Niño on large-scale extreme precipitation; however, there is a paucity of research specifically exploring how El Niño modulates extreme precipitation. In **Chapter 4** and **Chapter 5** of this study, we aim to fill this research gap and provide a comprehensive analysis of this field.

Observations reveal that the EOF2 of daily temperature advection at 850 hPa exhibits a cold-warm dipole, which closely resembles the circulation pattern observed during extreme precipitation events over YRB–SK–SP. We then designate the normalized principal component of the EOF2 TA mode, which serves as an indicator of synoptic-scale variability, as the TAI. In climatology sense, precipitation over YRB–SK–SP is proved to be affected by synoptic-scale disturbances associated with TAI-all circulations. The upper-level trough-ridge activities

extending from Mongolia to Japan, driven by synoptic-scale waves, are associated with the southward (northward) displacement of cold (warm) air originating from Northern China (WNP). This atmospheric mechanism leads to the occurrence of intense precipitation over YRB–SK–SP.

Subsequent investigation reveals that the probability of precipitation extremes over YRB–SK–SP, linked to synoptic-scale disturbances, experiences a noteworthy increase during EP El Niño episodes compared to climatological conditions. The intensified upper-level westerlies during EP El Niño plays a crucial role in augmenting atmospheric baroclinicity along EAWJ, resulting in enhanced synoptic-scale disturbances that promote precipitation extremes over YRB–SK–SP. Stronger synoptic-scale waves in the upper troposphere indicate a more pronounced trough-ridge activity during EP El Niño. Moreover, an enlarged meridional temperature gradient over EA is observed in the lower troposphere. The intensified upper trough over Mongolia–Northern China contributes to the southward displacement of cold air originating from Northern China, leading to increased precipitation over YRB. Simultaneously, strengthened moisture transport from the WNP to SK–SP is associated with an intensified upper ridge, resulting in enhanced rainfall over SK–SP. Overall, EP El Niño creates a favorable environment for intense precipitation extremes over YRB–SK–SP, facilitated by synoptic-scale disturbances. The corresponding mechanism is depicted in the flow chart provided in **Figure 6.1**. This study not only introduces a novel day-to-day predictor for extreme spring rainfall over EA but also offers a fresh perspective for examining the interplay between interannual-scale circulations during EP El Niño and synoptic-scale activities.

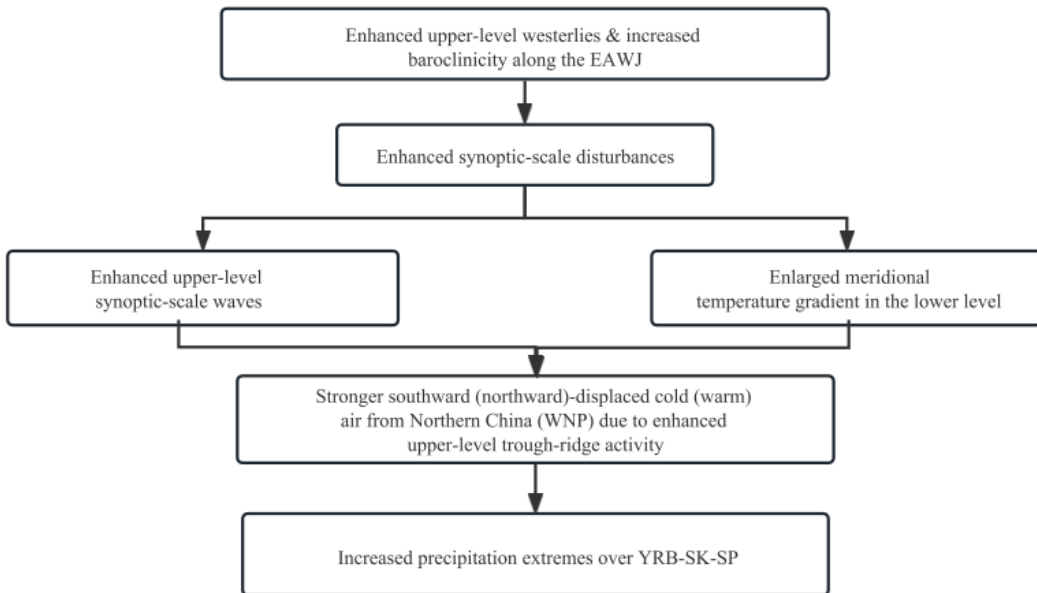


Figure 6.1 Flow chart illustrating the mechanisms underlying the occurrence of intense synoptic-scale-related precipitation extremes over YRB–SK–SP during EP El Niño.

6.3 Assessing CMIP6's capability to reproduce extreme spring precipitation over EA and the impacts of EP El Niño

Previous studies have evaluated the performance of CMIP5/CMIP6 models in simulating extreme precipitation, but there has been limited focus on their specific modeling capability in capturing extreme precipitation events attributed to synoptic-scale activities. This study emphasizes the evaluation of whether CMIP6 models can accurately reproduce extreme precipitation resulting from synoptic-scale disturbances, as well as their ability to simulate the modulation of extreme precipitation by EP El Niño.

CMIP6 models demonstrate a robust capability in simulating extreme precipitation over YRB–SK–SP associated with synoptic-scale disturbances, characterized by upper-level synoptic-

scale waves and a pronounced meridional temperature gradient over EA in the lower troposphere. However, these models exhibit poor performance in simulating anomalous precipitation extremes over YRB–SK–SP associated with synoptic-scale disturbances during EP El Niño. The underlying reasons are outlined as follows (refer to **Figure 6.2**): CMIP6 models inadequately capture the EP El Niño-induced westerlies due to biases in the mean-state EAWJ, resulting in reduced atmospheric baroclinicity. Consequently, diminished synoptic-scale activities associated with precipitation extremes over EA are observed. Improving the ability to simulate the background flow is identified as a critical factor for obtaining reasonable synoptic-scale activities during EP El Niño.

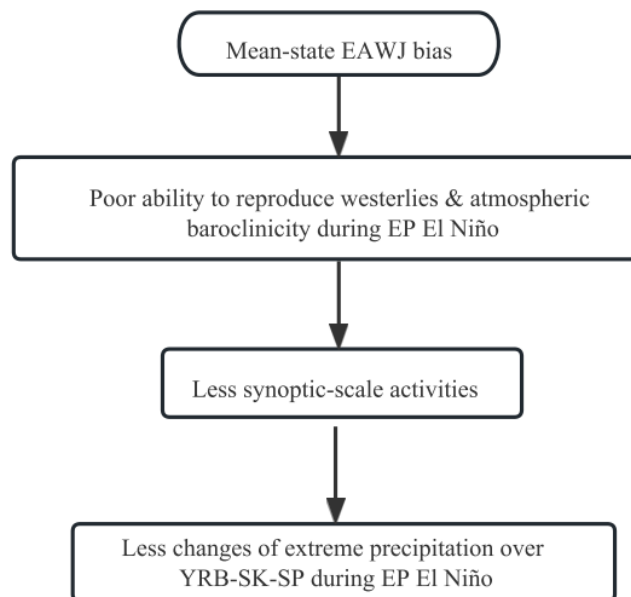


Figure 6.2 Flow chart illustrating the reasons behind the inability of CMIP6 models to accurately reproduce extreme precipitation over YRB–SK–SP during EP El Niño, attributed to synoptic-scale activities.

6.4 Future work

In our study, we have examined the mechanisms that contribute to extreme precipitation events in observed data and assessed the impacts of El Niño on extreme precipitation. Additionally, we have evaluated the ability of CMIP6 models to simulate these identified mechanisms. However, our research did not directly investigate extreme precipitation under future global warming scenarios. There are two potential avenues for further exploration that can be considered as an extension of this study:

- (1) How do springtime and summertime precipitation extremes over EA and their associated large-scale circulations (i.e., ENSO) change under the influence of global warming, compared to historical simulations?
- (2) Is there an increased/reduced/unchanged relationship between synoptic-scale disturbances and springtime and summertime extreme precipitation over EA under the influence of global warming, compared to historical simulations?

Appendix

A1 Details for extreme rainfall indices

In **Chapter 2**, we mentioned that there are diverse methods of obtaining extreme precipitation event. The methods of calculating each extreme rainfall index are show as follows. (See details at <https://climate-scenarios.canada.ca/?page=climdex-indices>)

1) $Rx1day$

RR_{ij} represents the daily precipitation amount on day i in period j . The maximum 1-day value for period j are:

$$Rx1day_j = \max (RR_{ij}) \quad (\text{A1.1})$$

2) $Rx5day$

RR_{kj} represents the precipitation amount for the 5-day interval ending k , period j . Then maximum 5-day values for period j are:

$$Rx5day_j = \max (RR_{kj}) \quad (\text{A1.2})$$

3) $R10mm$

RR_{ij} represents the daily precipitation amount on day i in period j . Count the number of days where:

$$RR_{ij} \geq 10mm \quad (\text{A1.3})$$

4) $R20mm$

RR_{ij} represents the daily precipitation amount on day i in period j . Count the number of days

where:

$$RR_{ij} \geq 20mm \quad (\text{A1.4})$$

5) CWD

RR_{ij} represents the daily precipitation amount on day i in period j . Count the largest number of consecutive days where:

$$RR_{ij} \geq 1mm \quad (\text{A1.5})$$

6) $PRCPTOT$

RR_{ij} represents the daily precipitation amount on day i in period j . If ' I ' represents the number of days in j , then

$$PRCPTOT_j = \sum_{i=1}^I RR_{ij} \quad (\text{A1.6})$$

7) $R95pTOT$

RR_{wj} represents the daily precipitation amount on a wet day ' w ' ($RR \geq 1mm$) in period j and $RR_{wn}95$ is the 95th percentile of precipitation on wet days in the whole period.

If ' W ' represents the number of wet days in the period, then:

$$R95p_j = \sum_{w=1}^W RR_{wj} \text{ where } RR_{wj} > RR_{wn}95 \quad (\text{A1.7})$$

8) $R99pTOT$

RR_{wj} represents the daily precipitation amount on a wet day ' w ' ($RR \geq 1mm$) in period j and $RR_{wn}99$ is the 99th percentile of precipitation on wet days in the whole period.

If ' W ' represents the number of wet days in the period, then:

$$R99p_j = \sum_{w=1}^W RR_{wj} \text{ where } RR_{wj} > RR_{wn}99 \quad (\text{A1.8})$$

9) SDII

RR_{wj} is the daily precipitation amount on wet days ' w ' ($RR \geq 1mm$) in period j . If ' W ' represents number of wet days in j , then:

$$SDII_j = \frac{\sum_{w=1}^W RR_{wj}}{W} \quad (\text{A1.9})$$

A2 Supplemental figures

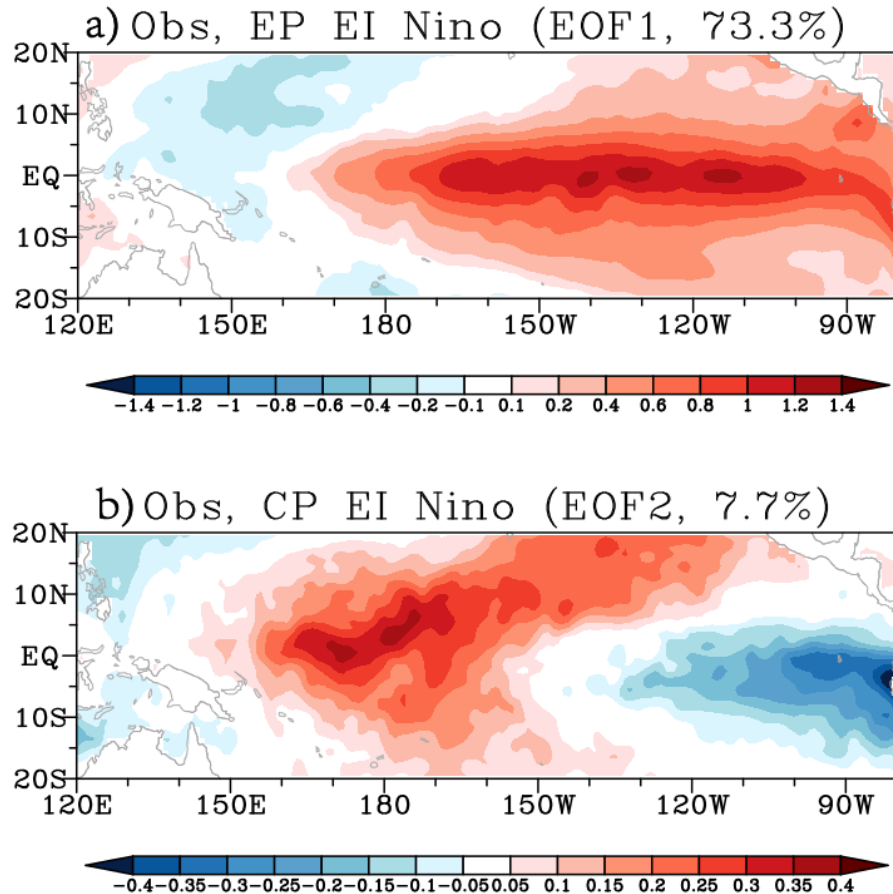


Figure A1 The first and second leading EOF modes of the tropical Pacific SST anomalies (shading; units: $^{\circ}\text{C}$) corresponding to (a) EP and (b) CP El Niño in observations for the 1951–2007 period. Proportion of variance explained by each EOF mode is displayed in brackets at the top of each panel.

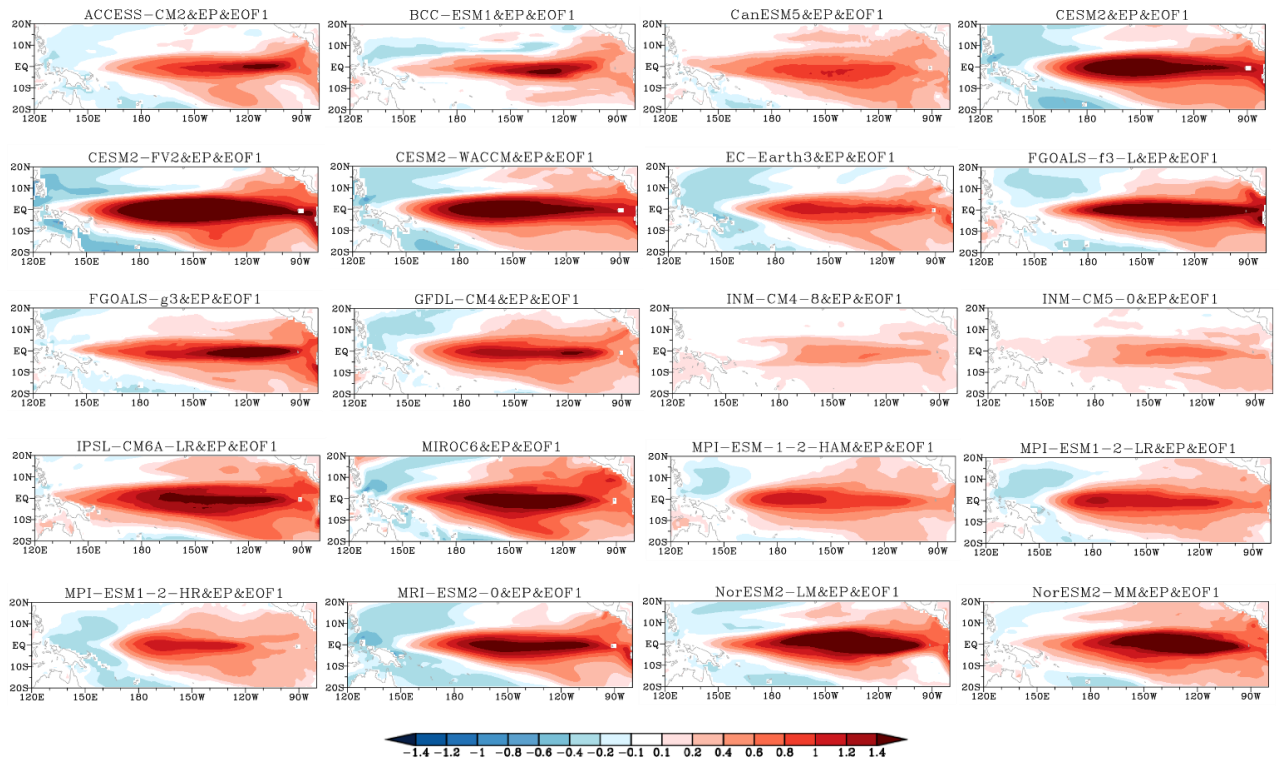


Figure A2 Same as Figure A1, but for the first leading EOF mode of the tropical Pacific SST anomalies (shading; units: $^{\circ}\text{C}$) for each of the 20 selected CMIP6 coupled models.

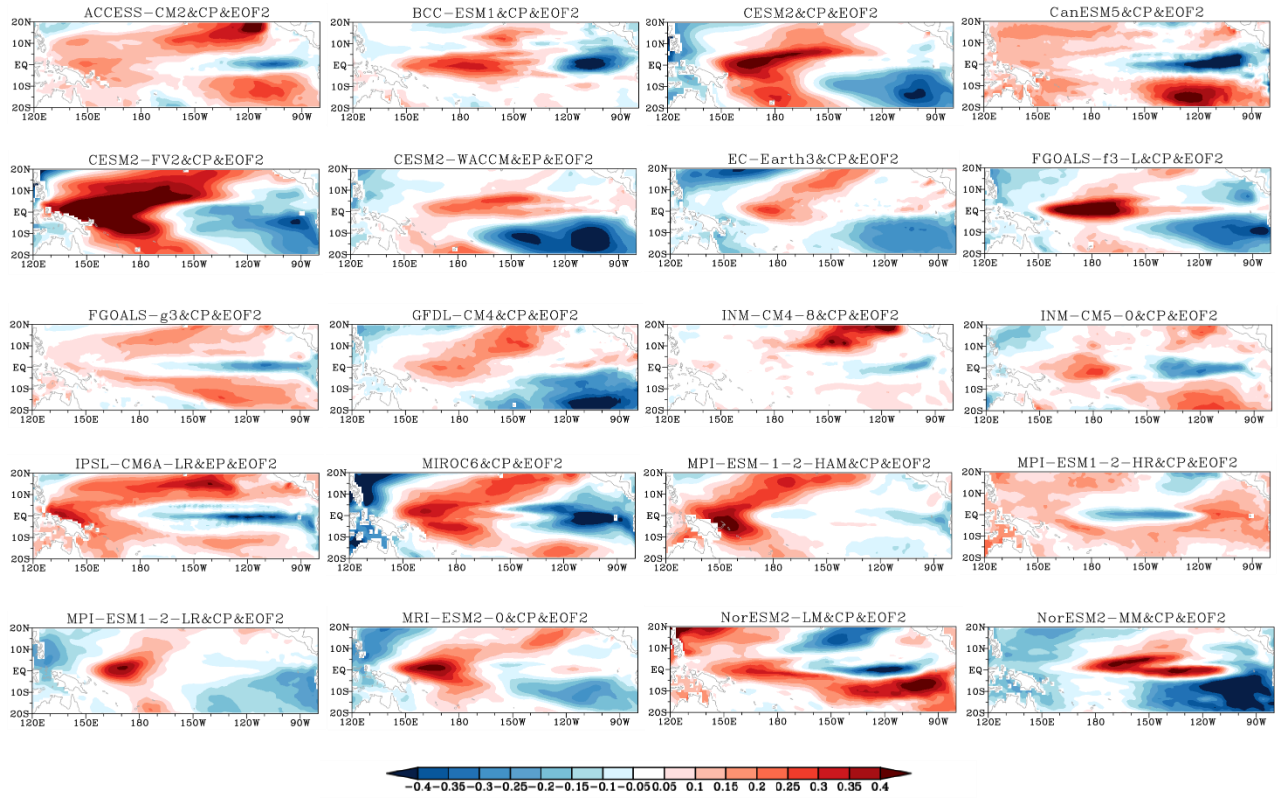


Figure A3 Same as Figure A1, but for the second leading EOF mode of the tropical Pacific SST anomalies (shading; units: $^{\circ}\text{C}$) for each of the 20 selected CMIP6 coupled models.

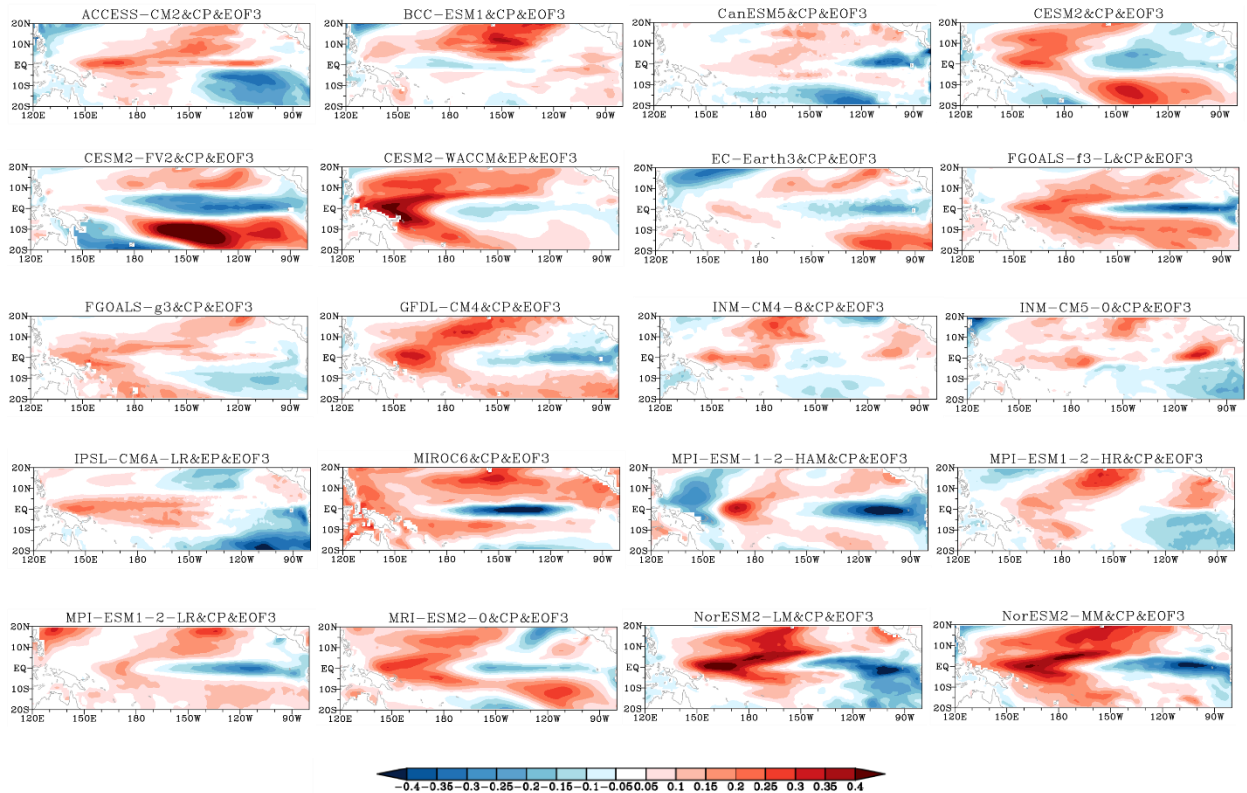


Figure A4 Same as Figure A1, but for the third leading EOF mode of the tropical Pacific SST anomalies (shading; units: $^{\circ}\text{C}$) for each of the 20 selected CMIP6 coupled models.

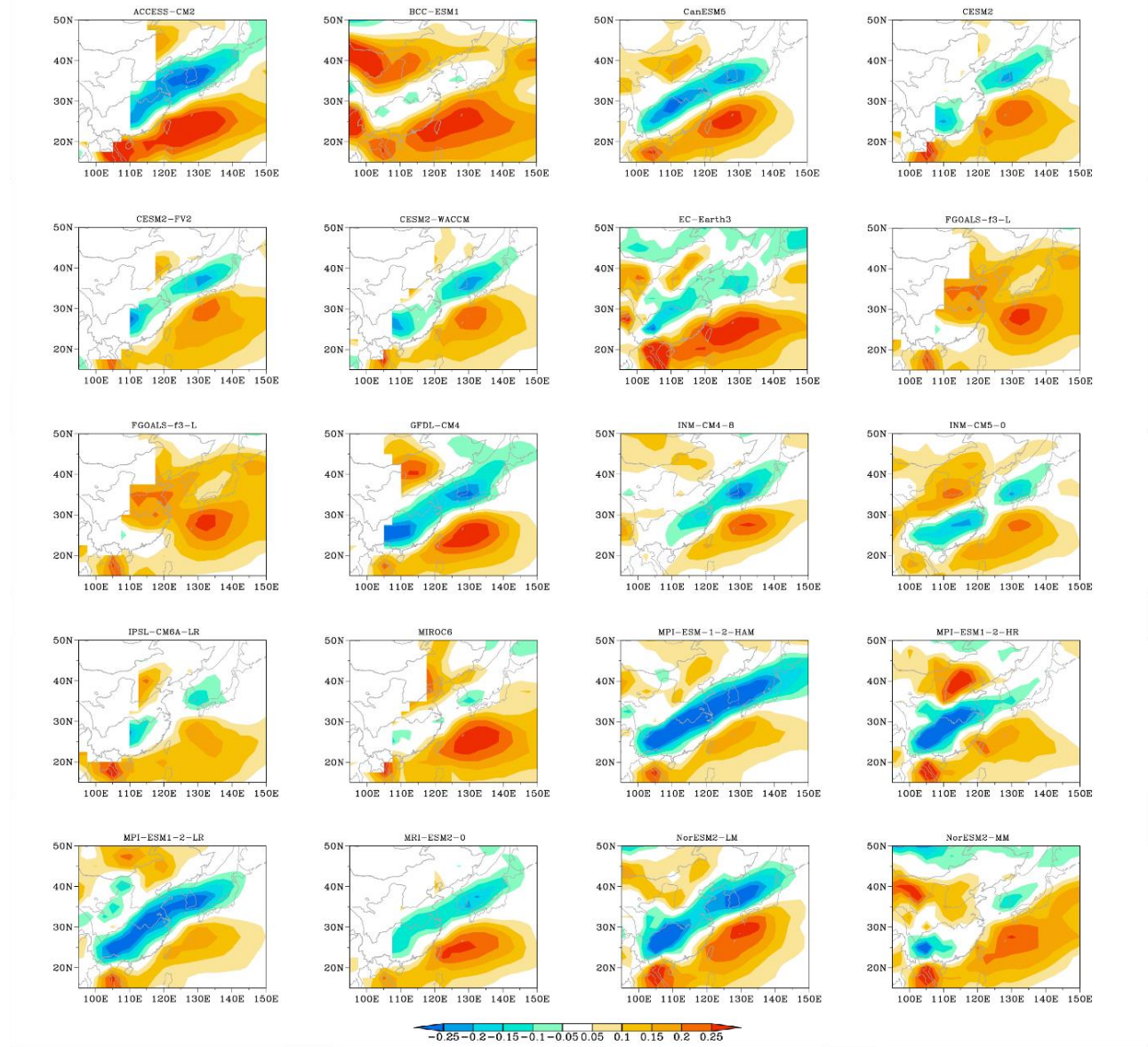


Figure A5 The anomalies of 850 hPa meridional temperature gradient (shading; units: $^{\circ}\text{C m}^{-1} \times 10^{-5}$) associated with the extreme precipitation days in MAM over SEA for each of the 20 selected CMIP6 coupled models.

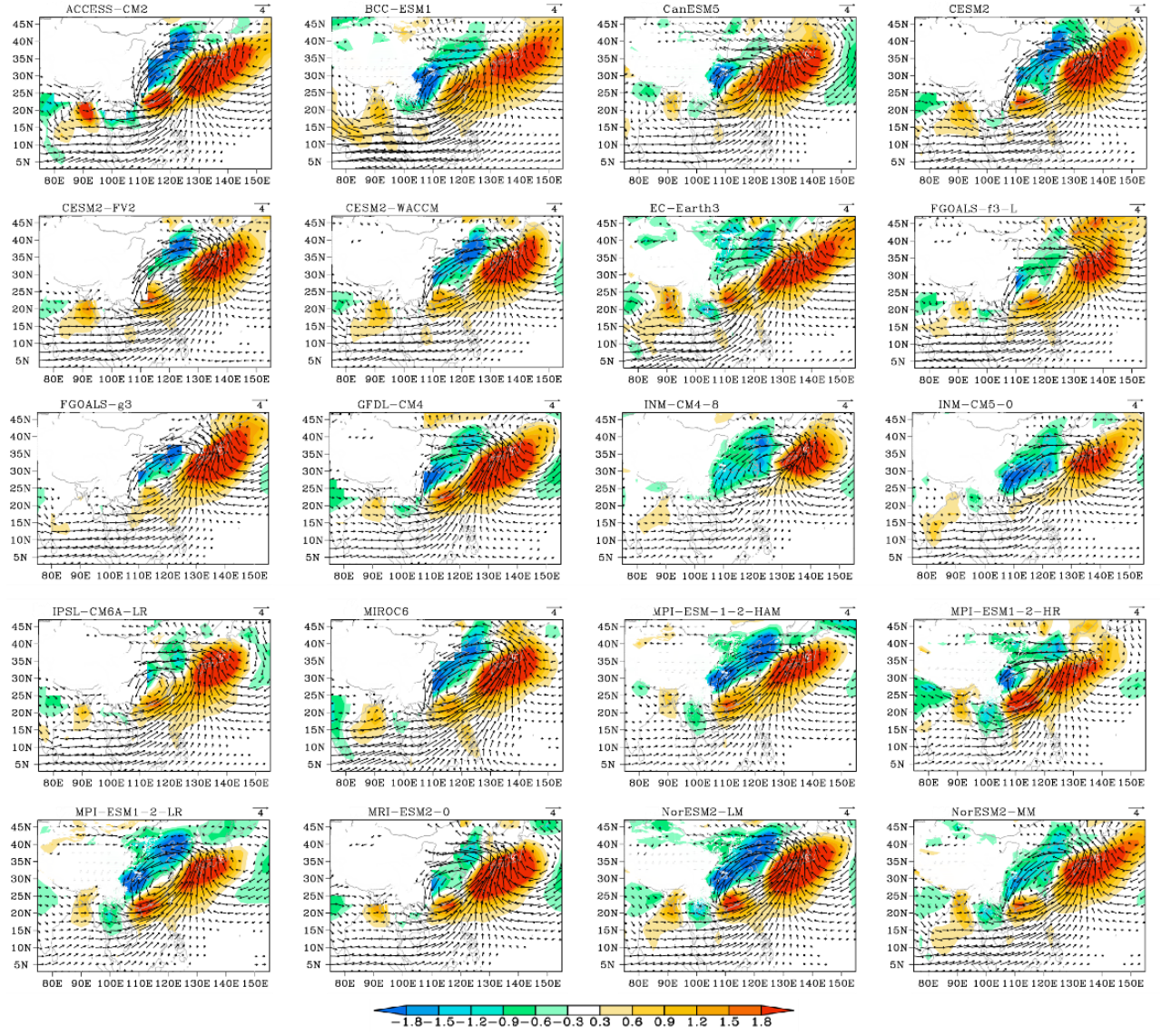


Figure A6 Same as Figure A5 but for 850 hPa wind (vectors; units: m s^{-1}) and temperature advection (shading; units: $^{\circ}\text{C day}^{-1}$); only vectors with magnitudes greater than 0.5 m s^{-1} are shown.

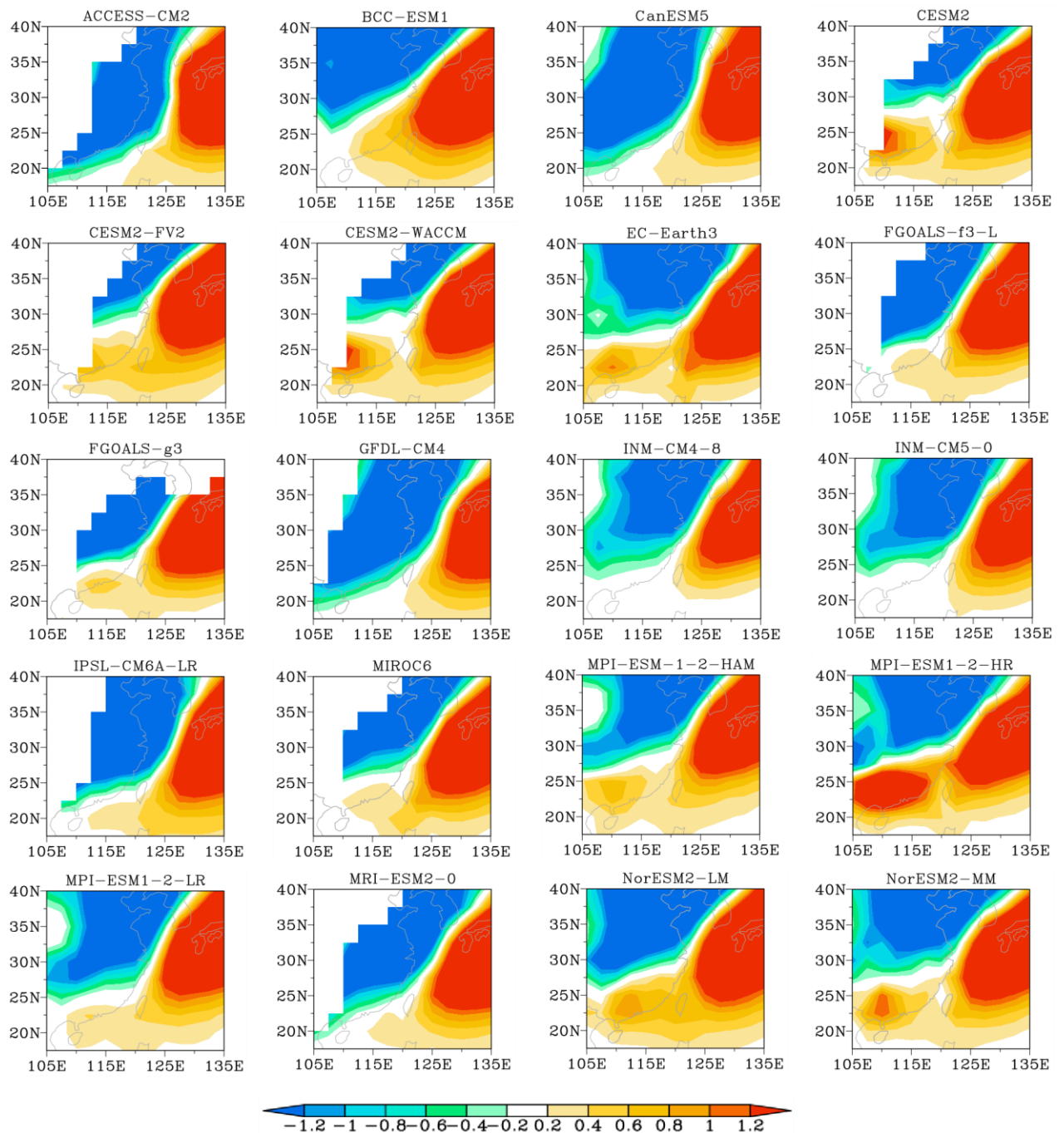


Figure A7 EOF2 mode of daily temperature advection (shading; units: $^{\circ}\text{C day}^{-1}$) at 850 hPa for

each of the 20 selected CMIP6 coupled models.

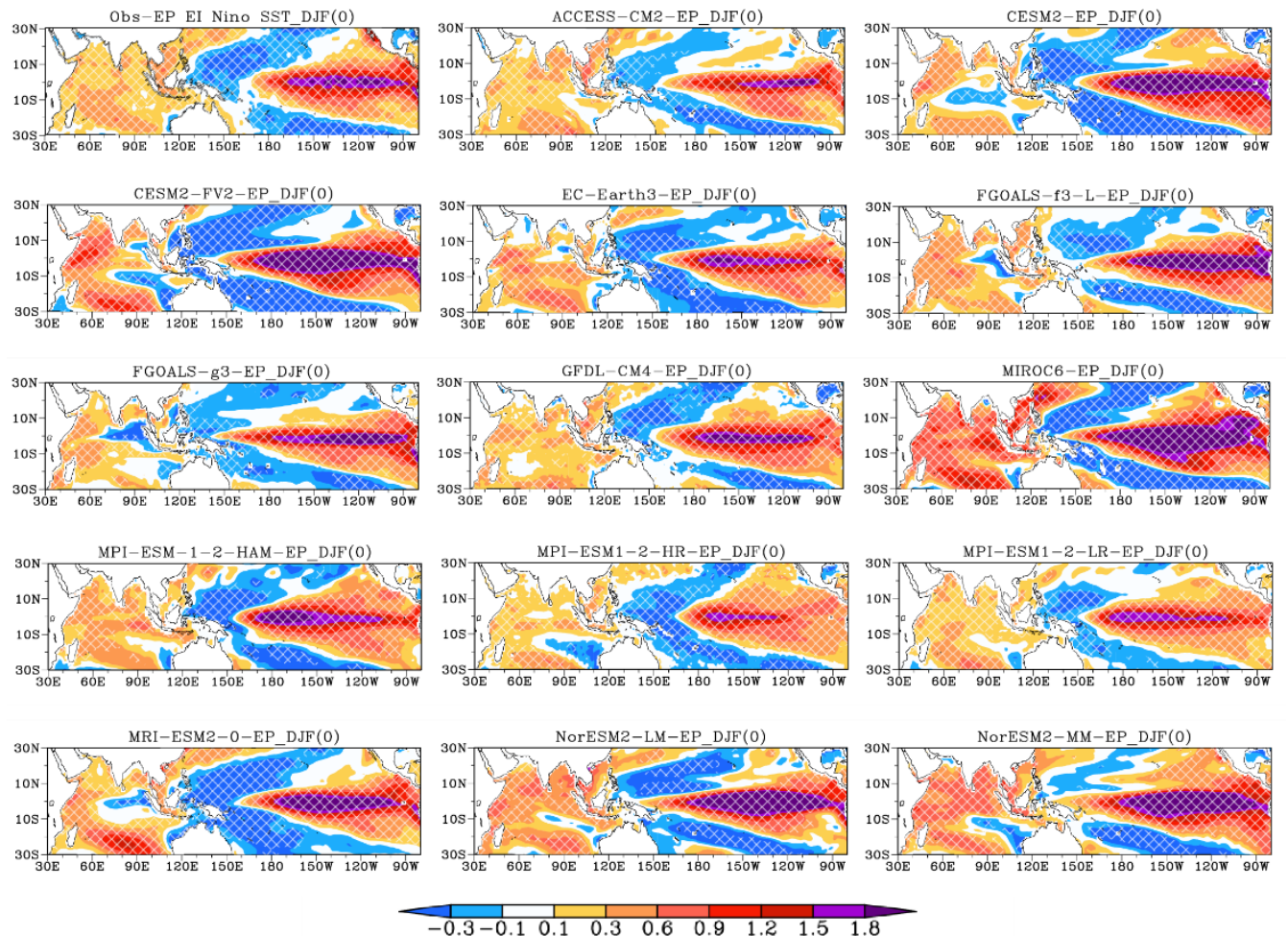


Figure A8 Composite SSTA (shading; units: $^{\circ}\text{C}$) during the DJF(0) for EP El Niño events

based on observations and 14 selected CMIP6 coupled models. The white crosses denote SSTA that are statistically significant at the 95% confidence level.

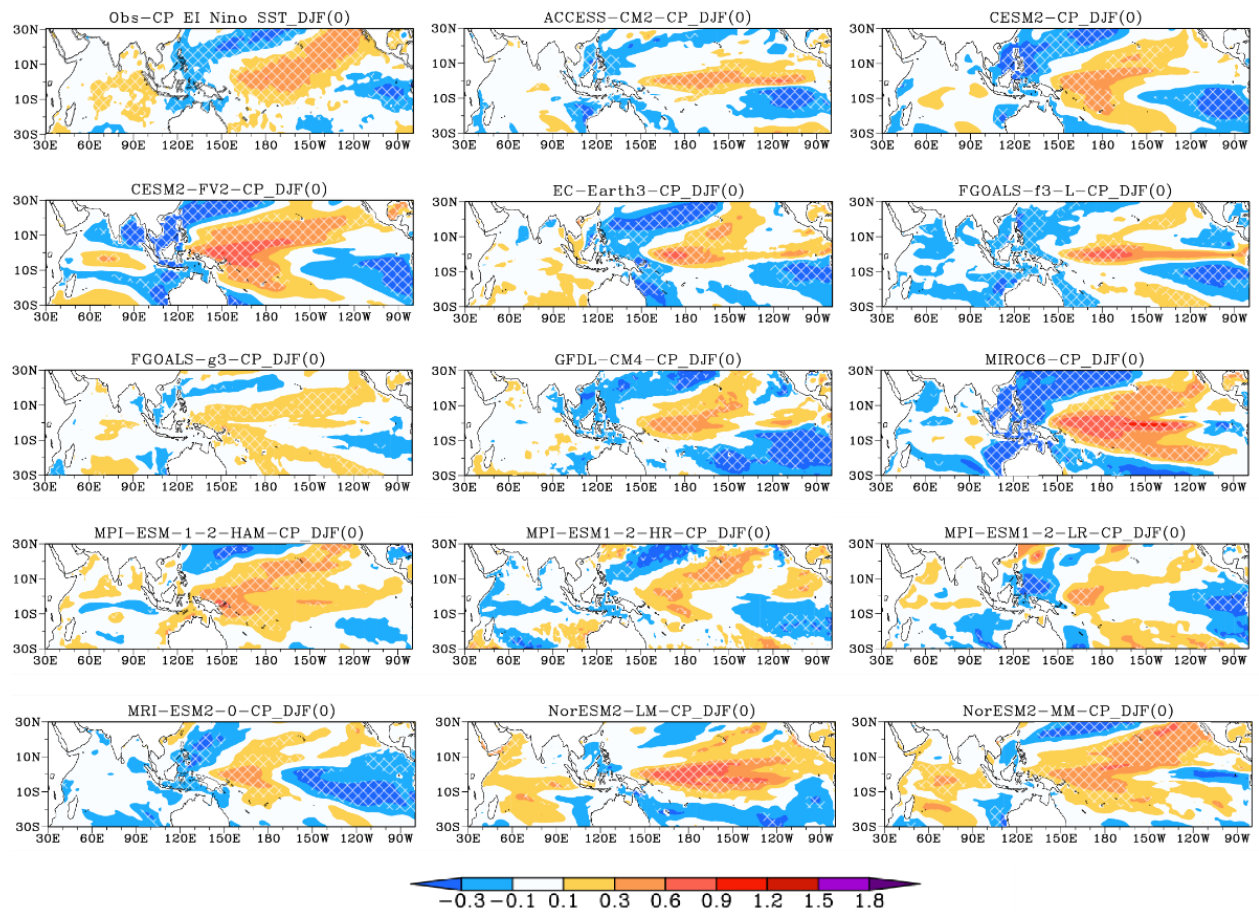


Figure A9 Same as Figure A8 but for CP El Niño.

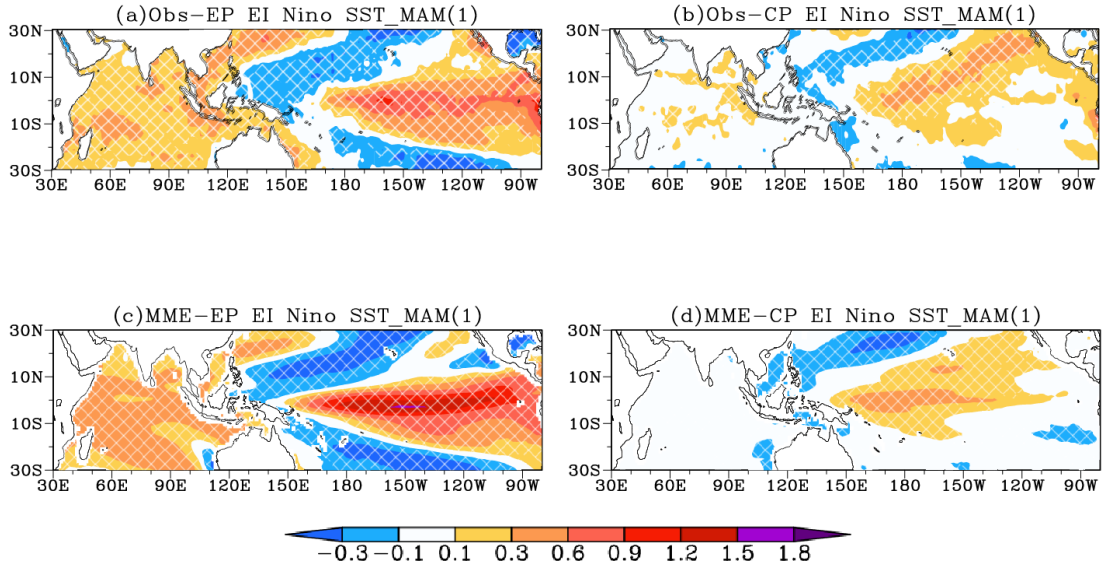


Figure A10 Composite SSTA (shading; units: $^{\circ}\text{C}$) during the MAM(1) for (a, c) EP and (b, d) CP El Niño events based on (a–b) observations and (c–d) CMIP6 MME mean of 14 models. The white crosses for observations denote SSTA that are statistically significant at the 95% confidence level, and the white crosses for models indicate more than 70% of models agree on the sign of SSTA between MME and each model.

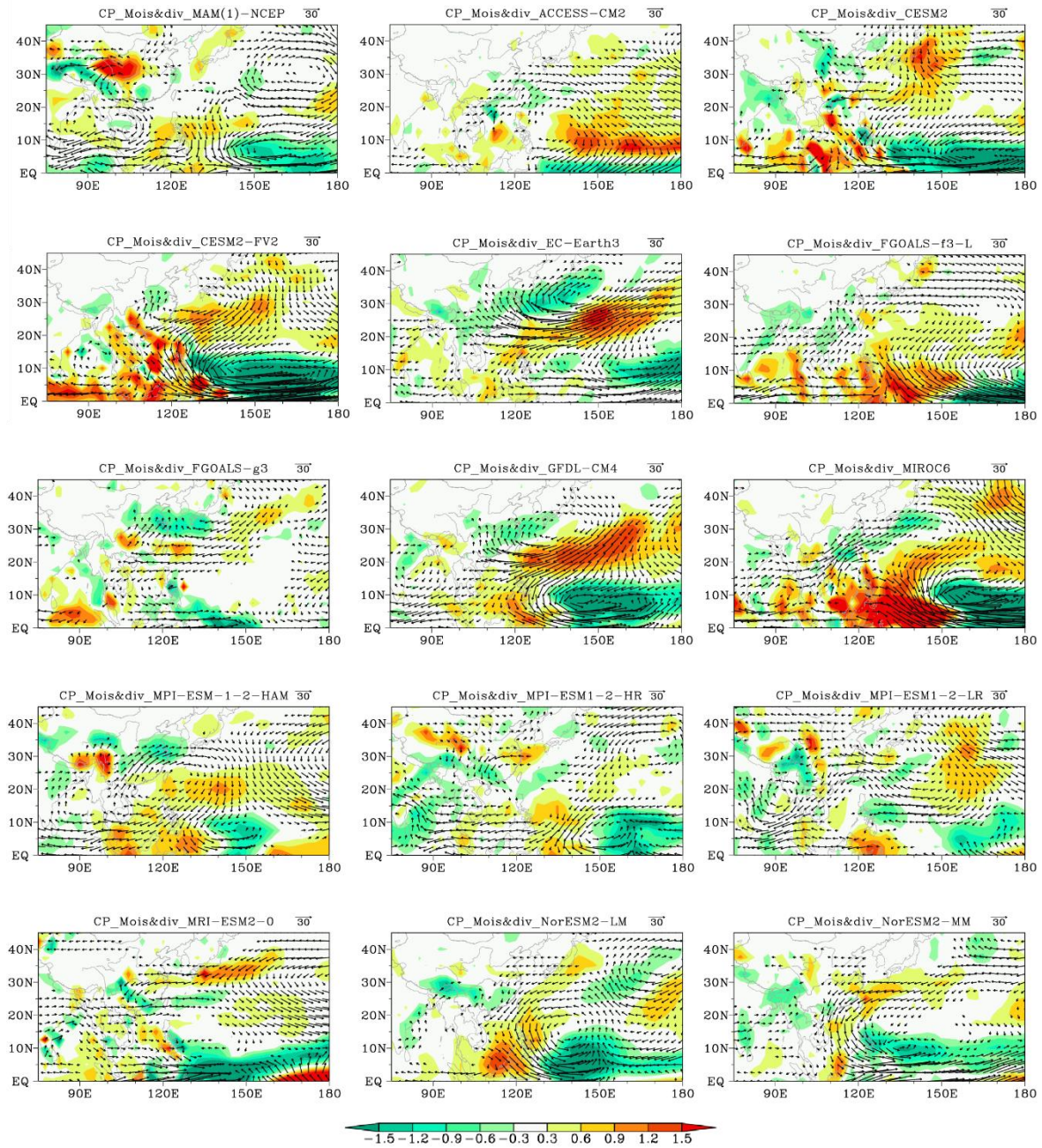


Figure A11 Anomalous vertically integrated moisture flux (vectors; units: $\text{kg m}^{-1} \text{s}^{-1}$) and its divergence (shading; units: mm day^{-1}) during the following MAM season of the CP El Niño events based on observations and each of the 14 selected CMIP6 coupled models. Only moisture flux anomalies $> 5 \text{ kg m}^{-1} \text{s}^{-1}$ are shown.

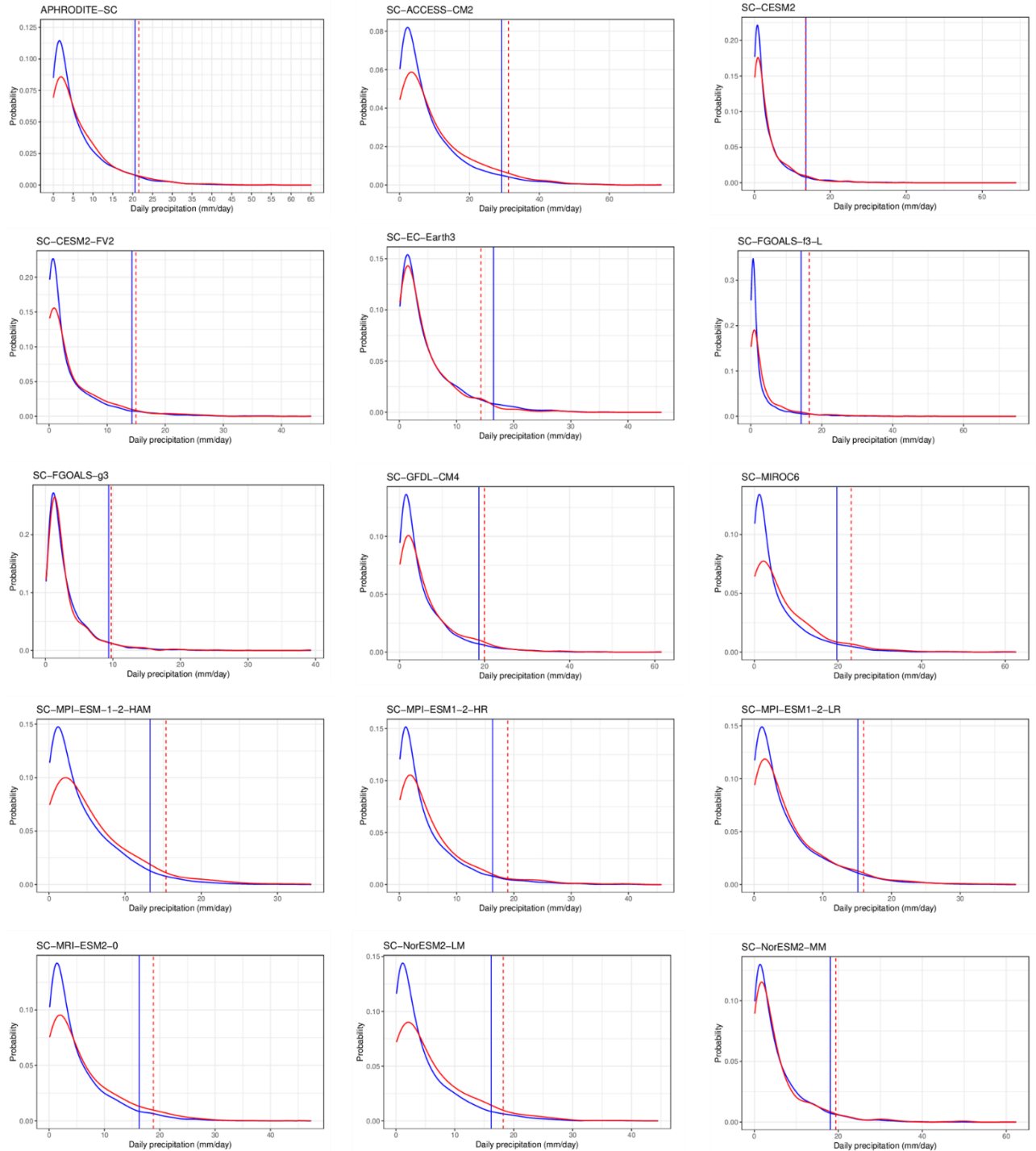


Figure A12 Daily precipitation probability density function (PDF) during EP El Niño (red curve) and all wet days (blue curve) events over the SC region in APHRODITE and 14 CMIP6 models. The 95th percentile values of the daily precipitation associated with EP El Niño (climatology) are indicated by red (blue) vertical dashed (solid) lines.

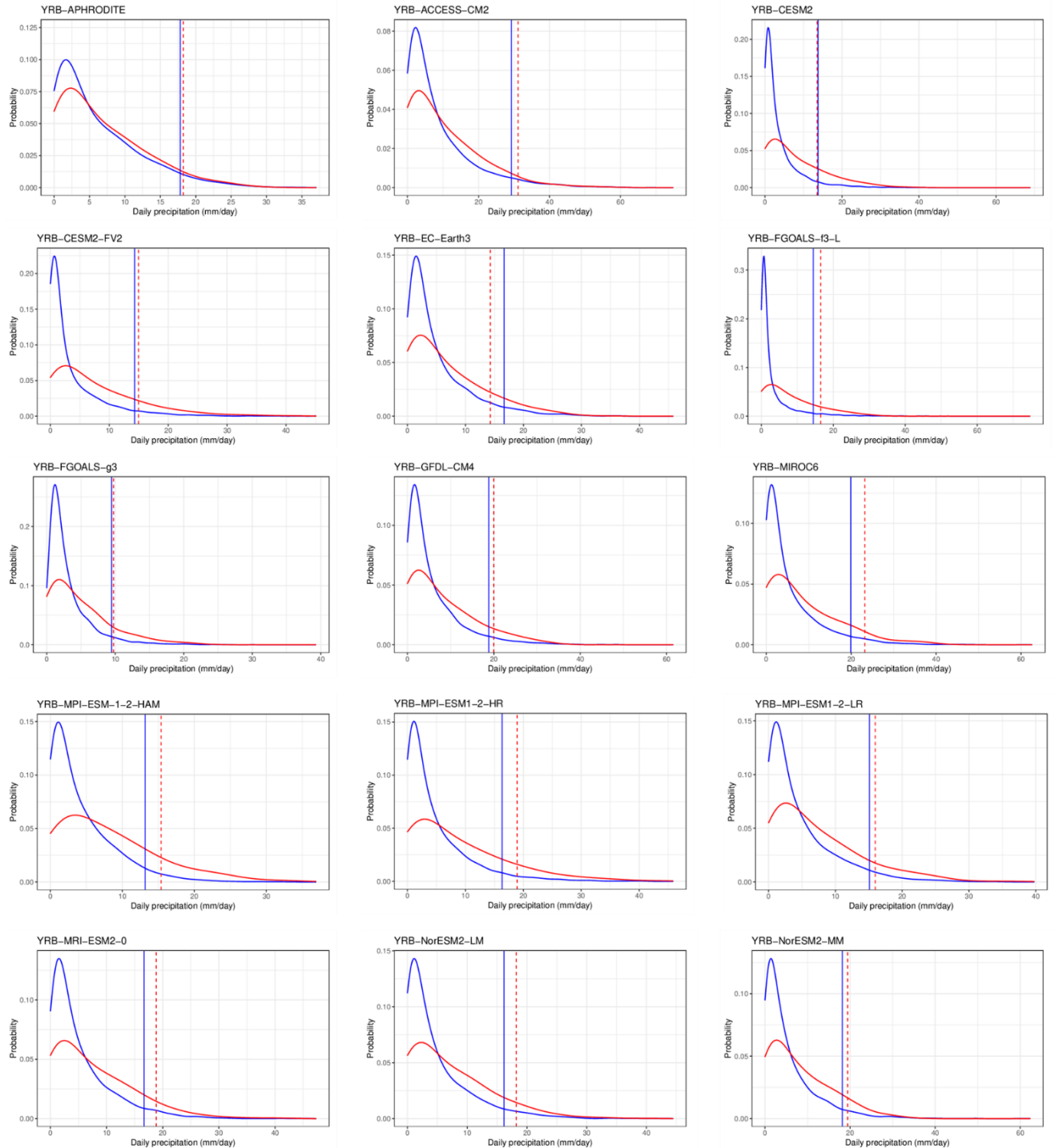


Figure A13 Same as Figure A12 but for the YRB region.

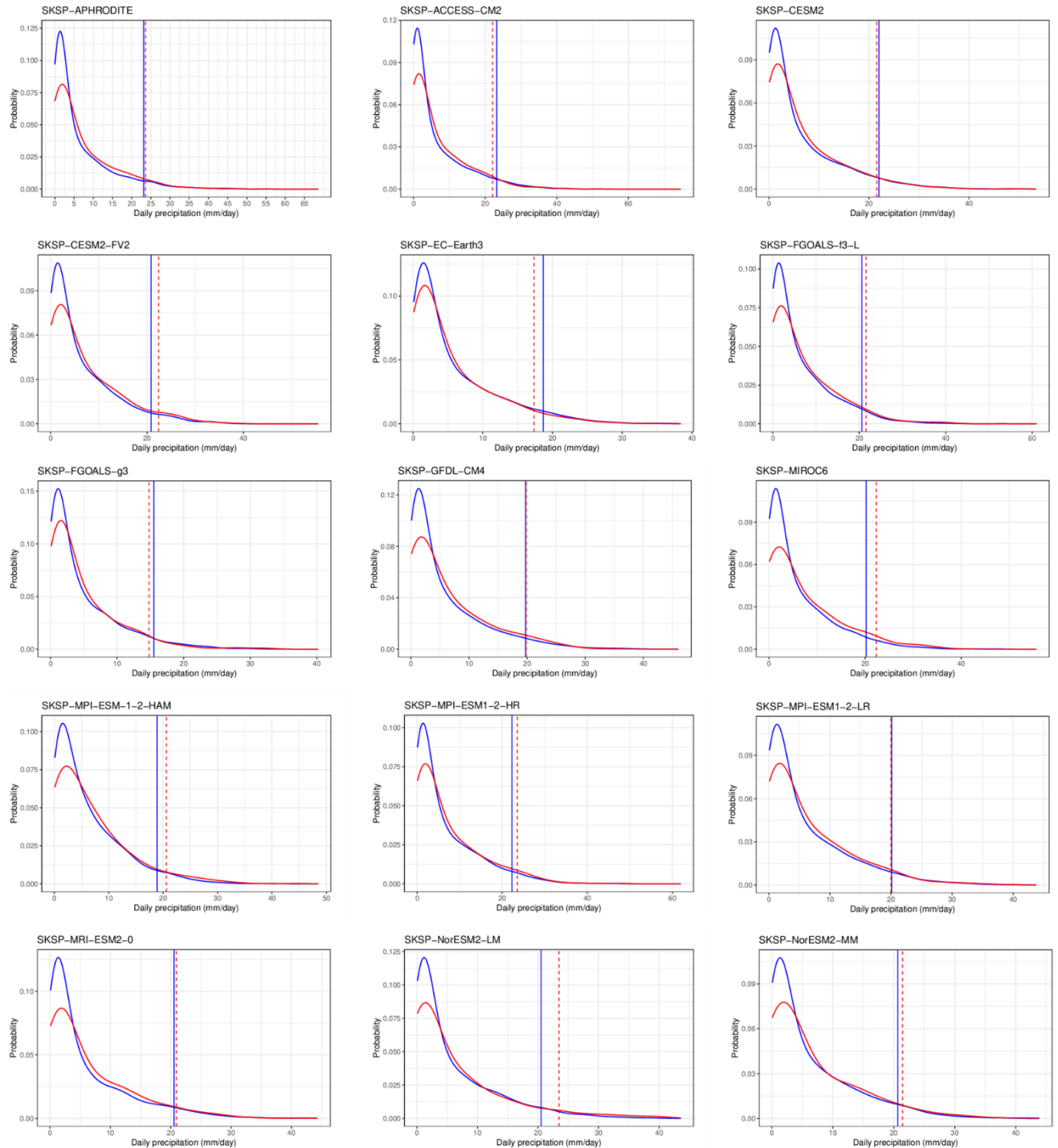


Figure A14 Same as Figure A12 but for the SK-SP region.

Bibliography

- Alexander, L. V., Zhang, X., Peterson, T. C., Caesar, J., Gleason, B., Klein Tank, A. M. G., Haylock, M., Collins, D., Trewin, B., Rahimzadeh, F., Tagipour, A., Rupa Kumar, K., Revadekar, J., Griffiths, G., Vincent, L., Stephenson, D. B., Burn, J., Aguilar, E., Brunet, M., Taylor, M., New, M., Zhai, P., Rusticucci, M., & Vazquez-Aguirre, J. L. (2006). Global observed changes in daily climate extremes of temperature and precipitation. *Journal of Geophysical Research: Atmospheres*, 111(D5). <https://doi.org/10.1029/2005JD006290>
- Alexander, M. A., Bladé, I., Newman, M., Lanzante, J. R., Lau, N.-C., & Scott, J. D. (2002). The Atmospheric Bridge: The Influence of ENSO Teleconnections on Air–Sea Interaction over the Global Oceans. *Journal of Climate*, 15(16), 2205-2231. [https://doi.org/10.1175/1520-0442\(2002\)015<2205:TABTIO>2.0.CO;2](https://doi.org/10.1175/1520-0442(2002)015<2205:TABTIO>2.0.CO;2)
- An, S.-I., Kug, J.-S., Ham, Y.-G., & Kang, I.-S. (2008). Successive Modulation of ENSO to the Future Greenhouse Warming. *Journal of Climate*, 21(1), 3-21. <https://doi.org/10.1175/2007JCLI1500.1>
- Annamalai, H., Liu, P., & Xie, S.-P. (2005). Southwest Indian Ocean SST Variability: Its Local Effect and Remote Influence on Asian Monsoons. *Journal of Climate*, 18(20), 4150-4167. <https://doi.org/10.1175/JCLI3533.1>
- Arnell, N. W., & Lloyd-Hughes, B. (2014). The global-scale impacts of climate change on water resources and flooding under new climate and socio-economic scenarios. *Climatic Change*, 122(1), 127-140. <https://doi.org/10.1007/s10584-013-0948-4>

- Ashok, K., Behera, S. K., Rao, S. A., Weng, H., & Yamagata, T. (2007). El Niño Modoki and its possible teleconnection. *Journal of Geophysical Research: Oceans*, 112(C11).
<https://doi.org/10.1029/2006JC003798>
- Bellenger, H., Guilyardi, E., Leloup, J., Lengaigne, M., & Vialard, J. (2014). ENSO representation in climate models: from CMIP3 to CMIP5. *Climate Dynamics*, 42(7), 1999-2018. <https://doi.org/10.1007/s00382-013-1783-z>
- Cai, W., Santoso, A., Collins, M., Dewitte, B., Karamperidou, C., Kug, J.-S., Lengaigne, M., McPhaden, M. J., Stuecker, M. F., Taschetto, A. S., Timmermann, A., Wu, L., Yeh, S.-W., Wang, G., Ng, B., Jia, F., Yang, Y., Ying, J., Zheng, X.-T., Bayr, T., Brown, J. R., Capotondi, A., Cobb, K. M., Gan, B., Geng, T., Ham, Y.-G., Jin, F.-F., Jo, H.-S., Li, X., Lin, X., McGregor, S., Park, J.-H., Stein, K., Yang, K., Zhang, L., & Zhong, W. (2021). Changing El Niño–Southern Oscillation in a warming climate. *Nature Reviews Earth & Environment*, 2(9), 628-644. <https://doi.org/10.1038/s43017-021-00199-z>
- Cai, W., Wang, G., Santoso, A., McPhaden, M. J., Wu, L., Jin, F.-F., Timmermann, A., Collins, M., Vecchi, G., Lengaigne, M., England, M. H., Dommenech, D., Takahashi, K., & Guilyardi, E. (2015). Increased frequency of extreme La Niña events under greenhouse warming. *Nature Climate Change*, 5(2), 132-137. <https://doi.org/10.1038/nclimate2492>
- Cai, X., Li, Y., Zhang, X. and Bao, Y. (2017) Characteristics of South Asia High in Summer in 2010 and Its Relationship with Rainbands in China. *Journal of Geoscience and Environment Protection*, 5, 210-222. <https://doi.org/10.4236/gep.2017.57016>.

- Chang, C.-P., Lei, Y., Sui, C.-H., Lin, X., & Ren, F. (2012). Tropical cyclone and extreme rainfall trends in East Asian summer monsoon since mid-20th century. *Geophysical Research Letters*, 39(18). <https://doi.org/10.1029/2012GL052945>
- Chang, E. K. M., & Fu, Y. (2002). Interdecadal Variations in Northern Hemisphere Winter Storm Track Intensity. *Journal of Climate*, 15(6), 642-658. [https://doi.org/10.1175/1520-0442\(2002\)015<0642:IVINHW>2.0.CO;2](https://doi.org/10.1175/1520-0442(2002)015<0642:IVINHW>2.0.CO;2)
- Chen, A., He, X., Guan, H., & Zhang, X. (2019). Variability of seasonal precipitation extremes over China and their associations with large-scale ocean–atmosphere oscillations. *International Journal of Climatology*, 39(2), 613-628. <https://doi.org/10.1002/joc.5830>
- Chen, C.-A., Hsu, H.-H., & Liang, H.-C. (2021). Evaluation and comparison of CMIP6 and CMIP5 model performance in simulating the seasonal extreme precipitation in the Western North Pacific and East Asia. *Weather and Climate Extremes*, 31, 100303. <https://doi.org/10.1016/j.wace.2021.100303>
- Chen, C.-A., Hsu, H.-H., Liang, H.-C., Chiu, P.-G., & Tu, C.-Y. (2022). Future change in extreme precipitation in East Asian spring and Mei-yu seasons in two high-resolution AGCMs. *Weather and Climate Extremes*, 35, 100408. <https://doi.org/10.1016/j.wace.2022.100408>
- Chen, G. T.-J., Jiang, Z., & Wu, M.-C. (2003). Spring Heavy Rain Events in Taiwan during Warm Episodes and the Associated Large-Scale Conditions. *Monthly Weather Review*, 131(7), 1173-1188. [https://doi.org/10.1175/1520-0493\(2003\)131<1173:SHREIT>2.0.CO;2](https://doi.org/10.1175/1520-0493(2003)131<1173:SHREIT>2.0.CO;2)

Chen, H., Sun, J., Lin, W., & Xu, H. (2020). Comparison of CMIP6 and CMIP5 models in simulating climate extremes. *Science Bulletin*, 65(17), 1415-1418.
<https://doi.org/10.1016/j.scib.2020.05.015>

Chen, H.-C., & Jin, F.-F. (2021). Simulations of ENSO Phase-Locking in CMIP5 and CMIP6. *Journal of Climate*, 34(12), 5135-5149. <https://doi.org/10.1175/JCLI-D-20-0874.1>

Chen, J., Yu, J.-Y., Wang, X., & Lian, T. (2020). Different Influences of Southeastern Indian Ocean and Western Indian Ocean SST Anomalies on Eastern China Rainfall during the Decaying Summer of the 2015/16 Extreme El Niño. *Journal of Climate*, 33(13), 5427-5443. <https://doi.org/10.1175/JCLI-D-19-0777.1>

Chen, M., & Li, T. (2021). ENSO evolution asymmetry: EP versus CP El Niño. *Climate Dynamics*, 56(11), 3569-3579. <https://doi.org/10.1007/s00382-021-05654-7>

Chen, S., Liu, B., Tan, X., & Huang, Z. (2019). Characteristics and circulation background of extreme precipitation over East China. *Natural Hazards*, 99(1), 537-552. <https://doi.org/10.1007/s11069-019-03758-2>

Chen, W., Feng, J., & Wu, R. (2013). Roles of ENSO and PDO in the Link of the East Asian Winter Monsoon to the following Summer Monsoon. *Journal of Climate*, 26(2), 622-635. <https://doi.org/10.1175/JCLI-D-12-00021.1>

Chen, X., Wu, P., Roberts, M. J., & Zhou, T. (2018). Potential Underestimation of Future Mei-Yu Rainfall with Coarse-Resolution Climate Models. *Journal of Climate*, 31(17), 6711-6727. <https://doi.org/10.1175/JCLI-D-17-0741.1>

Chen, Z., Wen, Z., Wu, R., Lin, X., & Wang, J. (2016). Relative importance of tropical SST anomalies in maintaining the Western North Pacific anomalous anticyclone during El

Niño to La Niña transition years. *Climate Dynamics*, 46(3), 1027-1041.

<https://doi.org/10.1007/s00382-015-2630-1>

Collins, M., An, S.-I., Cai, W., Ganachaud, A., Guilyardi, E., Jin, F.-F., Jochum, M., Lengaigne, M., Power, S., Timmermann, A., Vecchi, G., & Wittenberg, A. (2010). The impact of global warming on the tropical Pacific Ocean and El Niño. *Nature Geoscience*, 3(6), 391-397. <https://doi.org/10.1038/ngeo868>

Cui, D., Wang, C., & Santisirisomboon, J. (2019). Characteristics of extreme precipitation over eastern Asia and its possible connections with Asian summer monsoon activity. *International Journal of Climatology*, 39(2), 711-723. <https://doi.org/10.1002/joc.5837>

Dai, A. (2006). Precipitation Characteristics in Eighteen Coupled Climate Models. *Journal of Climate*, 19(18), 4605-4630. <https://doi.org/10.1175/JCLI3884.1>

Donat, M. G., Alexander, L. V., Yang, H., Durre, I., Vose, R., & Caesar, J. (2013). Global Land-Based Datasets for Monitoring Climatic Extremes. *Bulletin of the American Meteorological Society*, 94(7), 997-1006. <https://doi.org/10.1175/BAMS-D-12-00109.1>

Donat, M. G., Alexander, L. V., Yang, H., Durre, I., Vose, R., Dunn, R. J. H., Willett, K. M., Aguilar, E., Brunet, M., Caesar, J., Hewitson, B., Jack, C., Klein Tank, A. M. G., Kruger, A. C., Marengo, J., Peterson, T. C., Renom, M., Oria Rojas, C., Rusticucci, M., Salinger, J., Elrayah, A. S., Sekele, S. S., Srivastava, A. K., Trewin, B., Villarroel, C., Vincent, L. A., Zhai, P., Zhang, X., & Kitching, S. (2013). Updated analyses of temperature and precipitation extreme indices since the beginning of the twentieth century: The HadEX2 dataset. *Journal of Geophysical Research: Atmospheres*, 118(5), 2098-2118. <https://doi.org/10.1002/jgrd.50150>

Dong, T., & Dong, W. (2021). Evaluation of extreme precipitation over Asia in CMIP6 models.

Climate Dynamics, 57(7), 1751-1769. <https://doi.org/10.1007/s00382-021-05773-1>

Endo, H., & Kitoh, A. (2014). Thermodynamic and dynamic effects on regional monsoon rainfall changes in a warmer climate. *Geophysical Research Letters*, 41(5), 1704-1711. <https://doi.org/10.1002/2013GL059158>

Eyring, V., Bony, S., Meehl, G. A., Senior, C. A., Stevens, B., Stouffer, R. J., & Taylor, K. E. (2016). Overview of the Coupled Model Intercomparison Project Phase 6 (CMIP6) experimental design and organization. *Geosci. Model Dev.*, 9(5), 1937-1958. <https://doi.org/10.5194/gmd-9-1937-2016>

Feng, J., Chen, W., & Li, Y. (2017). Asymmetry of the winter extra-tropical teleconnections in the Northern Hemisphere associated with two types of ENSO. *Climate Dynamics*, 48(7), 2135-2151. <https://doi.org/10.1007/s00382-016-3196-2>

Feng, J., Chen, W., Gong, H., Ying, J., & Jiang, W. (2019). An investigation of CMIP5 model biases in simulating the impacts of central Pacific El Niño on the East Asian summer monsoon. *Climate Dynamics*, 52(5), 2631-2646. <https://doi.org/10.1007/s00382-018-4284-2>

Feng, J., Chen, W., Tam, C. Y., & Zhou, W. (2011). Different impacts of El Niño and El Niño Modoki on China rainfall in the decaying phases. *International Journal of Climatology*, 31(14), 2091-2101. <https://doi.org/10.1002/joc.2217>

Feng, J., Li, J., Zheng, F., Xie, F., & Sun, C. (2016). Contrasting Impacts of Developing Phases of Two Types of El Niño on Southern China Rainfall. *Journal of the*

Meteorological Society of Japan. 2, 94(4), 359-370. <https://doi.org/10.2151/jmsj.2016-019>

Feng, J., Lian, T., Ying, J., Li, J., & Li, G. (2020). Do CMIP5 Models Show El Niño Diversity?

Journal of Climate, 33(5), 1619-1641. <https://doi.org/10.1175/JCLI-D-18-0854.1>

Feng, Z., & Sixiong, Z. (2004). A study of formation and development of one kind of cyclone on the mei-yu (Baiu) front. *Advances in Atmospheric Sciences*, 21(5), 741-754. <https://doi.org/10.1007/BF02916371>

Ferrett, S., & Collins, M. (2019). ENSO feedbacks and their relationships with the mean state in a flux adjusted ensemble. *Climate Dynamics*, 52(12), 7189-7208. <https://doi.org/10.1007/s00382-016-3270-9>

Freund, M. B., Brown, J. R., Henley, B. J., Karoly, D. J., & Brown, J. N. (2020). Warming Patterns Affect El Niño Diversity in CMIP5 and CMIP6 Models. *Journal of Climate*, 33(19), 8237-8260. <https://doi.org/10.1175/JCLI-D-19-0890.1>

Freychet, N., Tett, S. F. B., Tian, F., Li, S., Dong, B., & Sparrow, S. (2022). Physical processes of summer extreme rainfall interannual variability in Eastern China—part II: evaluation of CMIP6 models. *Climate Dynamics*, 59(1), 455-469. <https://doi.org/10.1007/s00382-022-06137-z>

Fu, Y., Lin, Z., & Guo, D. (2020). Improvement of the simulation of the summer East Asian westerly jet from CMIP5 to CMIP6. *Atmospheric and Oceanic Science Letters*, 13(6), 550-558. <https://doi.org/10.1080/16742834.2020.1746175>

Fu, Y., Lin, Z., & Wang, T. (2021). Preconditions for CMIP6 models to reproduce the relationship between wintertime ENSO and subsequent East Asian summer rainfall.

Climate Research, 84, 133-144. <https://www.int-res.com/abstracts/cr/v84/p133-144/>

Fu, Y., Lu, R., & Guo, D. (2021). Projected Increase in Probability of East Asian Heavy Rainy Summer in the 21st Century by CMIP5 Models. *Advances in Atmospheric Sciences*, 38(10), 1635-1650. <https://doi.org/10.1007/s00376-021-0347-0>

Gill, A. E. (1980). Some simple solutions for heat-induced tropical circulation. *Quarterly Journal of the Royal Meteorological Society*, 106(449), 447-462.
<https://doi.org/10.1002/qj.49710644905>

Grotjahn, R. (2003). Baroclinic instability. *Encyclopedia of Atmospheric Sciences*, 179(188), 00076-00072.

Guo, L., Klingaman, N. P., Vidale, P. L., Turner, A. G., Demory, M.-E., & Cobb, A. (2017). Contribution of Tropical Cyclones to Atmospheric Moisture Transport and Rainfall over East Asia. *Journal of Climate*, 30(10), 3853-3865. <https://doi.org/10.1175/JCLI-D-16-0308.1>

Guo, Z., Zhou, T., & Wu, B. (2017). The asymmetric effects of El Niño and La Niña on the East Asian winter monsoon and their simulation by CMIP5 atmospheric models. *Journal of Meteorological Research*, 31(1), 82-93. <https://doi.org/10.1007/s13351-017-6095-5>

Haarsma, R. J., Hazeleger, W., Severijns, C., de Vries, H., Sterl, A., Bintanja, R., van Oldenborgh, G. J., & van den Brink, H. W. (2013). More hurricanes to hit western Europe due to global warming. *Geophysical Research Letters*, 40(9), 1783-1788.
<https://doi.org/10.1002/grl.50360>

- Horel, J. D., & Wallace, J. M. (1981). Planetary-Scale Atmospheric Phenomena Associated with the Southern Oscillation. *Monthly Weather Review*, 109(4), 813-829.
[https://doi.org/10.1175/1520-0493\(1981\)109<0813:PSAPAW>2.0.CO;2](https://doi.org/10.1175/1520-0493(1981)109<0813:PSAPAW>2.0.CO;2)
- Hoskins, B. J., & Karoly, D. J. (1981). The Steady Linear Response of a Spherical Atmosphere to Thermal and Orographic Forcing. *Journal of Atmospheric Sciences*, 38(6), 1179-1196.
[https://doi.org/10.1175/1520-0469\(1981\)038<1179:TSLROA>2.0.CO;2](https://doi.org/10.1175/1520-0469(1981)038<1179:TSLROA>2.0.CO;2)
- Hou, M., & Tang, Y. (2022). Recent progress in simulating two types of ENSO – from CMIP5 to CMIP6 [Original Research]. *Frontiers in Marine Science*, 9.
<https://www.frontiersin.org/articles/10.3389/fmars.2022.986780>
- Hsu, P.-C., & Li, T. (2011). Interactions between Boreal Summer Intraseasonal Oscillations and Synoptic-Scale Disturbances over the Western North Pacific. Part II: Apparent Heat and Moisture Sources and Eddy Momentum Transport. *Journal of Climate*, 24(3), 942-961. <https://doi.org/https://doi.org/10.1175/2010JCLI3834.1>
- Huang, D.-Q., Zhu, J., Zhang, Y.-C., Wang, J., & Kuang, X.-Y. (2015). The Impact of the East Asian Subtropical Jet and Polar Front Jet on the Frequency of Spring Persistent Rainfall over Southern China in 1997–2011. *Journal of Climate*, 28(15), 6054-6066.
<https://doi.org/10.1175/JCLI-D-14-00641.1>
- Huang, G., Qu, X., & Hu, K. (2011). The impact of the tropical Indian Ocean on South Asian High in boreal summer. *Advances in Atmospheric Sciences*, 28(2), 421-432.
<https://doi.org/10.1007/s00376-010-9224-y>

Jiang, H., & Zipser, E. J. (2010). Contribution of Tropical Cyclones to the Global Precipitation from Eight Seasons of TRMM Data: Regional, Seasonal, and Interannual Variations.

Journal of Climate, 23(6), 1526-1543. <https://doi.org/10.1175/2009JCLI3303.1>

Jiang, W., Gong, H., Huang, P., Wang, L., Huang, G., & Hu, L. (2022). Biases and improvements of the ENSO-East Asian winter monsoon teleconnection in CMIP5 and CMIP6 models. *Climate Dynamics*, 59(7), 2467-2480. <https://doi.org/10.1007/s00382-022-06220-5>

Jiang, W., Huang, G., Hu, K., Wu, R., Gong, H., Chen, X., & Tao, W. (2017). Diverse Relationship between ENSO and the Northwest Pacific Summer Climate among CMIP5 Models: Dependence on the ENSO Decay Pace. *Journal of Climate*, 30(1), 109-127. <https://doi.org/10.1175/JCLI-D-16-0365.1>

Jiang, W., Huang, G., Huang, P., Wu, R., Hu, K., & Chen, W. (2019). Northwest Pacific Anticyclonic Anomalies during Post-El Niño Summers Determined by the Pace of El Niño Decay. *Journal of Climate*, 32(12), 3487-3503. <https://doi.org/10.1175/JCLI-D-18-0793.1>

Jiang, W., Huang, P., Huang, G., & Ying, J. (2021). Origins of the Excessive Westward Extension of ENSO SST Simulated in CMIP5 and CMIP6 Models. *Journal of Climate*, 34(8), 2839-2851. <https://doi.org/10.1175/JCLI-D-20-0551.1>

Jiang, W., Huang, P., Li, G., & Huang, G. (2020). Emergent Constraint on the Frequency of Central Pacific El Niño Under Global Warming by the Equatorial Pacific Cold Tongue Bias in CMIP5/6 Models. *Geophysical Research Letters*, 47(19), e2020GL089519. <https://doi.org/10.1029/2020GL089519>

- Kao, H.-Y., & Yu, J.-Y. (2009). Contrasting Eastern-Pacific and Central-Pacific Types of ENSO. *Journal of Climate*, 22(3), 615-632. <https://doi.org/10.1175/2008JCLI2309.1>
- Kerr, R. A. (2007). Global Warming Is Changing the World. *Science*, 316(5822), 188-190. <https://doi.org/10.1126/science.316.5822.188>
- Kim, I.-W., Oh, J., Woo, S., & Kripalani, R. H. (2019). Evaluation of precipitation extremes over the Asian domain: observation and modelling studies. *Climate Dynamics*, 52(3), 1317-1342. <https://doi.org/10.1007/s00382-018-4193-4>
- Kim, J.-W., & An, S.-I. (2019). Western North Pacific anticyclone change associated with the El Niño–Indian Ocean Dipole coupling. *International Journal of Climatology*, 39(5), 2505-2521. <https://doi.org/10.1002/joc.5967>
- Kim, S. T., & Yu, J.-Y. (2012). The two types of ENSO in CMIP5 models. *Geophysical Research Letters*, 39(11). <https://doi.org/10.1029/2012GL052006>
- Kim, Y.-H., Min, S.-K., Zhang, X., Zwiers, F., Alexander, L. V., Donat, M. G., & Tung, Y.-S. (2016). Attribution of extreme temperature changes during 1951–2010. *Climate Dynamics*, 46(5), 1769-1782. <https://doi.org/10.1007/s00382-015-2674-2>
- Kosaka, Y., & Nakamura, H. (2006). Structure and dynamics of the summertime Pacific–Japan teleconnection pattern. *Quarterly Journal of the Royal Meteorological Society*, 132(619), 2009-2030. <https://doi.org/10.1256/qj.05.204>
- Kug, J.-S., Jin, F.-F., & An, S.-I. (2009). Two Types of El Niño Events: Cold Tongue El Niño and Warm Pool El Niño. *Journal of Climate*, 22(6), 1499-1515. <https://doi.org/10.1175/2008JCLI2624.1>

- Larkin, N. K., & Harrison, D. E. (2005). On the definition of El Niño and associated seasonal average U.S. weather anomalies. *Geophysical Research Letters*, 32(13).
<https://doi.org/10.1029/2005GL022738>
- Lau, N.-C. (1997). Interactions between Global SST Anomalies and the Midlatitude Atmospheric Circulation. *Bulletin of the American Meteorological Society*, 78(1), 21-34.
[https://doi.org/10.1175/1520-0477\(1997\)078<0021:IBGSAA>2.0.CO;2](https://doi.org/10.1175/1520-0477(1997)078<0021:IBGSAA>2.0.CO;2)
- Lee, S. (2000). Barotropic Effects on Atmospheric Storm Tracks. *Journal of the Atmospheric Sciences*, 57(9), 1420-1435. [https://doi.org/10.1175/1520-0469\(2000\)057<1420:BEOAST>2.0.CO;2](https://doi.org/10.1175/1520-0469(2000)057<1420:BEOAST>2.0.CO;2)
- Li, D., Zhou, T., & Zhang, W. (2019). Extreme precipitation over East Asia under 1.5 °C and 2 °C global warming targets: a comparison of stabilized and overshoot projections. *Environmental Research Communications*, 1(8), 085002. <https://doi.org/10.1088/2515-7620/ab3971>
- Li, G., & Xie, S.-P. (2014). Tropical Biases in CMIP5 Multimodel Ensemble: The Excessive Equatorial Pacific Cold Tongue and Double ITCZ Problems. *Journal of Climate*, 27(4), 1765-1780. <https://doi.org/10.1175/JCLI-D-13-00337.1>
- Li, G., Jian, Y., Yang, S., Du, Y., Wang, Z., Li, Z., Zhuang, W., Jiang, W., & Huang, G. (2019). Effect of excessive equatorial Pacific cold tongue bias on the El Niño-Northwest Pacific summer monsoon relationship in CMIP5 multi-model ensemble. *Climate Dynamics*, 52(9), 6195-6212. <https://doi.org/10.1007/s00382-018-4504-9>

Li, J., & Wang, B. (2018). Predictability of summer extreme precipitation days over eastern China. *Climate Dynamics*, 51(11), 4543-4554. <https://doi.org/10.1007/s00382-017-3848-x>

Li, J., Huo, R., Chen, H., Zhao, Y., & Zhao, T. (2021). Comparative Assessment and Future Prediction Using CMIP6 and CMIP5 for Annual Precipitation and Extreme Precipitation Simulation [Original Research]. *Frontiers in Earth Science*, 9. <https://www.frontiersin.org/articles/10.3389/feart.2021.687976>

Li, R. K. K., Tam, C. Y., & Lau, N. C. (2021). Effects of ENSO diversity and cold tongue bias on seasonal prediction of South China late spring rainfall. *Climate Dynamics*, 57(1), 577-591. <https://doi.org/10.1007/s00382-021-05732-w>

Li, R. K. K., Tam, C.-Y., Lau, N.-C., Sohn, S.-J., Ahn, J.-B., & O'Reilly, C. (2021). Forcing mechanism of the Silk Road pattern and the sensitivity of Rossby-wave source hotspots to mean-state winds. *Quarterly Journal of the Royal Meteorological Society*, 147(737), 2533-2546. <https://doi.org/10.1002/qj.4039>

Li, Y., Lau, N.-C., Tam, C.-Y., Cheung, H.-N., Deng, Y., & Zhang, H. (2021). Projected changes in the characteristics of the East Asian summer monsoonal front and their impacts on the regional precipitation. *Climate Dynamics*, 56(11), 4013-4026. <https://doi.org/10.1007/s00382-021-05687-y>

Li, Y., Ma, B., Feng, J., & Lu, Y. (2019). Influence of the strongest central Pacific El Niño–Southern Oscillation events on the precipitation in eastern China. *International Journal of Climatology*, 39(6), 3076-3090. <https://doi.org/10.1002/joc.6004>

- Li, Z., Luo, Y., Du, Y., & Chan, J. C. L. (2020). Statistical characteristics of pre-summer rainfall over south China and associated synoptic conditions. *Journal of the Meteorological Society of Japan*, 2, 98(1), 213-233. <https://doi.org/10.2151/jmsj.2020-012>
- Liang, X.-Z., & Wang, W.-C. (1998). Associations between China monsoon rainfall and tropospheric jets. *Quarterly Journal of the Royal Meteorological Society*, 124(552), 2597-2623. <https://doi.org/10.1002/qj.49712455204>
- Liao, C., Xu, H., Deng, J., & Zhang, L. (2018). Interannual Relationship between ENSO and Atlantic Storm Track in Spring Modulated by the Atlantic Multidecadal Oscillation. *Atmosphere*, 9(11). <https://doi.org/10.3390/atmos9110419>
- Lindzen, R. S., & Farrell, B. (1980). A Simple Approximate Result for the Maximum Growth Rate of Baroclinic Instabilities. *Journal of Atmospheric Sciences*, 37(7), 1648-1654. [https://doi.org/10.1175/1520-0469\(1980\)037<1648:ASARFT>2.0.CO;2](https://doi.org/10.1175/1520-0469(1980)037<1648:ASARFT>2.0.CO;2)
- Liu, B., Yan, Y., Zhu, C., Ma, S., & Li, J. (2020). Record-Breaking Meiyu Rainfall Around the Yangtze River in 2020 Regulated by the Subseasonal Phase Transition of the North Atlantic Oscillation. *Geophysical Research Letters*, 47(22), e2020GL090342. <https://doi.org/10.1029/2020GL090342>
- Liu, L., & Wang, Y. (2020). Trends in Landfalling Tropical Cyclone-Induced Precipitation over China. *Journal of Climate*, 33(6), 2223-2235. <https://doi.org/10.1175/JCLI-D-19-0693.1>
- Liu, M., Ren, H.-L., Zhang, R., Ineson, S., & Wang, R. (2021). ENSO phase-locking behavior in climate models: from CMIP5 to CMIP6. *Environmental Research Communications*, 3(3), 031004. <https://doi.org/10.1088/2515-7620/abf295>

Liu, S., & Duan, A. (2017). Impacts of the leading modes of tropical Indian Ocean Sea surface temperature anomaly on sub-seasonal evolution of the circulation and rainfall over East Asia during boreal spring and summer. *Journal of Meteorological Research*, 31(1), 171-186. <https://doi.org/10.1007/s13351-016-6093-z>

Liu, Y., Wang, L., Zhou, W., & Chen, W. (2014). Three Eurasian teleconnection patterns: spatial structures, temporal variability, and associated winter climate anomalies. *Climate Dynamics*, 42(11), 2817-2839. <https://doi.org/10.1007/s00382-014-2163-z>

Lui, Y. S., Tam, C.-Y., & Lau, N.-C. (2019). Future changes in Asian summer monsoon precipitation extremes as inferred from 20-km AGCM simulations. *Climate Dynamics*, 52(3), 1443-1459. <https://doi.org/10.1007/s00382-018-4206-3>

Luo, Y., Wu, M., Ren, F., Li, J., & Wong, W.-K. (2016). Synoptic Situations of Extreme Hourly Precipitation over China. *Journal of Climate*, 29(24), 8703-8719. <https://doi.org/10.1175/JCLI-D-16-0057.1>

Ma, J., Xu, H., & Lin, P. (2015). Meridional position biases of East Asian subtropical jet stream in CMIP5 models and their relationship with ocean model resolutions. *International Journal of Climatology*, 35(13), 3942-3958. <https://doi.org/10.1002/joc.4256>

Malik, N., Bookhagen, B., Marwan, N., & Kurths, J. (2012). Analysis of spatial and temporal extreme monsoonal rainfall over South Asia using complex networks. *Climate Dynamics*, 39(3), 971-987. <https://doi.org/10.1007/s00382-011-1156-4>

Martinez-Villalobos, C., & Neelin, J. D. (2019). Why Do Precipitation Intensities Tend to Follow Gamma Distributions? *Journal of the Atmospheric Sciences*, 76(11), 3611-3631. <https://doi.org/10.1175/JAS-D-18-0343.1>

McGregor, S., Cassou, C., Kosaka, Y., & Phillips, A. S. (2022). Projected ENSO Teleconnection Changes in CMIP6. *Geophysical Research Letters*, 49(11), e2021GL097511. <https://doi.org/10.1029/2021GL097511>

McPhaden, M. J., Lee, T., & McClurg, D. (2011). El Niño and its relationship to changing background conditions in the tropical Pacific Ocean. *Geophysical Research Letters*, 38(15). <https://doi.org/10.1029/2011GL048275>

Meehl, G. A., Boer, G. J., Covey, C., Latif, M., & Stouffer, R. J. (1997). Intercomparison makes for a better climate model. *Eos, Transactions American Geophysical Union*, 78(41), 445-451. <https://doi.org/10.1029/97EO00276>

Monirul Qader Mirza, M. (2002). Global warming and changes in the probability of occurrence of floods in Bangladesh and implications. *Global Environmental Change*, 12(2), 127-138. [https://doi.org/10.1016/S0959-3780\(02\)00002-X](https://doi.org/10.1016/S0959-3780(02)00002-X)

Moss, R. H., Edmonds, J. A., Hibbard, K. A., Manning, M. R., Rose, S. K., van Vuuren, D. P., Carter, T. R., Emori, S., Kainuma, M., Kram, T., Meehl, G. A., Mitchell, J. F. B., Nakicenovic, N., Riahi, K., Smith, S. J., Stouffer, R. J., Thomson, A. M., Weyant, J. P., & Wilbanks, T. J. (2010). The next generation of scenarios for climate change research and assessment. *Nature*, 463(7282), 747-756. <https://doi.org/10.1038/nature08823>

Namias, J., Yuan, X., & Cayan, D. R. (1988). Persistence of North Pacific Sea Surface Temperature and Atmospheric Flow Patterns. *Journal of Climate*, 1(7), 682-703. [https://doi.org/10.1175/1520-0442\(1988\)001<0682:PONPSS>2.0.CO;2](https://doi.org/10.1175/1520-0442(1988)001<0682:PONPSS>2.0.CO;2)

Nan, Y., Sun, J., Zhang, M., Hong, H., & Yuan, J. (2022). Strengthened influence of the East Asian trough on spring extreme precipitation variability over eastern Southwest China

after the late 1980s. *Atmospheric and Oceanic Science Letters*, 15(5), 100191.

<https://doi.org/10.1016/j.aosl.2022.100191>

Neelin, J. D., Battisti, D. S., Hirst, A. C., Jin, F.-F., Wakata, Y., Yamagata, T., & Zebiak, S. E.

(1998). ENSO theory. *Journal of Geophysical Research: Oceans*, 103(C7), 14261-14290.

<https://doi.org/10.1029/97JC03424>

Ng, C. H. J., Vecchi, G. A., Muñoz, Á. G., & Murakami, H. (2019). An asymmetric rainfall response to ENSO in East Asia. *Climate Dynamics*, 52(3), 2303-2318.

<https://doi.org/10.1007/s00382-018-4253-9>

O'Neill, B. C., Kriegler, E., Ebi, K. L., Kemp-Benedict, E., Riahi, K., Rothman, D. S., van Ruijven, B. J., van Vuuren, D. P., Birkmann, J., Kok, K., Levy, M., & Solecki, W. (2017).

The roads ahead: Narratives for shared socioeconomic pathways describing world futures in the 21st century. *Global Environmental Change*, 42, 169-180.

<https://doi.org/10.1016/j.gloenvcha.2015.01.004>

Park, M., & Lee, S. (2021). Is the Stationary Wave Bias in CMIP5 Simulations Driven by Latent Heating Biases? *Geophysical Research Letters*, 48(4), e2020GL091678.

<https://doi.org/10.1029/2020GL091678>

Peixoto, J. P., and A. H. Oort, (1992) Physics of Climate. *American Institute of Physics*, 520 pp.

Plumb, R. A. (1985). On the Three-Dimensional Propagation of Stationary Waves. *Journal of Atmospheric Sciences*, 42(3), 217-229. [https://doi.org/10.1175/1520-0469\(1985\)042<0217:OTTDPO>2.0.CO;2](https://doi.org/10.1175/1520-0469(1985)042<0217:OTTDPO>2.0.CO;2)

Power, S., Delage, F., Chung, C., Kociuba, G., & Keay, K. (2013). Robust twenty-first-century projections of El Niño and related precipitation variability. *Nature*, 502(7472), 541-545.

<https://doi.org/10.1038/nature12580>

Qian, Q., Jia, X., & Wu, R. (2019). Changes in the Impact of the Autumn Tibetan Plateau Snow Cover on the Winter Temperature Over North America in the mid-1990s. *Journal of Geophysical Research: Atmospheres*, 124(19), 10321-10343.

<https://doi.org/10.1029/2019JD030245>

Qin, Y., Lu, C., & Li, L. (2017). Multi-scale cyclone activity in the Changjiang River–Huaihe River valleys during spring and its relationship with rainfall anomalies. *Advances in Atmospheric Sciences*, 34(2), 246-257. <https://doi.org/10.1007/s00376-016-6042-x>

Rasmusson, E. M., & Arkin, P. A. (1985). Chapter 40 Interannual climate variability associated with the El Niño/ Southern Oscillation. In J. C. J. Nihoul (Ed.), *Elsevier Oceanography Series (Vol. 40, pp. 697-725)*. Elsevier. [https://doi.org/10.1016/S0422-9894\(08\)70736-0](https://doi.org/10.1016/S0422-9894(08)70736-0)

Rayner, N. A., Parker, D. E., Horton, E. B., Folland, C. K., Alexander, L. V., Rowell, D. P., Kent, E. C., & Kaplan, A. (2003). Global analyses of sea surface temperature, sea ice, and night marine air temperature since the late nineteenth century. *Journal of Geophysical Research: Atmospheres*, 108(D14). <https://doi.org/10.1029/2002JD002670>

Riahi, K., van Vuuren, D. P., Kriegler, E., Edmonds, J., O'Neill, B. C., Fujimori, S., Bauer, N., Calvin, K., Dellink, R., Fricko, O., Lutz, W., Popp, A., Cuaresma, J. C., Kc, S., Leimbach, M., Jiang, L., Kram, T., Rao, S., Emmerling, J., Ebi, K., Hasegawa, T., Havlik, P., Humpenöder, F., Da Silva, L. A., Smith, S., Stehfest, E., Bosetti, V., Eom, J., Gernaat, D., Masui, T., Rogelj, J., Strefler, J., Drouet, L., Krey, V., Luderer, G., Harmsen, M.,

- Takahashi, K., Baumstark, L., Doelman, J. C., Kainuma, M., Klimont, Z., Marangoni, G., Lotze-Campen, H., Obersteiner, M., Tabeau, A., & Tavoni, M. (2017). The Shared Socioeconomic Pathways and their energy, land use, and greenhouse gas emissions implications: An overview. *Global Environmental Change*, 42, 153-168.
<https://doi.org/10.1016/j.gloenvcha.2016.05.009>
- Sampe, T., & Xie, S.-P. (2010). Large-Scale Dynamics of the Meiyu-Baiu Rainband: Environmental Forcing by the Westerly Jet. *Journal of Climate*, 23(1), 113-134.
<https://doi.org/10.1175/2009JCLI3128.1>
- Sanders, F., & Hoskins, B. J. (1990). An Easy Method for Estimation of Q-Vectors from Weather Maps. *Weather and Forecasting*, 5(2), 346-353.
[https://doi.org/https://doi.org/10.1175/1520-0434\(1990\)005<0346:AEMFEO>2.0.CO;2](https://doi.org/https://doi.org/10.1175/1520-0434(1990)005<0346:AEMFEO>2.0.CO;2)
- Schiermeier, Q. (2011). Increased flood risk linked to global warming. *Nature*, 470(7334), 316-316. <https://doi.org/10.1038/470316a>
- Seneviratne, S., Nicholls, N., Easterling, D., Goodess, C., Kanae, S., Kossin, J., Luo, Y., Marengo, J., McInnes, K., & Rahimi, M. (2012). Changes in climate extremes and their impacts on the natural physical environment. In: Managing the Risks of Extreme Events and Disasters to Advance Climate Change Adaptation: Special Report of the Intergovernmental Panel on Climate Change. <https://doi.org/10.7916/d8-6nbt-s431>
- Shang, W., Li, S., Ren, X., & Duan, K. (2020). Event-based extreme precipitation in Central-Eastern China: large-scale anomalies and teleconnections. *Climate Dynamics*, 54(3), 2347-2360. <https://doi.org/10.1007/s00382-019-05116-1>

- Sheffield, J., & Wood, E. F. (2008). Projected changes in drought occurrence under future global warming from multi-model, multi-scenario, IPCC AR4 simulations. *Climate Dynamics*, 31(1), 79-105. <https://doi.org/10.1007/s00382-007-0340-z>
- Song, C.-Y., & Ahn, J.-B. (2022). Influence of Okhotsk Sea blocking on summer precipitation over South Korea. *International Journal of Climatology*, 42(6), 3553-3570. <https://doi.org/10.1002/joc.7432>
- Srinivas, G., Chowdary, J. S., Gnanaseelan, C., Parekh, A., Dandi, R., Prasad, K. V. S. R., & Naidu, C. V. (2019). Impact of differences in the decaying phase of El Niño on South and East Asia summer monsoon in CMIP5 models. *International Journal of Climatology*, 39(14), 5503-5521. <https://doi.org/10.1002/joc.6168>
- Stuecker, M. F., Timmermann, A., Jin, F.-F., McGregor, S., & Ren, H.-L. (2013). A combination mode of the annual cycle and the El Niño/Southern Oscillation. *Nature Geoscience*, 6(7), 540-544. <https://doi.org/10.1038/ngeo1826>
- Sun, J., & Ao, J. (2013). Changes in precipitation and extreme precipitation in a warming environment in China. *Chinese Science Bulletin*, 58(12), 1395-1401. <https://doi.org/10.1007/s11434-012-5542-z>
- Sun, Q., Miao, C., Qiao, Y., & Duan, Q. (2017). The nonstationary impact of local temperature changes and ENSO on extreme precipitation at the global scale. *Climate Dynamics*, 49(11), 4281-4292. <https://doi.org/10.1007/s00382-017-3586-0>
- Takaya, K., & Nakamura, H. (2001). A Formulation of a Phase-Independent Wave-Activity Flux for Stationary and Migratory Quasigeostrophic Eddies on a Zonally Varying Basic

Flow. *Journal of the Atmospheric Sciences*, 58(6), 608-627. [https://doi.org/10.1175/1520-0469\(2001\)058<0608:AFOAPI>2.0.CO;2](https://doi.org/10.1175/1520-0469(2001)058<0608:AFOAPI>2.0.CO;2)

Tang, B., Hu, W., & Duan, A. (2021). Assessment of Extreme Precipitation Indices over Indochina and South China in CMIP6 Models. *Journal of Climate*, 34(18), 7507-7524. <https://doi.org/10.1175/JCLI-D-20-0948.1>

Tang, B., Hu, W., & Duan, A. (2021). Future Projection of Extreme Precipitation Indices over the Indochina Peninsula and South China in CMIP6 Models. *Journal of Climate*, 34(21), 8793-8811. <https://doi.org/10.1175/JCLI-D-20-0946.1>

Tang, Y., Huang, A., Wu, P., Huang, D., Xue, D., & Wu, Y. (2021). Drivers of Summer Extreme Precipitation Events Over East China. *Geophysical Research Letters*, 48(11), e2021GL093670. <https://doi.org/10.1029/2021GL093670>

Tian, F., Li, S., Dong, B., Klingaman, N. P., Freychet, N., & Sparrow, S. (2022). Physical processes of summer extreme rainfall interannual variability in eastern China: Part I—observational analysis. *Climate Dynamics*, 59(1), 201-217. <https://doi.org/10.1007/s00382-021-06123-x>

Timmermann, A., An, S.-I., Kug, J.-S., Jin, F.-F., Cai, W., Capotondi, A., Cobb, K. M., Lengaigne, M., McPhaden, M. J., Stuecker, M. F., Stein, K., Wittenberg, A. T., Yun, K.-S., Bayr, T., Chen, H.-C., Chikamoto, Y., Dewitte, B., Dommeneget, D., Grothe, P., Guilyardi, E., Ham, Y.-G., Hayashi, M., Ineson, S., Kang, D., Kim, S., Kim, W., Lee, J.-Y., Li, T., Luo, J.-J., McGregor, S., Planton, Y., Power, S., Rashid, H., Ren, H.-L., Santoso, A., Takahashi, K., Todd, A., Wang, G., Wang, G., Xie, R., Yang, W.-H., Yeh, S.-W.,

- Yoon, J., Zeller, E., & Zhang, X. (2018). El Niño–Southern Oscillation complexity. *Nature*, 559(7715), 535-545. <https://doi.org/10.1038/s41586-018-0252-6>
- Tong, M., Zheng, Z., & Fu, Q. (2022). Evaluation of East Asian Meiyu from CMIP6/AMIP simulations. *Climate Dynamics*, 59(7), 2429-2444. <https://doi.org/10.1007/s00382-022-06218-z>
- Trenberth, K. E., & Stepaniak, D. P. (2001). Indices of El Niño Evolution. *Journal of Climate*, 14(8), 1697-1701. [https://doi.org/10.1175/1520-0442\(2001\)014<1697:LIOENO>2.0.CO;2](https://doi.org/10.1175/1520-0442(2001)014<1697:LIOENO>2.0.CO;2)
- Trenberth, K. E., Dai, A., van der Schrier, G., Jones, P. D., Barichivich, J., Briffa, K. R., & Sheffield, J. (2014). Global warming and changes in drought. *Nature Climate Change*, 4(1), 17-22. <https://doi.org/10.1038/nclimate2067>
- Vaid, B. H., & San Liang, X. (2015). Tropospheric temperature gradient and its relation to the South and East Asian precipitation variability. *Meteorology and Atmospheric Physics*, 127(5), 579-585. <https://doi.org/10.1007/s00703-015-0385-1>
- Veiga, S. F., & Yuan, H. (2021). Performance-based projection of precipitation extremes over China based on CMIP5/6 models using integrated quadratic distance. *Weather and Climate Extremes*, 34, 100398. <https://doi.org/10.1016/j.wace.2021.100398>
- Wainwright, C. M., Black, E., & Allan, R. P. (2021). Future Changes in Wet and Dry Season Characteristics in CMIP5 and CMIP6 Simulations. *Journal of Hydrometeorology*, 22(9), 2339-2357. <https://doi.org/10.1175/JHM-D-21-0017.1>
- Wang, B., & Zhang, Q. (2002). Pacific–East Asian Teleconnection. Part II: How the Philippine Sea Anomalous Anticyclone is Established during El Niño Development. *Journal of*

Climate, 15(22), 3252-3265. [https://doi.org/10.1175/1520-0442\(2002\)015<3252:PEATPI>2.0.CO;2](https://doi.org/10.1175/1520-0442(2002)015<3252:PEATPI>2.0.CO;2)

Wang, B., Liu, J., Kim, H.-J., Webster, P. J., & Yim, S.-Y. (2012). Recent change of the global monsoon precipitation (1979–2008). *Climate Dynamics*, 39(5), 1123-1135. <https://doi.org/10.1007/s00382-011-1266-z>

Wang, B., Wu, R., & Fu, X. (2000). Pacific–East Asian Teleconnection: How Does ENSO Affect East Asian Climate? *Journal of Climate*, 13(9), 1517-1536. [https://doi.org/10.1175/1520-0442\(2000\)013<1517:PEATHD>2.0.CO;2](https://doi.org/10.1175/1520-0442(2000)013<1517:PEATHD>2.0.CO;2)

Wang, B., Wu, R., & Li, T. (2003). Atmosphere–Warm Ocean Interaction and Its Impacts on Asian–Australian Monsoon Variation. *Journal of Climate*, 16(8), 1195-1211. [https://doi.org/10.1175/1520-0442\(2003\)16<1195:AOIAII>2.0.CO;2](https://doi.org/10.1175/1520-0442(2003)16<1195:AOIAII>2.0.CO;2)

Wang, C. (2002). Atmospheric Circulation Cells Associated with the El Niño–Southern Oscillation. *Journal of Climate*, 15(4), 399-419. [https://doi.org/10.1175/1520-0442\(2002\)015<0399:ACCAWT>2.0.CO;2](https://doi.org/10.1175/1520-0442(2002)015<0399:ACCAWT>2.0.CO;2)

Wang, L., Yang, Z., Gu, X., & Li, J. (2020). Linkages Between Tropical Cyclones and Extreme Precipitation over China and the Role of ENSO. *International Journal of Disaster Risk Science*, 11(4), 538-553. <https://doi.org/10.1007/s13753-020-00285-8>

Wang, P., Tam, C.-Y., & Xu, K. (2019). El Niño–East Asian monsoon teleconnection and its diversity in CMIP5 models. *Climate Dynamics*, 53(9), 6417-6435. <https://doi.org/10.1007/s00382-019-04938-3>

Wang, P., Tam, C.-Y., Lau, N.-C., & Xu, K. (2021). Future impacts of two types of El Niño on East Asian rainfall based on CMIP5 model projections. *Climate Dynamics*, 56(3), 899-916. <https://doi.org/10.1007/s00382-020-05510-0>

Wang, S., H. Zuo, F. Sun, L. Wu, Y. Yin, & J. Luo, (2021). Dynamics of East Asian Spring Rainband and Spring–Autumn Contrast: Environmental Forcings of Large-Scale Circulation. *J. Climate*, 34, 3523–3541, <https://doi.org/10.1175/JCLI-D-20-0501.1>.

Wang, W., Tang, H., Li, J., & Hou, Y. (2022). Spatial-Temporal Variations of Extreme Precipitation Characteristics and Its Correlation with El Niño-Southern Oscillation during 1960–2019 in Hubei Province, China. *Atmosphere*, 13(11). <https://doi.org/10.3390/atmos13111922>

Wang, X., Guan, C., Huang, R. X., Tan, W., & Wang, L. (2019). The roles of tropical and subtropical wind stress anomalies in the El Niño Modoki onset. *Climate Dynamics*, 52(11), 6585–6597. <https://doi.org/10.1007/s00382-018-4534-3>

Wang, X., Li, T., & He, C. (2021). Impact of the Mean State on El Niño–Induced Western North Pacific Anomalous Anticyclones during El Niño Decaying Summer in AMIP Models. *Journal of Climate*, 34(22), 9201–9217. <https://doi.org/10.1175/JCLI-D-20-0747.1>

Wang, Y., & Zhou, L. (2005). Observed trends in extreme precipitation events in China during 1961–2001 and the associated changes in large-scale circulation. *Geophysical Research Letters*, 32(9). <https://doi.org/10.1029/2005GL022574>

Wang, Z., Duan, A., Yang, S., & Ullah, K. (2017). Atmospheric moisture budget and its regulation on the variability of summer precipitation over the Tibetan Plateau. *Journal of*

Geophysical Research: Atmospheres, 122(2), 614-630.

<https://doi.org/10.1002/2016JD025515>

Wei, W., Zhang, R., Wen, M., & Yang, S. (2017). Relationship between the Asian Westerly Jet Stream and Summer Rainfall over Central Asia and North China: Roles of the Indian Monsoon and the South Asian High. *Journal of Climate*, 30(2), 537-552.

<https://doi.org/10.1175/JCLI-D-15-0814.1>

Williams, I. N., & Patricola, C. M. (2018). Diversity of ENSO Events Unified by Convective Threshold Sea Surface Temperature: A Nonlinear ENSO Index. *Geophysical Research Letters*, 45(17), 9236-9244. <https://doi.org/10.1029/2018GL079203>

Wu, B., Li, T., & Zhou, T. (2010). Relative Contributions of the Indian Ocean and Local SST Anomalies to the Maintenance of the Western North Pacific Anomalous Anticyclone during the El Niño Decaying Summer. *Journal of Climate*, 23(11), 2974-2986.

<https://doi.org/10.1175/2010JCLI3300.1>

Wu, B., Zhou, T., & Li, T. (2017). Atmospheric Dynamic and Thermodynamic Processes Driving the Western North Pacific Anomalous Anticyclone during El Niño. Part II: Formation Processes. *Journal of Climate*, 30(23), 9637-9650.

<https://doi.org/10.1175/JCLI-D-16-0495.1>

Wu, B., Zhou, T., & Li, T. (2017). Atmospheric Dynamic and Thermodynamic Processes Driving the Western North Pacific Anomalous Anticyclone during El Niño. Part I: Maintenance Mechanisms. *Journal of Climate*, 30(23), 9621-9635.

<https://doi.org/10.1175/JCLI-D-16-0489.1>

- Wu, R., Hu, Z.-Z., & Kirtman, B. P. (2003). Evolution of ENSO-Related Rainfall Anomalies in East Asia. *Journal of Climate*, 16(22), 3742-3758. [https://doi.org/10.1175/1520-0442\(2003\)016<3742:EOERAI>2.0.CO;2](https://doi.org/10.1175/1520-0442(2003)016<3742:EOERAI>2.0.CO;2)
- Wulf, H., Bookhagen, B., & Scherler, D. (2012). Climatic and geologic controls on suspended sediment flux in the Sutlej River Valley, western Himalaya. *Hydrol. Earth Syst. Sci.*, 16(7), 2193-2217. <https://doi.org/10.5194/hess-16-2193-2012>
- Xie, S.-P., Hu, K., Hafner, J., Tokinaga, H., Du, Y., Huang, G., & Sampe, T. (2009). Indian Ocean Capacitor Effect on Indo-Western Pacific Climate during the Summer following El Niño. *Journal of Climate*, 22(3), 730-747. <https://doi.org/10.1175/2008JCLI2544.1>
- Xie, S.-P., Kosaka, Y., Du, Y., Hu, K., Chowdary, J. S., & Huang, G. (2016). Indo-western Pacific Ocean capacitor and coherent climate anomalies in post-ENSO summer: A review. *Advances in Atmospheric Sciences*, 33(4), 411-432. <https://doi.org/10.1007/s00376-015-5192-6>
- Xin, X., Wu, T., Zhang, J., Yao, J., & Fang, Y. (2020). Comparison of CMIP6 and CMIP5 simulations of precipitation in China and the East Asian summer monsoon. *International Journal of Climatology*, 40(15), 6423-6440. <https://doi.org/10.1002/joc.6590>
- Xu, H., Chen, H., & Wang, H. (2022). Future changes in precipitation extremes across China based on CMIP6 models. *International Journal of Climatology*, 42(1), 635-651. <https://doi.org/10.1002/joc.7264>
- Xu, J., Zhang, Q., Bi, B., & Chen, Y. (2022). Spring Extreme Precipitation Days in North China and Their Reliance on Atmospheric Circulation Patterns during 1979–2019. *Journal of Climate*, 35(7), 2253-2267. <https://doi.org/10.1175/JCLI-D-21-0268.1>

- Xu, K., Huang, Q.-L., Tam, C.-Y., Wang, W., Chen, S., & Zhu, C. (2019). Roles of tropical SST patterns during two types of ENSO in modulating wintertime rainfall over southern China. *Climate Dynamics*, 52(1), 523-538. <https://doi.org/10.1007/s00382-018-4170-y>
- Xu, K., Huang, R. X., Wang, W., Zhu, C., & Lu, R. (2017). Thermocline Fluctuations in the Equatorial Pacific Related to the Two Types of El Niño Events. *Journal of Climate*, 30(17), 6611-6627. <https://doi.org/10.1175/JCLI-D-16-0291.1>
- Xu, K., Tam, C.-Y., Zhu, C., Liu, B., & Wang, W. (2017). CMIP5 Projections of Two Types of El Niño and Their Related Tropical Precipitation in the Twenty-First Century. *Journal of Climate*, 30(3), 849-864. <https://doi.org/10.1175/JCLI-D-16-0413.1>
- Yang, J., Liu, Q., Xie, S.-P., Liu, Z., & Wu, L. (2007). Impact of the Indian Ocean SST basin mode on the Asian summer monsoon. *Geophysical Research Letters*, 34(2). <https://doi.org/10.1029/2006GL028571>
- Yang, S., Lau, K. M., & Kim, K. M. (2002). Variations of the East Asian Jet Stream and Asian-Pacific–American Winter Climate Anomalies. *Journal of Climate*, 15(3), 306-325. [https://doi.org/10.1175/1520-0442\(2002\)015<0306:VOTEAJ>2.0.CO;2](https://doi.org/10.1175/1520-0442(2002)015<0306:VOTEAJ>2.0.CO;2)
- Yatagai, A., Kamiguchi, K., Arakawa, O., Hamada, A., Yasutomi, N., & Kitoh, A. (2012). APHRODITE: Constructing a Long-Term Daily Gridded Precipitation Dataset for Asia Based on a Dense Network of Rain Gauges. *Bulletin of the American Meteorological Society*, 93(9), 1401-1415. <https://doi.org/10.1175/BAMS-D-11-00122.1>
- Yin, H., & Sun, Y. (2018). Detection of Anthropogenic Influence on Fixed Threshold Indices of Extreme Temperature. *Journal of Climate*, 31(16), 6341-6352. <https://doi.org/10.1175/JCLI-D-17-0853.1>

- Ying, X., Jie, W., Ying, S., Bo-Tao, Z., Rou-Ke, L., & Jia, W. (2015). Change in Extreme Climate Events over China Based on CMIP5. *Atmospheric and Oceanic Science Letters*, 8(4), 185-192. <https://doi.org/10.3878/AOSL20150006>
- You, Q., Jiang, Z., Yue, X., Guo, W., Liu, Y., Cao, J., Li, W., Wu, F., Cai, Z., Zhu, H., Li, T., Liu, Z., He, J., Chen, D., Pepin, N., & Zhai, P. (2022). Recent frontiers of climate changes in East Asia at global warming of 1.5°C and 2°C. *npj Climate and Atmospheric Science*, 5(1), 80. <https://doi.org/10.1038/s41612-022-00303-0>
- Yu JY, Kao HY, Lee T (2010) Subtropics-related interannual sea surface temperature variability in the central equatorial pacific. *J Clim.* <https://doi.org/10.1175/2010JCLI3171.1>
- Yu J-Y. , & Giese BS (2013) ENSO diversity in observations. *US CLIVAR Var*
- Yu, B., & Boer, G. (2002). The roles of radiation and dynamical processes in the El Niño-like response to global warming. *Climate Dynamics*, 19(5), 539-554. <https://doi.org/10.1007/s00382-002-0244-x>
- Yu, J.-Y., & Kao, H.-Y. (2007). Decadal changes of ENSO persistence barrier in SST and ocean heat content indices: 1958–2001. *Journal of Geophysical Research: Atmospheres*, 112(D13). <https://doi.org/10.1029/2006JD007654>
- Yu, T., Feng, J., Chen, W., & Wang, X. (2021). Persistence and breakdown of the western North Pacific anomalous anticyclone during the EP and CP El Niño decaying spring. *Climate Dynamics*, 57(11), 3529-3544. <https://doi.org/10.1007/s00382-021-05882-x>

Yuan, X., Wang, S., & Hu, Z.-Z. (2018). Do Climate Change and El Niño Increase Likelihood of Yangtze River Extreme Rainfall? *Bulletin of the American Meteorological Society*, 99(1), S113-S117. <https://doi.org/10.1175/BAMS-D-17-0089.1>

Yuan, Y., & Yang, S. (2012). Impacts of Different Types of El Niño on the East Asian Climate: Focus on ENSO Cycles. *Journal of Climate*, 25(21), 7702-7722. <https://doi.org/10.1175/JCLI-D-11-00576.1>

Zhang, Q., Gu, X., Li, J., Shi, P., & Singh, V. P. (2018). The Impact of Tropical Cyclones on Extreme Precipitation over Coastal and Inland Areas of China and Its Association to ENSO. *Journal of Climate*, 31(5), 1865-1880. <https://doi.org/10.1175/JCLI-D-17-0474.1>

Zhang, Q., Zheng, Y., Singh, V. P., Luo, M., & Xie, Z. (2017). Summer extreme precipitation in eastern China: Mechanisms and impacts. *Journal of Geophysical Research: Atmospheres*, 122(5), 2766-2778. <https://doi.org/10.1002/2016JD025913>

Zhang, R., & Sumi, A. (2002). Moisture Circulation over East Asia during El Niño Episode in Northern Winter, Spring and Autumn. *Journal of the Meteorological Society of Japan. Ser. II*, 80(2), 213-227. <https://doi.org/10.2151/jmsj.80.213>

Zhang, R., Sumi, A., & Kimoto, M. (1996). Impact of El Niño on the East Asian Monsoon: A Diagnostic Study of the '86/87 and '91/92 Events. *Journal of the Meteorological Society of Japan. Ser. II*, 74(1), 49-62. https://doi.org/10.2151/jmsj1965.74.1_49

Zhang, R., Sumi, A., & Kimoto, M. (1999). A diagnostic study of the impact of El Niño on the precipitation in China. *Advances in Atmospheric Sciences*, 16(2), 229-241. <https://doi.org/10.1007/BF02973084>

Zhang, W., Jin, F.-F., Li, J., & Ren, H.-L. (2011). Contrasting Impacts of Two-Type El Niño over the Western North Pacific during Boreal Autumn. *Journal of the Meteorological Society of Japan. Ser. II*, 89(5), 563-569.

<https://doi.org/10.2151/jmsj.2011-510>

Zhao, D., Yu, Y., & Chen, L. (2021). Impact of the Monsoonal Surge on Extreme Rainfall of Landfalling Tropical Cyclones. *Advances in Atmospheric Sciences*, 38(5), 771-784.

<https://doi.org/10.1007/s00376-021-0281-1>

Zhao, T., Chen, L., & Ma, Z. (2014). Simulation of historical and projected climate change in arid and semiarid areas by CMIP5 models. *Chinese Science Bulletin*, 59(4), 412-429.

<https://doi.org/10.1007/s11434-013-0003-x>

Zheng, F., Fang, X.-H., Yu, J.-Y., & Zhu, J. (2014). Asymmetry of the Bjerknes positive feedback between the two types of El Niño. *Geophysical Research Letters*, 41(21), 7651-7657. <https://doi.org/10.1002/2014GL062125>

Zhong, W., Wu, Y., Yang, S., Ma, T., Cai, Q., & Liu, Q. (2023). Heavy Southern China Spring Rainfall Promoted by Multi-Year El Niño Events. *Geophysical Research Letters*, 50(7), e2022GL102346. <https://doi.org/10.1029/2022GL102346>

Zhou, X., Liu, F., Wang, B., Xiang, B., Xing, C., & Wang, H. (2019). Different responses of East Asian summer rainfall to El Niño decays. *Climate Dynamics*, 53(3), 1497-1515. <https://doi.org/10.1007/s00382-019-04684-6>

Zhu, H., Jiang, Z., & Li, L. (2021). Projection of climate extremes in China, an incremental exercise from CMIP5 to CMIP6. *Science Bulletin*, 66(24), 2528-2537. <https://doi.org/10.1016/j.scib.2021.07.026>

Zhu, H., Jiang, Z., Li, J., Li, W., Sun, C., & Li, L. (2020). Does CMIP6 Inspire More Confidence in Simulating Climate Extremes over China? *Advances in Atmospheric Sciences*, 37(10), 1119-1132. <https://doi.org/10.1007/s00376-020-9289-1>